INFORMATION TO USERS

This manuscript has been reproduced from the microfilm master. UMI films the text directly from the original or copy submitted. Thus, some thesis and dissertation copies are in typewriter face, while others may be from any type of computer printer.

The quality of this reproduction is dependent upon the quality of the copy submitted. Broken or indistinct print, colored or poor quality illustrations and photographs, print bleedthrough, substandard margins, and improper alignment can adversely affect reproduction.

In the unlikely event that the author did not send UMI a complete manuscript and there are missing pages, these will be noted. Also, if unauthorized copyright material had to be removed, a note will indicate the deletion.

Oversize materials (e.g., maps, drawings, charts) are reproduced by sectioning the original, beginning at the upper left-hand corner and continuing from left to right in equal sections with small overlaps.

Photographs included in the original manuscript have been reproduced xerographically in this copy. Higher quality 6" x 9" black and white photographic prints are available for any photographs or illustrations appearing in this copy for an additional charge. Contact UMI directly to order.

Bell & Howell Information and Learning
300 North Zeeb Road, Ann Arbor, MI 48106-1346 USA
800-521-0600

Methods for Calculating the Free Energy of Atomic Clusters

Lynn Amon

A dissertation submitted in partial fulfillment
of the requirements for the degree of

Doctor of Philosophy

University of Washington

2000

Program Authorized to Offer Degree: Chemistry

In presenting this dissertation in partial fulfillment of the requirements for the Doctorial degree at the University of Washington, I agree that the Library shall make its copies freely available for inspection. I further agree that extensive copying of this thesis is allowable only for scholarly purposes, consistent with "fair use" as prescribed in the U.S. Copyright Law. Requests for copying or reproduction of this dissertation may be referred to University Microfilms, 1490 Eisenhower Place, P.O. Box 975, Ann Arbor, MI 48106, to whom the author has granted "the right to reproduce and sell (a) copies of the manuscript in microform and/or (b) printed copies of the manuscript made from microform."

Signature 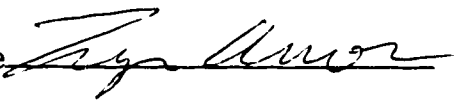

Date 3-13-2000

University of Washington

Graduate School

This is to certify that I have examined this copy of a doctoral dissertation by

Lynn Amon

and have found that it is complete and satisfactory in all respects,
and that any and all revisions required by the final
examining committee have been made.

Chair of Supervisory Committee:

William P. Reinhardt

Reading Committee:

Hannes Jonsson

David Baker

Date: March 13 2000

University of Washington

Abstract

Methods for Calculating the Free Energy of Atomic Clusters

by Lynn Amon

Chair of Supervisory Committee

Professor William P. Reinhardt
Department of Chemistry

We have extended the finite-time variational method for calculating free energy differences, ΔA, to atomic clusters. The main obstacle in calculating ΔA for finite systems is finding a suitable reference state. We present an optimal reference state for liquid clusters as well as one for solid clusters. Thus, the free energy for clusters in each phase can be calculated separately. The method is tested on LJ_{55} for a wide range of temperatures. This method should be easily extended to molecular clusters or large molecules and would allow one to determine the stability of different geometrical isomers at non-zero temperatures. We also examine the commonly used practice of adjusting the maximum step size during Metropolis Monte Carlo simulation.

TABLE OF CONTENTS

LIST OF FIGURES

LIST OF TABLES

ACKNOWLEDGMENTS

I would like to thank William P. Reinhardt for acting as my advisor and helping to edit this dissertation. I would also like to thank the following people: Mark Miller provided the some of the data in chapter 3. Jonathon Doye generously provided his data for comparison. John Hunter brought the reversible scaling paper to my attention among other things. Susan Rempe helped me with coordinate systems. I have also had very helpful discussions with David Wales and Stephen Berry.

Funding was provided by the National Physical Science Consortium and UW-HPCC grant.

Chapter 1

INTRODUCTION

The goal of the work presented in this thesis is the development of a method for determining the order of stability of different geometric isomers of an atomic or molecular cluster at a non-zero temperature. We show how several different approaches can be made to solve this problem which give the same result but that some are clearly more efficient than others. Though this method is generally applicable to most clusters, or large molecules for that matter, we apply it to a family of well-studied clusters in which the interactions are chosen to mimic those of the noble gases.

The role of molecular structure determination in chemistry has grown over the last few decades as methods of structure determination, both experimentally and computationally, continue to improve. Computational methods are often directed at finding mechanically stable molecular conformations in which the potential energy is a minimum [1-6]. However, only at zero temperature, does a local or global potential energy minimum determine the structure. The Second Law of Thermodynamics tells us that at finite temperatures, an isolated, isothermal system always seeks to minimize its free energy rather than its potential energy. The free energy is a much more difficult property to calculate. Direct determination of the exact value requires complete enumeration of the Boltzman-weighted configurations subject to appropriate physical constraints. With the exception of simple systems like the ideal gas and harmonic

oscillator, this evaluation is infeasible. Estimates of free energies can be made by either using approximate models of the system or by employing molecular simulation to limit the scope of configurations to those which are thermodynamically relevant. The molecular simulation methods may be further divided into two classes; those which attempt to determine the free energy on an arbitrary scale and those in which an estimate of the absolute free energy is made by computing the free energy difference between the system of interest and one in which the absolute free energy is already known. In this thesis, we will refer to the former class as molecular simulation methods and the latter class as free energy difference methods.

Atomic clusters are a special case. Determining the free energy for these systems is complicated by the fact that the thermodynamics of finite systems, particularly regarding phase transitions, is significantly different than its bulk counterpart. One of the most surprising features of atomic and molecular clusters is that one with as few as seven atoms can display both solid and liquid behavior and undergo a phase transition [12]. While this behavior was first detected through molecular simulation [13], supporting experimental evidence for phase changes within an atomic cluster has also been obtained [14, 15, 16] using supersonic jets in conjunction with electron diffraction. A cluster solid-liquid phase transition differs from a bulk one in several respects. The signature of a transition from ordered to amorphous for an infinitely large system is a discontinuity in thermodynamic functions. For instance, the solid lines in figures 1.1a and b represent, respectively, a canonical caloric curve and heat capacity peak for an infinitely large system. The corresponding dashed lines are what these properties look like when the number of atoms, N, is small. At the transition temperature in the large system, the caloric curve shows a discontinuity and the heat capacity diverges. The finite system shows much different behavior. The caloric curve changes smoothly through the melting

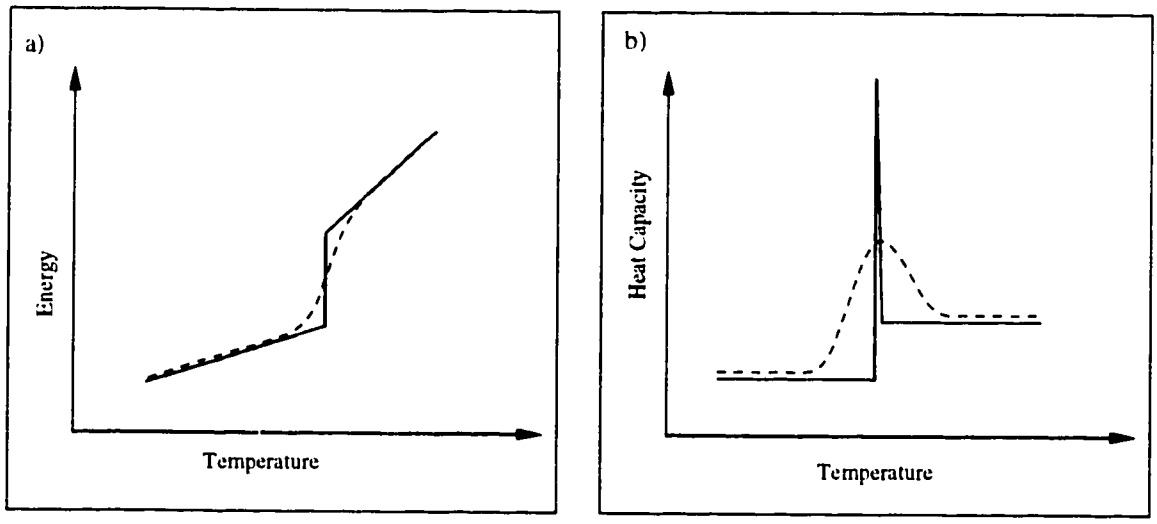

Figure 1.1: Examples of a canonical caloric curve and heat capacity as a function of temperature for an infinitely large system (solid lines) and for a small system (dashed lines).

point and the heat capacity has a round, finite peak [17]. Instead of a sharp melting point, the transition for the cluster takes place over a range of temperatures, called the melting or coexistence [18] range. The term coexistence refers to the observation that at any temperature within this range, a single cluster may fluctuate from an ordered solid structure to an amorphous liquid structure. This type of coexistence is to be distinguished from the coexistence associated with bulk systems at the melting point in which two different phases occur simultaneously.

In the thermodynamic limit, the melting point is the temperature at which the free energies of both solid and liquid are equal. Coexistence in finite systems is better illustrated with a thermodynamic function related to the free energy, the Landau free energy. It is the free energy at a given temperature of a system as a function of some order parameter. Within the melting range, the Landau free energy has two minima separated by a barrier as depicted in

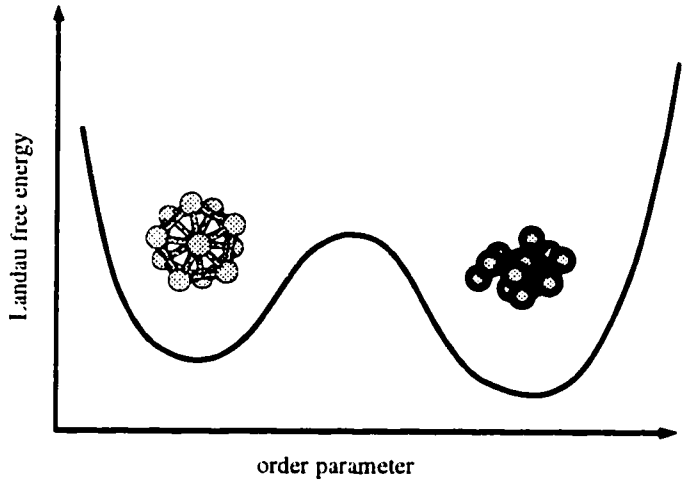

Figure 1.2: Example of a Landau free energy curve for an atomic cluster at a temperature within the coexistence region.

figure 1.2. One minimum corresponds to the solid phase and the other to the liquid phase. Unlike a bulk system, which, on becoming unstable at the melting point, decreases its free energy by splitting into two phases, small clusters may not be large enough to [5]. Larger clusters may exhibit behavior of a surface-melted phase resulting in a third minimum. Some molecular clusters, such as $(H_2O)_n$, $n = 8, 12, 20$ [15-19], can occur as several different solid isomers making the free energy landscape even more complicated.

Sorting out this landscape out has been attempted previously with approximate models and molecular simulations methods. The latter strategy, in addition to providing only relative values of the free energy, may also be ineffective at distinguishing the free energies of different phases. Free energy difference methods, on the other hand, have rarely been applied to atomic clusters [24] and never to solid clusters. In this chapter we review the existing methods for computing the free energy of clusters as well as general free energy difference methods. We then make the case that one of these latter methods is better suited to computing both solid and liquid cluster free energies on an absolute

scale.

1.1 *Calculating free energies of atomic clusters*

For the remainder of this thesis, references to free energy will always mean the Helmholtz free energy, the thermodynamic function relevant to the canonical ensemble in which the independent variables are the temperature, T, volume, V, and number of particles, N. Thermodynamically, it is considered a measure of the competition between the energy, E, and the entropy, S: $A = E - TS$. Microscopically and classically, the free energy is related to the canonical partition function, Q, as

$$A(N,V,T) = -kT \ln Q(N,V,T) \tag{1.1}$$

$$= -kT \ln[h^{-3N} \iint \exp(-H(\mathbf{p}_1,\ldots,\mathbf{p}_N,\mathbf{r}_1,\ldots,\mathbf{r}_N)/kT) \tag{1.2}$$

$$d\mathbf{p}_1,\ldots,d\mathbf{p}_N,d\mathbf{r}_1,\ldots,d\mathbf{r}_N] \tag{1.3}$$

in which k is Boltzman's constant, h is Planck's constant, and the Hamiltonian, H, is a function of the configuration coordinates of the particles, $\mathbf{r}$, and their momenta $\mathbf{p}$. The question of particle distinguishability will be addressed in chapter 4. In this thesis, we are concerned exclusively with Hamiltonians in which the momentum and configuration terms are separable into kinetic energy, KE, and potential energy, U, respectively. In this case, the integrations in equation 1.3 can be done separately.

$$\begin{aligned} Q &= \int \exp(-KE(\mathbf{p}_1,\ldots,\mathbf{p}_N)/kT)d\mathbf{p}_1,\ldots,d\mathbf{p}_N \\ &\quad \int \exp(-U(\mathbf{r}_1,\ldots,\mathbf{r}_N)/kT)d\mathbf{r}_1,\ldots,d\mathbf{r}_N \\ &= Q_{kin}\, Q_{con} \end{aligned} \tag{1.4}$$

Because the kinetic energy is simply $\sum_{i=1}^{N} \mathbf{p}_i^2/2m_i$, the first integral is easily evaluated as $Q_{kin} = (2\pi mkT)^{3N/2}$. The second integral, Q_{con}, which we will

refer to as the configurational integral, depends on the interaction between the atoms and in most cases cannot be evaluated analytically. Even when the interaction is a simple pair potential, determining Q_{con} by direct numerical integration becomes too computationally expensive for a system as small as four atoms. For these reasons, alternative methods have been developed which either approximate interactions or limit the amount of phase space explored to the most relevant part.

1.1.1 Estimating free energies with harmonic models

Estimates of free energies using approximate models are most often made by replacing the real interactions with harmonic ones. In the early 1970's [25, 26], a common practice for computing the free energy of atomic clusters was to approximate the internal motions of the clusters as $3N-6$ independent harmonic oscillators. The normal frequencies of oscillation can be obtained by diagonalizing a matrix of $(3N)^2$ second derivatives of the equilibrium potential energy [27]. The zero point energy was usually taken to be the minimized potential energy of the cluster. Translational and rotational free energy account for the other six degrees of freedom. To compute these, the mass of the whole cluster and its average moment of inertia for the given temperature can be inserted into the expressions for the translational and rotational free energy of an ideal gas particle. Approximating the interatomic motions as completely harmonic and using just one small piece, the global minimum, of the potential energy surface is quite limiting. The latter part of that problem was addressed early this decade by Wales [28] who developed a way, known as the superposition harmonic approximation (SHA), to both enumerate and use thousands of low energy minima on the PES and sum over them. Doye and Wales [4] improved the method further by including anharmonic effects.

Estimating the free energy in the SHA has several disadvantages. Includ-

ing anharmonicity is computationally intensive and is not easily generalized to other systems. It requires not only knowledge of where the minima are but also details about their curvatures. For a cluster of 55 atoms interacting with the Lennard-Jones potential, LJ_{55}, omission of anharmonicity was shown to substantially affect estimates of the free energy, so it cannot be neglected. These results will be shown and discussed further in chapter 5. Even without anharmonicity, the SHA method relies heavily on detailed information about the potential energy surface such that it is not readily transferable to other systems. Lastly, since the number of minima in the PES may be prohibitively large, only a small subset of them can be considered.

A distinct advantage of the SHA method is that once all the minima have been found, their corresponding structures can be examined to determine if they belong to the solid, liquid or surface-melted phase. Doye and Wales [29] have shown that by grouping these minima by phase and summing over the group, the free energy of each phase can be computed separately. These results will also discussed in chapter 5.

1.1.2 Estimating free energies with molecular simulation

An alternative method for estimating free energies is to limit the amount of phase space considered to the part which is most relevant. Such limitations can be achieved via two types of molecular simulation: constant temperature molecular dynamics or Metropolis Monte Carlo. Both kinds of simulation consist of a series of steps in which a set of atoms advances from one configuration to another based on the interaction potential of the atoms, U, and the temperature, T, and volume, V, of the system thereby simulating how the atoms in the canonical ensemble would behave. Once equilibrated, the subsequent "dynamics" of the system is determined by the inter-particle potential. Trajectories thus contain information directly relevant to the phase space accessible to the

actual system.

A Metropolis Monte Carlo (MC) [30] simulation allows one to sample phase space with a Boltzman distribution. It begins with a system of N atoms in an initial configuration, $\mathbf{r}^{(i)} = \mathbf{r}_1^{(i)}, \mathbf{r}_2^{(i)}, \ldots \mathbf{r}_N^{(i)}$. A trial move is then made by randomly selecting an atom and displacing it by a random amount up some maximum step size resulting in a new configuration, $\mathbf{r}^{(i')}$. The change in the potential energy of the system is $\Delta U = U(\mathbf{r}^{(i')}) - U(\mathbf{r}^{(i)})$. The move is accepted if $\exp(-\Delta U/kT) > \text{ran}()$ where ran() is random number uniformly distributed over $(0, 1]$ and k is Boltzman's constant. If the move is accepted, $\mathbf{r}^{(i+1)} = \mathbf{r}^{(i')}$, if not, $\mathbf{r}^{(i+1)} = \mathbf{r}^{(i)}$. After many MC sweeps, N MC trial moves, data from the simulation can be used to calculate equilibrium averages of an observable property, $M(\mathbf{r})$:

$$\langle M \rangle = \frac{\int M(\mathbf{r}) \exp(-U(\mathbf{r})/kT) d\mathbf{r}}{\int \exp(-U(\mathbf{r})/kT) d\mathbf{r}} \approx \frac{1}{n} \sum_{i=1}^{n} M(\mathbf{r}^{(i)}) \tag{1.5}$$

where n is the total number of MC steps.

Molecular dynamics (MD) works quite differently. All N atoms are advanced in one step from $\mathbf{r}^{(i)}$ to $\mathbf{r}^{(i+1)}$ by computing all the forces on the atoms and integrating Newton's equations of motion. The total energy of the system, $KE + U$, is conserved but the temperature fluctuates resulting in a microcanonical ensemble. In the canonical ensemble the temperature must be fixed. Two methods are commonly used for this purpose: the Andersen thermostat and the Nose-Hoover thermostat. With the Andersen thermostat [31], atoms selected from a Poisson distribution are assigned new velocities from a Boltzman distribution for the given temperature. Altering velocities in this way simulates stochastic collisions generated from a heat bath. The Nose-Hoover thermostat [32, 33] is deterministic. A variable called the thermodynamic friction coefficient is introduced as well as a new 'effective mass' parameter and the equations of motion are revised to include them. Both of these thermostats have

been shown to result in behavior consistent with the canonical ensemble and their data can be used to generate equilibrium averages as in equation 1.5.

Both MC and MD simulations have been used to calculate Landau free energies as a function of some order parameter. For instance, in the case atomic clusters, the order parameter used most often is the potential energy, U. Data from the simulation is used to make a histogram of the number of times a value of the order parameter is visited, $h(U)$. The Landau free energy is then $F(U) = -kT \ln h(u)/n$ where n is the total number of data points. Calculating $F(U)$ can be greatly compromised by poor sampling, especially in regions of phase space where the system spends little time. Torrie and Valleau [34] offered a remedy by limiting the simulation to specific regions of the order parameter to enhance the sampling in less populated regions. Imposing these limits is more easily implemented in a MC simulation than in an MD one. In this method, called umbrella sampling, two adjacent regions which share a common endpoint, U_o, will have a discontinuity in $F(U)$ at U_o. The difference in $F(U_o)$ between the two regions is added as a constant to one of the regions such that $F(U)$ becomes continuous throughout both regions. The statistics must be reliable for all of these regions otherwise the error in one will be propagated to all the others.

The Landau free energy only shows how two regions of configuration space are related. The Helmholtz free energy is related to $F(U)$ by

$$A(T) = -kT \ln \int \exp(-F(U)/kT) dU. \tag{1.6}$$

Because $F(U)$ is not on an absolute scale, absolute values of $A(T)$ cannot be determined in this way. However, consider the case in which $F(U)$ has two minima separated by a barrier indicating two states which coexist like the one depicted in figure 1.2. Ideally, integrating over each minimum would allow one to determine relative Helmholtz free energies of the two states. However, in

addition to the discretization of U which can lead to accuracy problems, the order parameter may not distinguish one state from another. For example, $F(U)$ calculated for LJ_{55} at a temperature at which solid, surface-melted and liquid states all coexist showed only two wells [5, 29]. The solid and surface-melted states could not be differentiated from each other. Even the solid and and liquid wells have significant overlap so the end points for integration will also contribute to the systematic error in A. Landau free energy curves computed with other order parameters, based on the geometry of the cluster, showed even less distinction between the minima.

A method closely related to umbrella sampling is the multiple histogram method. Two similar varieties of this method were developed independently by Ferrenberg and Swendsen [35] and by Labastie and Whetten [3]. As in computing Landau free energies, both versions entail running a canonical MC or MD simulation at a temperature, T, and storing the data in a histogram, $h_T(U)$, where again we use the potential energy as the order parameter. The essential idea to the multihistogram method is that $h_T(U)$ can be used to calculate the canonical probability distribution, $P_T(U)$, as well as $P_{T_i}(U)$ for T_i in the neighborhood of T:

$$P_{T_i}(U) = P_T(U)\frac{\int \exp[-U(1/kT_i - 1/kT)]dU}{\int P_T(U)\exp[-U(1/kT_i - 1/kT)]dU} \tag{1.7}$$

where

$$P_T(U) = \frac{h(u)\exp(-U/kT)}{\int h(u)\exp(-U/kT)dU}. \tag{1.8}$$

Equation 1.8 relies on a simple estimate of the density of states, $\Omega(U) = h_T(U)/n$. To improve the estimate, $h_{T_i}(U)$ for a broad range of temperatures $\{T_i\}$ can be collected and averaged using a set of weighting functions which minimize the

statistical error in $\Omega(U)$. The resulting multihistogram equations are

$$\Omega(U) = \frac{\sum_i h_{T_i}(U)/g_i}{\sum_i n_i \exp[(A_{T_i} - U)/kT_i]/g_i} \tag{1.9}$$

$$\exp(-A_{T_i}/kT_i) = \int \Omega(U) \exp(-U/kT_i) dU \tag{1.10}$$

and must be solved self-consistently. Using a range of temperatures increases the sampling of data, and combined with error minimization technique, ideally should produce a $\Omega(U)$ accurate enough to use at any temperature. The Helmholtz free energy is obtained from $\Omega(U)$ by $A(T) = -kT \ln(\int \Omega(U) \exp(-U/kT) dU)$. Tsai and Jordan [36] took this method even further in their Monte Carlo simulations of LJ_{13} clusters by adding a jump-walking scheme [37] to further enhance ergodicity. Again, however, the value of $A(T)$ will not be on an absolute scale and free energies of individual phases are not easily determined using this method for the same reasons listed above.

1.2 Free Energy Difference Methods

An alternative method to calculating free energies directly is to instead compute the free energy differences, $\Delta A = A_1 - A_0$, between a system with potential energy U_0 and some reference state with U_1. If A_1 is already known then the absolute free energy of the system is easily evaluated from ΔA. Several methods have been developed [38, 39] for this purpose and are reviewed in this section.

The first of these methods, free energy perturbation (FEP) [40], is based on

the following equations:

$$\langle M \rangle = \frac{\int M \exp(-U(\mathbf{r})/kT) d\mathbf{r}}{\int \exp(-U(\mathbf{r})/kT) d\mathbf{r}} \tag{1.11}$$

$$Q = \int \exp(-U(\mathbf{r})/kT) d\mathbf{r} \tag{1.12}$$

$$\Delta A = -kT \ln \frac{Q_1}{Q_0} \tag{1.13}$$

$$= -kT \ln \frac{\int \exp(-U_0(\mathbf{r})/kT) \exp(-[U_1(\mathbf{r}) - U_0(\mathbf{r})]/kT) d\mathbf{r}}{\int \exp(-U_0(\mathbf{r})/kT)} \tag{1.14}$$

where $\langle M \rangle$ is the expectation value or equilibrium average of some property M. In this case, the property is $\exp(-[U_1(\mathbf{r}) - U_0(\mathbf{r})]/kT)$ and

$$\Delta A = -kT \ln \left\langle \exp\left(-\frac{U_1(\mathbf{r}) - U_0(\mathbf{r})}{kT}\right) \right\rangle_0 \tag{1.15}$$

The average can be taken over a canonical MC or MD simulation in which the potential energy is $U_0(\mathbf{r})$ as indicated by the subscript 0. Calculating a good average of an exponential is difficult because one data point can overwhelm the whole average. One check of the accuracy is to also perform a simulation using U_1 such that

$$\Delta A = kT \ln \left\langle \exp\left(\frac{U_1(\mathbf{r}) - U_0(\mathbf{r})}{kT}\right) \right\rangle_1 \tag{1.16}$$

which should produce the same result as equation 1.15. Performing a double-ended calculation also allows one to determine crude upper and lower bounds to ΔA by using the Gibbs-Bogoliubov-Feynman inequality, $\langle \exp f \rangle \geq \exp\langle f \rangle$ which applied to equations 1.15 and 1.16 result in

$$\langle U_1(\mathbf{r}) - U_0(\mathbf{r}) \rangle_1 \leq \Delta A \leq \langle U_1(\mathbf{r}) - U_0(\mathbf{r}) \rangle_0 \tag{1.17}$$

The statistics can be improved by choosing two states which are similar. Towards that end, a series of n steps can be made to take U_0 to U_1 such that

$$\Delta A = -kT \sum_{i=1}^{n-1} \ln \left\langle \exp\left(-\frac{U_{i+1}(\mathbf{r}) - U_i(\mathbf{r})}{kT}\right) \right\rangle_i$$

or the points can be joined by curve-fitting and integration.

An improvement that can be made to the FEP method but which is not widely used is the acceptance ratio method [41]. It shares some similarities with the multiple histogram method. The exponential of the free energy difference between states 0 and 1 is the ratio of partition functions,

$$\exp(-kT\Delta A) = \frac{Q_0}{Q_1} = \frac{Q_0 \int w \exp[-kT(U_0(\mathbf{r}) + U_1(\mathbf{r}))]d\mathbf{r}}{Q_1 \int w \exp[-kT(U_0(\mathbf{r}) + U_1(\mathbf{r}))]d\mathbf{r}} \tag{1.18}$$

$$= \frac{\langle w \exp(-kTU_0)\rangle_1}{\langle w \exp(-kTU_1)\rangle_0} \tag{1.19}$$

where w is a weighting factor which can be optimized to minimize the variance of the averages. The result is two equations that must be solved self-consistently.

$$\frac{Q_0}{Q_1} = \frac{\langle f(kT(U_0 - U_1 + C))\rangle_1}{\langle f(kT(U_1 - U_0 - C))\rangle_0} \exp(kT\,C) \tag{1.20}$$

$$C = \ln\left(\frac{Q_0}{Q_1}\right) \tag{1.21}$$

The function f is the Fermi function $f(x) = 1/(1 + \exp(x))$. An initial guess for C is inserted into equation 1.20 and result is then plugged into equation 1.21 and repeated until C converges. Initially it seems that this method requires more computation than FEP because two equilibrium simulations must be performed for every iteration, however, provided enough disk space is available, the values of U_0 and U_1 can be stored for just two simulations and reused for each iteration. The averages should be more reliable than what is used in FEP because their variance is minimized. As with FEP, the jump from U_0 to U_1 can be divided into smaller steps.

Probably the most frequently used free energy difference method is thermodynamic integration (TI) [42]. This method is based on the idea that the potential energy for the system can be changed to the potential energy of the reference state through some path which does not have to be physical. The path

is dictated by a parameter, λ, such that when $\lambda = 0$ the $U(\lambda, \mathbf{r})$ corresponds the initial state and when $\lambda = 1$ it corresponds to the reference state. The derivative of the free energy with respect to λ can then be found using equations 1.3 and 1.11.

$$\frac{\partial A(\lambda)}{\partial \lambda} = \frac{\int \frac{\partial U(\lambda)}{\partial \lambda} \exp\left(-\frac{U(\lambda,\mathbf{r})}{kT}\right) d\mathbf{r}}{\int \exp\left(-\frac{U(\lambda,\mathbf{r})}{kT}\right) d\mathbf{r}} \tag{1.22}$$

$$= \left\langle \frac{\partial U(\mathbf{r},\lambda)}{\partial \lambda} \right\rangle_{\lambda} \tag{1.23}$$

The free energy difference between two states, $U(\mathbf{r}, 0)$ and $U(\mathbf{r}, 1)$, is

$$\Delta A = \int_0^1 \left\langle \frac{\partial U(\mathbf{r},\lambda)}{\partial \lambda} \right\rangle_{\lambda} d\lambda \tag{1.24}$$

In practice, only a finite number of steps in λ can be taken and a numerical procedure is used to handle the integration. Each step in λ requires an equilibrated average of $\frac{\partial U(\mathbf{r},\lambda)}{\partial \lambda}$. In addition to computing well converged averages at each λ, enough values of λ must be used to ensure that the integration converges as well. Another difficulty with TI is that the path must be chosen carefully. If the final potential energy corresponds to an ideal gas, $U(\mathbf{r}, 1) = 0$, then the integrand should also be zero. Otherwise, overlapping atoms will cause statistical problems.

All of these free energy difference methods rely on using intermediate states between the system of interest and the reference state. They exploit the fact ΔA is a state function which is independent of the path used to go from one state to the other so that path can be nonphysical. Increasing the number of intermediate steps along the path increases the overlap of the configuration partition functions which increases the accuracy. However, at each step, an equilibrium simulation must be performed. A variant of both FEP and TI, called slow growth [43, 44, 45] decreases the number of moves in each simulation to one while increasing the number of increments between the states. In

both cases the expressions for free energy difference become

$$\Delta A = \sum_{i=1}^{n-1} U(\lambda_{i+1}, \mathbf{r}^{(i)}) - U(\lambda_i, \mathbf{r}^{(i)}) \tag{1.25}$$

where $\lambda_i = i/n$. The configuration $\mathbf{r}^{(i)}$ advances to $\mathbf{r}^{(i+1)}$ by either a MC or MD step with the new potential energy $U(\lambda_{i+1}, \mathbf{r})$. How the potential energy depends on λ is arbitrary as long as the function which bridges $U(\lambda_1, \mathbf{r})$ and $U(\lambda_n, \mathbf{r})$ is continuous. In this scheme, the coordinates are not given any time to equilibrate to the new potential energy and a lag develops between the configuration and the potential energy.

A different view of this type of switching was taken by Watanabe and Reinhardt [46]. Instead of calculating the free energy difference in the canonical ensemble, they computed entropy in the microcanonical ensemble. Over an MD simulation, the potential energy is slowly changed by small increments every time step from the system of interest to a reference state with a known entropy, $S(E)$. If the potential energy is changed slowly the phase volume of the initial and final volumes will be identical. Thus, the total energy, E, of the final state can be used to compute $S(E)$ which will be the same entropy as the initial state. As the number of steps between the states are increased, the value of $S(E)$ converges.

Building on this idea of adiabatic switching, Reinhardt and Hunter [47] developed a method for the canonical ensemble, the finite-time variational (FTV) method, which was later expounded by Hunter, Reinhardt and Davis [48]. They point out that changing the potential energy while the coordinates remain frozen does work, w, on the system. Allowing the coordinates to change according to the new potential energy absorbs heat, q. Taken together, these two processes result in an overall change in the energy of the system: $\Delta E = q + w$, by the first law of thermodynamics. The second law demands that $q \leq T\Delta S$,

thus

$$\Delta A = \Delta E - T\Delta S \leq w \tag{1.26}$$

where the equality holds for a reversible process. That is, the work done on the system to change it from the initial state to the reference state is an upper bound to the free energy difference between the initial and reference states. Equation 1.25 in this new light becomes

$$\Delta A_{init \to ref} \leq w_{init \to ref} = \sum_{i=1}^{n-1} U(\lambda_{i+1}, \mathbf{r}^{(i)}) - U(\lambda_i, \mathbf{r}^{(i)}). \tag{1.27}$$

The lower bound can also be found by performing a simulation of the reverse process.

$$\begin{aligned} \Delta A_{init \to ref} = -\Delta A_{ref \to init} &\geq w_{ref \to init} \\ &= -\sum_{i=1}^{n-1} U(\lambda_{n-i+1}, \mathbf{r}^{(n-i)}) - U(\lambda_{n-i}, \mathbf{r}^{(n-i)}) \end{aligned} \tag{1.28}$$

Increasing n makes each process more reversible thereby decreasing the discrepancy between the bounds until, at large enough n, they converge. For the bounds to hold, each must be computed as an ensemble average and simulations must begin with equilibrated configurations.

This method has several advantages over the others discussed in chapter. Because both upper and lower bounds to ΔA can computed, the level of accuracy (systematic error) can easily be determined. This accuracy can be systematically improved by increasing the length of the simulation or, as we will show later, by optimizing the switching path and the choice of reference state. Furthermore, time-consuming equilibrium averages at all intermediate values of λ are not required.

1.3 Summary

The goal of work presented in this thesis is to develop a method for gaining more knowledge about the free energy landscape of atomic clusters throughout the temperature range in which the cluster remains intact. This range includes low temperatures at which solid clusters are the most stable, higher temperatures at which liquid clusters dominate, and intermediate temperatures at which both types coexist. For some clusters, other phases also occur such as surface-melted clusters and multiple solid phases. In order to fully understand this landscape, the free energy of each phases needs to be calculated separately. Free energy methods which rely on histograms such as the Landau free energy and multihistogram methods rarely allow for such separation because finding an order parameter which results in zero overlap of the states is unlikely. The SHA method does allow one to exclusively sum over states of one phase but it has many approximations and requires extensive knowledge of the potential energy surface making it difficult to generalize to other systems. At coexistence temperatures, the free energy difference methods which rely on equilibrium averages also fail to result in separate solid and liquid free energies because the barrier between the states is low enough that both states are sampled while collecting data for the average. The slow growth methods, however, hold some promise because only the phase of the initial configuration matters. This initial configuration can be constrained to the phase of interest. Among the slow growth methods, the FTV method stands out as the strongest candidate as it is performed in the canonical ensemble and provides upper and lower bounds to the true free energy. What we will show in this thesis is that the FTV method combined with the appropriate reference states does allow one to calculate the free energies of solid and liquid states separately throughout the coexistence range.

The layout of this thesis is the following: In the next chapter, we provide a more detailed description of the FTV method in general, define some terms and illustrate how the upper and lower bounds converge to the correct result. Chapter 3 is a digression regarding MC simulations in general in which we show that the established practice of dynamically adjusting the maximum step size can result in erroneous results. In chapter 4, we present four different reference states for atomic clusters, two of which are appropriate for solid clusters and two for liquid clusters. We show which of each pair is optimal for FTV calculations. The last chapter contains results for both solid and liquid phases LJ_{55} and a comparison to the results of Doye and Wales. Lastly, we illustrate how this method can be extended to molecular clusters such as $(H_2O)_{20}$ to determine which isomer is the most stable at a given temperature.

Chapter 2

THE FINITE TIME VARIATIONAL METHOD

In the previous chapter we showed how the upper and lower bounds to a free energy difference between two states , ΔA, can be computed using the finite time variational (FTV) method. In this chapter, we describe the FTV method more fully and define terms which will be used frequently to describe results presented in later chapters. We also point out some pitfalls, illustrated with a trivial example, that can easily be avoided once recognized. Theoretically, the FTV method can be used with either MC or MD simulations. MC simulations are generally easier to implement in the canonical ensemble than MD. Additionally, changing the potential energy within an MD simulation while trying to maintain a constant temperature complicates the simulation further. For these reasons, only MC simulations are used in all of the work presented in this thesis. To ease the notation of this chapter, we limit our description to that of a MC simulation.

2.1 Method

The free energy difference we wish to compute is between our system of interest and a reference state with a known free energy. The system of interest consists of a set of N particles with coordinates $\mathbf{r} = \mathbf{r}_1, \mathbf{r}_2, \ldots \mathbf{r}_N$ which interact through the configurational part of the Hamiltonian $U_{init}(\mathbf{r})$ at constant temperature, T, and a constant volume, V. As mentioned in chapter 1, we restrict our systems to those in which the configurational and kinetic parts of the Hamiltonian are

separable. Thus, we can limit the scope of our simulation to the particle positions. The reference state also has N particles at a temperature, T, but its interaction is $U_{ref}(\mathbf{r})$. The path that bridges the U_{init} and U_{ref} can parametrized as a function of a progress variable λ which varies linearly from 0 to 1. The only constraints of the path are that it is continuous over $[0,1]$ and

$$\lambda = 0; \qquad U(\mathbf{r},\lambda) = U_{init}(\mathbf{r}) \tag{2.1}$$

$$\lambda = 1; \qquad U(\mathbf{r},\lambda) = U_{ref}(\mathbf{r}). \tag{2.2}$$

To compute the upper bound of ΔA, the work done on the system to change U_{init} to U_{ref} is computed by the following procedure. First, an equilibrium MC simulation with U_{init} at fixed T, V is performed from which an equilibrated set of coordinates is extracted. This configuration, $\mathbf{r}^{(1)}$, serves as the initial one for the switching process. The parameterized Hamiltonian for this initial state is $U(\mathbf{r}^{(1)},\lambda_1)$ where $\lambda_1 = 0$. Then, λ is changed by small amount from λ_0 to λ_1 and the work for this change is calculated. In general, the work done on the system to change λ_i to λ_{i+1} is

$$w_i = U(\mathbf{r}^{(i)},\lambda_{i+1}) - U(\mathbf{r}^{(i)},\lambda_i). \tag{2.3}$$

where $\lambda_{i+1} - \lambda_i = 1/n$ and $\lambda_n = 1$. This change in the Hamiltonian is then followed by a Metropolis MC move which updates the coordinates from $\mathbf{r}^{(i)}$ to $\mathbf{r}^{(i+1)}$. The heat absorbed by the system is

$$q_i = U(\mathbf{r}^{(i+1)},\lambda_{i+1}) - U(\mathbf{r}^{(i)},\lambda_{i+1}). \tag{2.4}$$

The sequence is executed $n-1$ times incrementing i by 1 each time. The work done and heat absorbed for the entire process are

$$w_{init\to ref} = \sum_{i=0}^{n-1} w_i \qquad \text{and} \qquad q_{init\to ref} = \sum_{i=0}^{n-1} q_i. \tag{2.5}$$

By the first law of thermodynamics,

$$\Delta E = U(\mathbf{r}^{(n)}, \lambda_n) - U(\mathbf{r}^{(1)}, \lambda_1) = w_{init \to ref} + q_{init \to ref} \tag{2.6}$$

for the process and by the second law, $q_{init \to ref} \leq T\Delta S$ which means the work is an upper bound to the free energy change.

$$\Delta A_{init \to ref} = \Delta E - T\Delta S \leq w_{init \to ref}. \tag{2.7}$$

Examining equation 2.6, we can see that $w_{init \to ref}$ does not have to be computed explicitly and can instead be deduced from the $q_{init \to ref}$ and the energy at start and end of the switching process. This feature is particularly time-saving for Metropolis MC simulations in which the heat at each step must computed anyway (see chapter 1) so $q_{init \to ref}$ can be computed by accumulating q_i for all the accepted moves during the switching process. If only one particle is moved, q_i will only depend on the parts of potential energy that are a function of that particle so only those parts must be computed. To get w_i on the other hand, without a sophisticated code tailored specifically to the switching path, the entire potential energy must be included even if only one particle moved. Take the case of a pair potential in which U(r) depends only on all the pair distances and on λ, $U(\mathbf{r}, \lambda) = \sum_{a=1}^{N} \sum_{b>a}^{N} U_p(\mathbf{r}_a, \mathbf{r}_b, \lambda)$. For one MC move in which only atom j moves,

$$w_i = \sum_{a=1}^{N} \sum_{b>a}^{N} [U_p(\mathbf{r}_a^{(i)}, \mathbf{r}_j^{(i)}, \lambda_{i+1}) - U_p(\mathbf{r}_a^{(i)}, \mathbf{r}_j^{(i)}, \lambda_i)] \tag{2.8}$$

and

$$q_i = \sum_{a=1}^{N} [U_p(\mathbf{r}_a^{(i)}, \mathbf{r}_j^{(i+1)}, \lambda_{i+1}) - U_p(\mathbf{r}_a^{(i)}, \mathbf{r}_j^{(i)}, \lambda_{i+1})]. \tag{2.9}$$

Equation 2.8 requires $2N(N-1)$ evaluations of E whereas equation 2.9 needs only $2N$.

The lower bound to $\Delta A_{init \to ref}$ can be determined by computing the work for the reverse process. For this calculation, an equilibrated configuration from a simulation with U_{ref} is used as the initial set of of coordinates and the initial Hamiltonian is $U(\mathbf{r}^{(1)}, \lambda_n)$. The heat and work are computed just as in equations 2.3-2.5 except λ_{i+1} and λ_i are replaced with λ_{n-i} and λ_{n+1-i} respectively.

$$w_{ref \to init} = \sum_{i=0}^{n-1} = U(\mathbf{r}^{(i)}, \lambda_{n-1-i}) - U(\mathbf{r}^{(i)}, \lambda_{n-i}) \tag{2.10}$$

$$q_{ref \to init} = \sum_{i=0}^{n-1} = U(\mathbf{r}^{(i+1)}, \lambda_{n-1-i}) - U(\mathbf{r}^{(i)}, \lambda_{n-1-i}) \tag{2.11}$$

The same arguments used for the upper bound can be applied here to show that the work done for this process with opposite sign is a lower bound to free energy of the forward process or

$$\Delta A_{ref \to init} = -\Delta A_{ref \to init} \geq -w_{ref \to init} \tag{2.12}$$

2.2 *The FTV Method illustrated with a simple example*

The equality in the second law, $q \leq T\Delta S$, holds when a process is reversible. Our switching process will approach reversibility as $n \to \infty$ so increasing n brings the bounds closer to each other and the actual value of ΔA. We can illustrate the convergence of upper and lower bounds with a simple example in which ΔA can be found analytically. We start with a particle in a harmonic well and switch to an ideal gas particle contained by a hard wall sphere to a fixed volume.

The partition function for an ideal gas particle constrained to a sphere of radius, R_c, is

$$Q_{ig} = 4\pi \int_0^{R_c} r^2 dr = \frac{4\pi}{3} R_c^3 \tag{2.13}$$

where spherical coordinates are used for the integration. For a particle in a harmonic well the partition function is

$$\begin{aligned} Q_{hrm} &= \iiint_{-\infty}^{\infty} \exp(-k_{sp}(x^2+y^2+z^2)/kT)dxdydz \\ &= 4\pi \int_0^{R_c} r^2 \exp(-k_{sp}r^2/kT)dr \\ &= \left(\sqrt{kT\ \pi/k_{sp}}\right)^3 \end{aligned} \tag{2.14}$$

We want to keep the simulation at fixed volume so the particle will be constrained by the hard wall sphere throughout the switching process. This means the limits of integration for Q_{hrm} change to $[0, R_c]$. If R_c is chosen large enough, this change of limits does not significantly affect the value of Q_{hrm} or its corresponding free energy. For instance, when $kT = 1$ and $k_{sp} = 1$ the difference between $(\sqrt{kT\pi})^3$ and a numerical evaluation of equation 2.14 with $R_c = 4$ is of the order 10^{-6}. The difference in the free energy is even smaller, of the order 10^{-7}. Given these negligible differences, we are justified in using a fixed volume of $\frac{4\pi}{3}(R_c = 4)^3$ with $kT = 1$ and $k_{sp} = 1$.

We begin the simulation by randomly placing the particle in the sphere and letting it equilibrate under the harmonic Hamiltonian, $U_{hrm}(r) = k_{sp}r^2$, for 50,000 MC steps. The hard wall sphere is imposed by rejecting any move that results in the particle exceeding a distance of R_c from the origin. We use a simple linear switching path, $U(r,\lambda) = (1-\lambda)U_{hrm}(r)$ so that at $\lambda = 1$ the only interaction left is the one implicit in the confinement of the particle in the sphere. The reverse simulation is started the same way except the equilibration, with $U_{ig}(r) = 0$, essentially amounts to choosing random positions anywhere within the sphere. Ensemble averages of the work for each direction are generated from 100 replicas. In figure 2.1, we have plotted $\langle w_{hrm\to ig}\rangle$ and $\langle -w_{ig\to hrm}\rangle$ from separate calculations of increasing n. The error bars represent the standard error in the mean of the ensemble average. They are joined

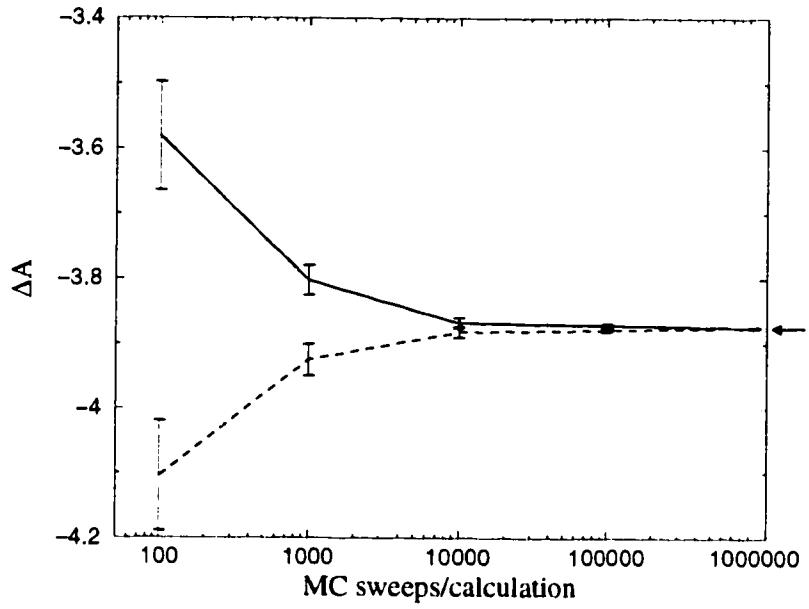

Figure 2.1: Convergence of the upper and lower bounds to $\Delta A_{hrm \to ig} = A_{hrm} - A_{ig}$. The solid line joins the $w_{hrm \to ig}$ points and the dashed line joins the $-w_{ig \to hrm}$ points. The arrow on the right side of the plot shows the analytical value of $\Delta A_{hrm \to ig}$. The error bars indicate the standard error in the mean.

by lines to illustrate the upper and lower bounds to $\Delta A_{hrm \to ig} = A_{hrm} - A_{ig}$. This figure shows quite clearly that the bounds to the free energy change converge as the number of MC steps within the calculation is increased. We may also check that they are converging to the correct value because we know the analytical values of both A_{hrm} and A_{ig}. The arrow on the right side of the plot shows the analytical value of $\Delta A_{hrm \to ig}$.

Using this simple example, we can define some terms that we will use throughout this thesis. Our estimate of ΔA will come from the average of the upper and lower bounds for the largest n used. In this example, at 10^5 MC steps, $\Delta A_{est} = -3.87454 \pm 0.00598$ but at 10^6 steps the average is -3.87422 ± 0.00055, a number closer to the analytical value of -3.87420. The total error for these estimates in comprised of two parts: the statistical error and the systematic

error. The source of the statistical error, δw, is the fluctuations in the ensemble averages and is determined from the standard error in the mean. The systematic error results from the finite number of steps taken between the two states and can be gauged by the difference in the upper and lower bounds. Both of these errors, as can be seen in figure 2.1, decrease with increasing n. We define the total error, δA_{tot}, as

$$\delta A_{tot} = \frac{1}{2}(\langle w_{init \to ref} \rangle + \delta w_{init \to ref} - (\langle w_{ref \to init} \rangle - \delta w_{ref \to init})) \tag{2.15}$$

When two different types calculations are both used to estimate A_{init}, the one which achieves a smaller value of δA_{tot} for the same n is called more efficient. When an FTV calculation provides results with δA_{tot} less than or equal to some predefined acceptable error, we call the calculation converged.

Throughout this thesis we will discuss ways of improving the efficiency of an FTV calculation. Hunter *et al* [48] showed that for a two dimensional Ising model the switching path can be optimized to produce the best efficiency. In chapter 4, we will show that the choice of reference state can also greatly affect the efficiency. Lastly, we have found that the maximum step size parameter of MC simulations can also influence the efficiency. This point is discussed briefly in the next section and then more thoroughly in chapter 3.

2.3 Avoiding Problems

The FTV method should succeed in calculating any free energy difference. It may fail to converge within an acceptable amount of MC steps but given enough time it would eventually give the correct result. Even for inefficient calculations that have not converged, it provides a reliable result within the confines of its total error. A failure of the FTV method would result in either the true value of ΔA lying outside the bounds or the bounds crossing. A failure can occur in two ways: if the calculation is started with configurations that are

not representative of an equilibrium ensemble or if ensemble average of the work is taken over an inadequate number of replicas. Both cases represent the same underlying problem of allowing fluctuations to compromise the ensemble average.

One other possible failure of the FTV method is related to maximum step size parameter of MC simulations. In metropolis MC, a trial move is made for a particle by displacing the particle a random distance up to some maximum, d, from its original position. The size of d is chosen to promote efficient sampling. At least two texts on molecular simulation advise dynamical adjustment of this parameter within the simulation based the ratio of accepted to total MC moves. We have found that such adjustment during an FTV calculation does give efficiently converging upper and lower bounds but they converge to an incorrect value for ΔA. This problem is not unique to the FTV method. We have also found that adjusting d within a thermodynamic integration also gives specious results. We devote the next chapter to this issue and give instructions for choosing d for both equilibrium simulations and FTV calculations.

2.4 Extensions to the FTV method

In the last few years, two improvements to general free energy difference methods have been suggested. Though they can applied to any the methods, both of these extensions are particularly well-suited for the FTV method. The first was offered by Jarzynski [49, 50] who showed that a closer estimate of ΔA can be made by averaging over $\exp(-w/kT)$ instead of just w. He derived the relation,

$$\Delta A = -kT \ln \langle \exp(-w/kT) \rangle , \tag{2.16}$$

in two different ways, one considered the deterministic evolution of the system and the in other, the evolution was stochastic and governed by a master

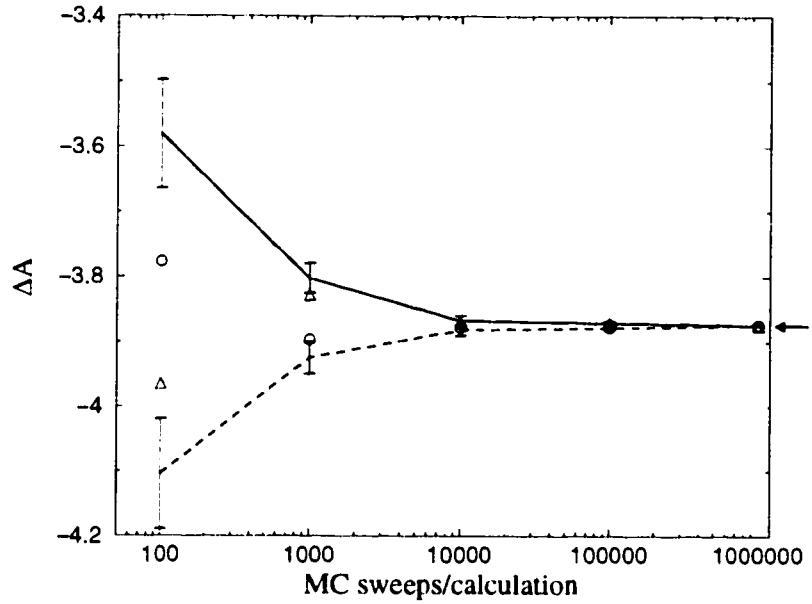

Figure 2.2: Comparison of estimates of $\Delta A_{hrm \to ig}$ using $\langle w \rangle$ and $-kT \ln\langle \exp(-w/kT) \rangle$. The solid line joins $\langle w_{hrm \to ig} \rangle$ points, the dashed line joins $-\langle w_{ig \to hrm} \rangle$ points, the triangles are $-kT \ln\langle \exp(-w_{hrm \to ig}/kT) \rangle$ and the circles are $-kT \ln\langle \exp(-w_{ig \to hrm}/kT) \rangle$. The arrow on the right side of the plot shows the analytical value of $\Delta A_{hrm \to ig}$.

equation. Unlike equation 2.7, equation 2.16 is not a bound and though, theoretically, it holds for any switching time, it will not hold when the fluctuations in w are much greater than kT, which does occurs for short switching times. In figure 2.2, we compare the convergence for our simple harmonic example using $\langle w \rangle$ and $-kT \ln \langle \exp(-w/kT) \rangle$. The Jarzynski results do violate the bounds at small n when the fluctuations are large but at every n, they are closer to the actual value of ΔA then the simple average of the work. At large n, however, the difference between the simple average and the exponentiated average is less than the statistical uncertainty.

Quite recently, Koning, Antonelli and Yip [51] introduced an extension to slow growth methods called reversible scaling (RS) in which the free energy

can be computed for many temperatures from one simulation. Going back to one definition of the free energy at temperature, T_0, and coordinates, $\mathbf{r}$,

$$A_0(T_0) = -kT_0 \ln\left(\int \exp(-U_0(\mathbf{r})/kT_0)d\mathbf{r}\right) \tag{2.17}$$

If the Hamiltonian is parametrized as we did in the harmonic example with a coefficient, $U(\mathbf{r},\lambda) = c(\lambda)U_0(\mathbf{r})$, then the free energy of a state with Hamiltonian, $U(\mathbf{r},\lambda)$, is

$$A(T_0,\lambda) = -kT_0 \ln\left(\int \exp(-U_0(\mathbf{r})/kT)d\mathbf{r}\right) \tag{2.18}$$

where $T = T_0/c(\lambda)$. From the FTV method, we know that free energy difference between the two states is bounded by the work, w_λ, done on the system by changing the Hamiltonian, $\Delta A(T_0,\lambda) = A(T_0,\lambda) - A_0(T_0) \leq w_\lambda$. Using these equations, the free energy of a system with Hamiltonian, U_0, at a temperature, T, can be written as

$$\begin{aligned} A_0(T) &= \frac{T}{T_0}(A_0(T_0) + \Delta A(T_0,\lambda)) \\ &\leq \frac{T}{T_0}(A_0(T_0) + w_\lambda) \end{aligned} \tag{2.19}$$

The bound is only guaranteed to hold for exact values of $A_0(T_0)$ but because that value will most likely come from an FTV calculation, it will have some error. The lower bound to $\Delta A(T_0,\lambda)$ cannot be found by doing the reverse calculation. Such a calculation would take its initial configuration from an intermediate step in switching calculation and not from an equilibrated sample.

We applied this method to the example of a harmonic particle switched to an ideal gas particle described earlier. The initial temperature, T_0 was set equal to 1.0 as were k and k_{sp}. The volume of the simulation was constrained to a sphere of radius 4.0. An FTV simulation for the forward process was run with the added feature that at several values of λ the work up to that point was saved. Ensemble averages of the total work as well as of the work up

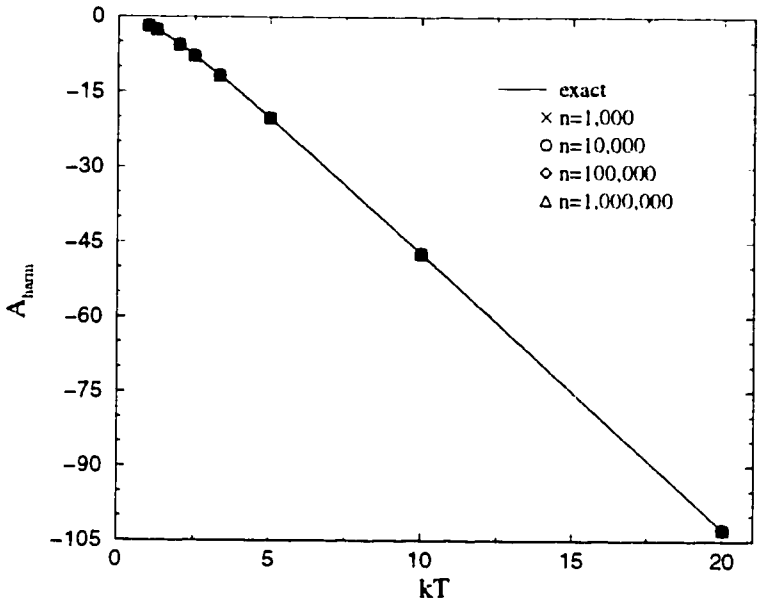

Figure 2.3: The free energy of a harmonic particle confined to a sphere of radius 4.0 as calculated using the RS method. k and k_{sp} are both equal to one.

to the selected intermediate points were computed. The average of the total work was used to estimate $A_0(T_0)$ and the averages of the work at other points were used to find $A_0(T)$. The results for several different simulation lengths, n, are plotted in figure 2.3. The exact results come from numerical integration of $-kT \ln\left(\int_0^{R_c=4.0} r^2 \exp(-k_{sp}r^2/kT)dr\right)$. Unlike the simple FTV example with $T = 1.0$, at higher T, the bounds of the container have a non-negligible effect on the free energy. For all the values of n and T, we found excellent agreement. Even for the smallest n and largest T, the difference between the computed and exact values was only 0.104. Though this test was on a very small system, it may well be worth trying on more sophisticated systems.

Chapter 3

ADJUSTING THE MAXIMUM STEP SIZE IN MONTE CARLO SIMULATIONS

The previous chapter briefly mentioned that the FTV method can fail when the maximum step size in a MC simulation is adjusted based on the ratio of accepted moves to total moves. In this chapter, we explain and illustrate this point. In the first section, reasons for making such an adjustment of the step size are given as well as a the origins of how it came into common practice. In the next section, we show how systematic error is introduced into the results of both FTV and thermodynamic integration calculations as a result of this dynamic adjustment. Furthermore, we will demonstrate that the problem is not limited to free energy difference calculations but can affect equilibrium properties as well. Finally, reasons for the error are discussed as well as the conditions under which the problem is most egregious. The contents of this chapter are also discussed in [1].

3.1 Why adjust the maximum step size?

In a Metropolis MC simulation, at each step, a particle is displaced by a random amount in any direction up to some maximum, d. This is the maximum step size. It affects how often MC moves are accepted. If d is large, the larger moves allow more phase space to be explored but the moves are rarely accepted. Conversely, if d is small, moves are accepted quite often but many moves are need to adequately sample phase space. In the early history of Metropolis MC,

the acceptance rate was found to play a role in how well phase space was explored. One of the first papers to discuss it was by Wood and Jacobson [52] who defined a measure of optimization called the "calculation rate". It is based on on the root mean square displacement per configuration. They found that this measure varies with the rejection ratio, the ratio of rejected moves to total moves. For a system of hard sphere atoms subject to periodic boundary conditions the calculation rate was greatest when the rejection ratio was quite high, ~ 0.9. Almost two decades later, Streett and Tildesley [53], in their work on hard diatomic molecules, sought to optimize their MC simulations by using the best value of d. However, they interpreted the ratio of Wood and Jacobson as an acceptance ratio of 0.5 to 0.7. In order to maintain that ratio, they adjusted d within the simulation. This is the earliest reference in the literature that we can find to dynamic adjustment of d. Since that publication, two widely used texts on molecular simulation [54, 55] also advise dynamic adjustment of d. Gauging how often simulators use this method is difficult because it is a detail that is rarely published but given its presence in textbooks and from conversations with other scientists, we believe that it has become a common practice.

3.2 Adjusting d in a free energy difference calculation

3.2.1 The FTV method

In the FTV method, dynamic adjustment of d takes on a special significance. When the Hamiltonian is changed over the course of the simulation, d can vary greatly. As an example, we chose as our initial system, a cluster of 13 Lennard-Jones atoms, LJ_{13}, contained in a sphere centered on the center of mass of the cluster. The reference state, described in great detail in the next chapter, is a set of 13 ideal gas atoms with the same volume constraint. The parameterized

Hamiltonian is

$$H(\mathbf{r}, \lambda) = (1 - \lambda)^3 H_{LJ_{cm}}(\mathbf{r}) \tag{3.1}$$

where $H_{LJ_{cm}}$ is from equation 4.5 and $\mathbf{r}$ is the set of all coordinates. The temperature, $kT/\epsilon = 0.37$, is chosen such that the cluster remains in a liquid state. The radius of the sphere, $R_c = 2.94\sigma$, was chosen to be large enough that it does not apply an artificial pressure on the cluster yet small enough that evaporation events are unimportant [36]. An ensemble of sixty replicas of LJ_{13} was generated by extracting configurations from an equilibrium simulation every 500,000 MC sweeps. For a warm-up period of 5,000 sweeps, the maximum step size is allowed to change every 50 sweeps according to Allen and Tildesley's scheme [54]:

ratio = (number of accepted moves)/(number of total moves)
if ratio > 0.50 **then**
  $d = d * 1.05$
else
  $d = d * 0.95$
end if

After the warm-up period, d remains constant. The ensemble for the reverse simulation was generated by randomly selecting positions for each configuration subject to the volume constraint and equilibrating according the reference state Hamiltonian for 5,000 sweeps where $d = 0.5R_c$ remains constant.

An FTV calculation is a special case of MC simulation because the Hamiltonian changes with the simulation. If d is held constant at a value appropriate for the initial interaction while $H_{LJ_{cm}}$ is switched off, the acceptance ratio changes dramatically over the switching path as shown in figure 3.1a for one replica. Conversely, if the acceptance ratio is maintained by adjusting d every 50 sweeps, it varies by as much as half the radius of the constraining volume

over the switching path as shown in figure 3.1b.

Figure 3.2 shows how the results of the FTV calculation are affected by how d is treated. The solid lines are the upper and lower bounds to ΔA when d is adjusted every 50 sweeps. The dashed lines are the bounds when d is held constant at a value appropriate for the initial interaction, $d = 0.11\sigma$. The bounds converge more quickly when d is dynamically adjusted but they converge to a distinctly different value than when d is held constant. The values of ΔA for each calculation along with their total errors are listed in table 3.1. In order to improve the convergence of the constant d calculation, $d = 0.5\sigma$ was used to obtain this value of ΔA. Dynamic adjustment of d introduces a systematic error of 0.119ϵ. It is easy to assume that the problem can be attributed to the fact that the atomic interaction changes throughout the simulation. However, we will show that this problem is not unique to the FTV method.

Table 3.1: ΔA and its total uncertainty, calculated using the FTV and TI methods, with the maximum step size held fixed or adjusted every 50 sweeps. All values are in units of ϵ. The uncertainty in the FTV calculation is computed from equation 2.15 and the error in the TI calculation is the standard error in the mean in the integrand which greatly exceeds the estimated error due to discretization of the integral.

	FTV	uncertainty	TI	uncertainty
d constant	12.9568	0.0026	12.9564	0.0033
d adjusted	13.0758	0.0043	13.2863	0.0025

3.2.2 Thermodynamic integration

One might guess that other methods of calculating ΔA that rely on equilibrium averages rather than changing the Hamiltonian every step might not be affected by dynamically adjusting d because d would not change much over

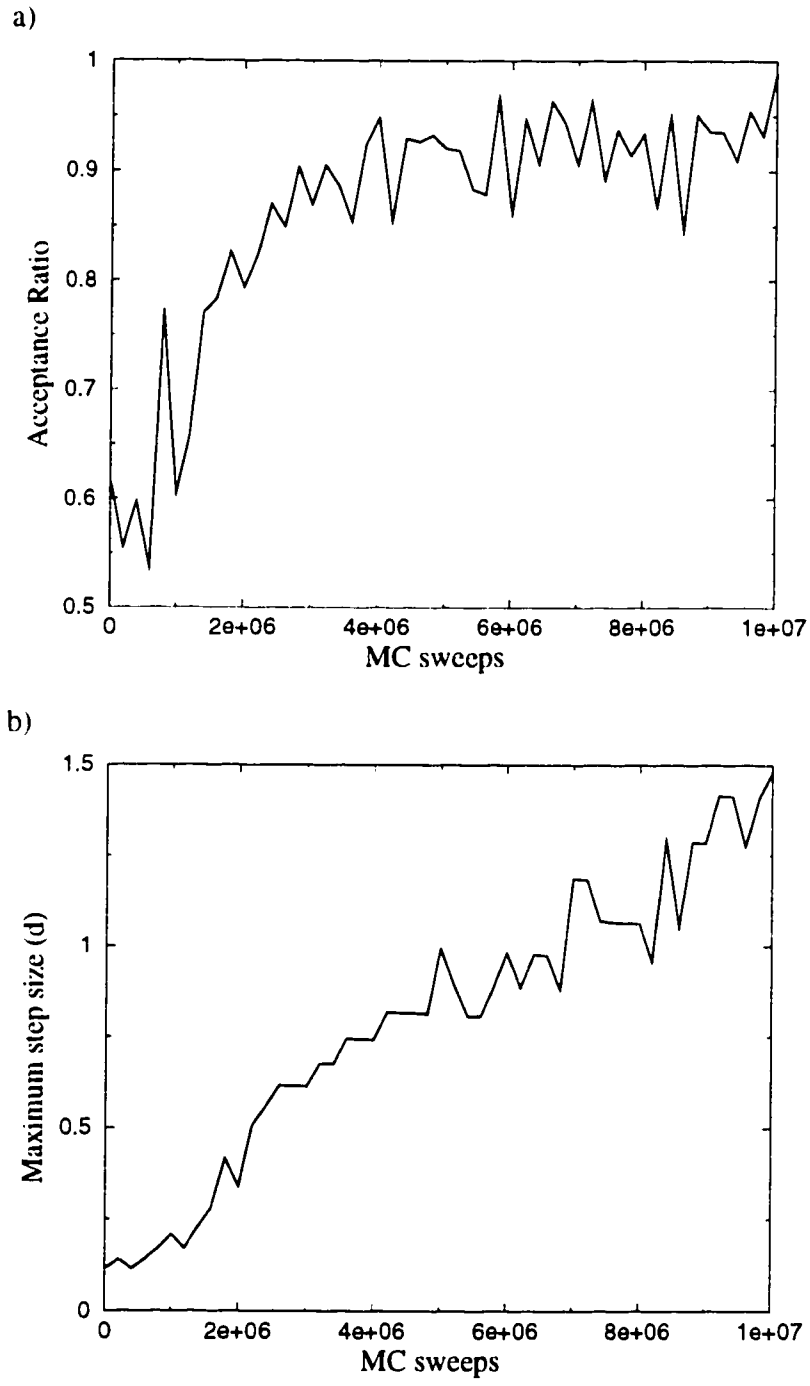

Figure 3.1: a) The acceptance ratio as a function MC sweep in an FTV calculation with d held constant at 0.11σ and b) d when it is allowed to adjust to maintain an acceptance ratio of 0.5.

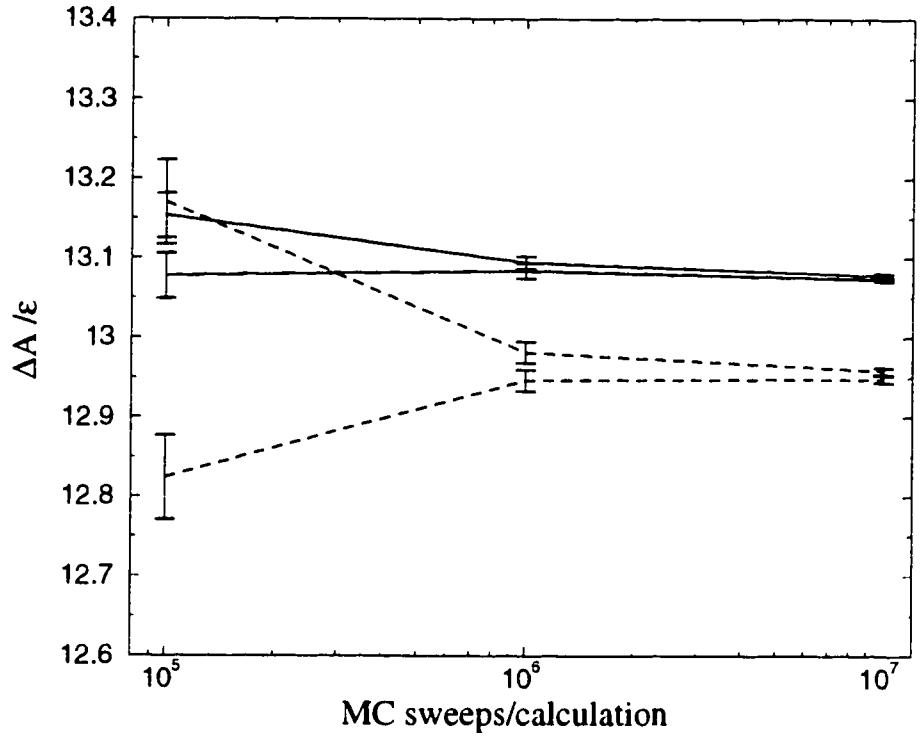

Figure 3.2: Upper and lower bounds to ΔA when d is dynamically adjusted (solid lines) and when it is held constant at 0.11σ (dashed lines).

the course of the simulation. To test this assumption, we calculated ΔA again for the LJ_{13} system described above using thermodynamic integration (TI) in which the free energy difference is given by

$$\Delta A = \int_0^1 \left\langle \frac{\partial H(\mathbf{r};\lambda)}{\partial \lambda} \right\rangle_\lambda d\lambda. \tag{3.2}$$

In order to avoid the overlap of atoms as $\lambda \to 1$, we parameterized the integration path according to

$$H(\mathbf{r};\lambda) = [1 - c(\lambda)]\, H_{LJcm}(\mathbf{r})$$

where $U_{LJ}(\mathbf{r})$ of equation 4.1 was rewritten as

$$U(r_{ij}) = 4\epsilon \left[\left(\frac{\sigma}{r_{ij} + c(\lambda)} \right)^{12} - \left(\frac{\sigma}{r_{ij}} \right)^{6} \right],$$

r_{ij} is the distance between any two atoms i and j and $c(\lambda) = \lambda^2(3 - 2\lambda)$.

The integral in equation. (3.2) was discretized into 80 equally spaced steps in λ. At each step, the average in the integrand was taken over 7 runs. Each simulation consisted of three parts: first, 5000 MC sweeps were performed in which d was equilibrated by adjusting every 50 sweeps, secondly, $500,000$ further sweeps were performed to equilibrate the configuration, and finally, statistics were gathered over 3×10^7 production sweeps.

Two sets of simulations were run. In the first set, d was held fixed after the initial 5000 sweeps in which it was equilibrated. In the second set, the adjustment of d every 50 sweeps was continued throughout the configuration equilibration and production periods. The integrands for both these sets are plotted in Fig. 3.3 as a function of λ. For most values of λ the data for the two sets are indistinguishable. The largest discrepancy occurs when λ is at intermediate values. Table 3.1 shows the TI results when these curves are integrated using Simpson's rule to obtain ΔA. The combined uncertainties in ΔA due to discretization of the integral and statistical error in the ensemble

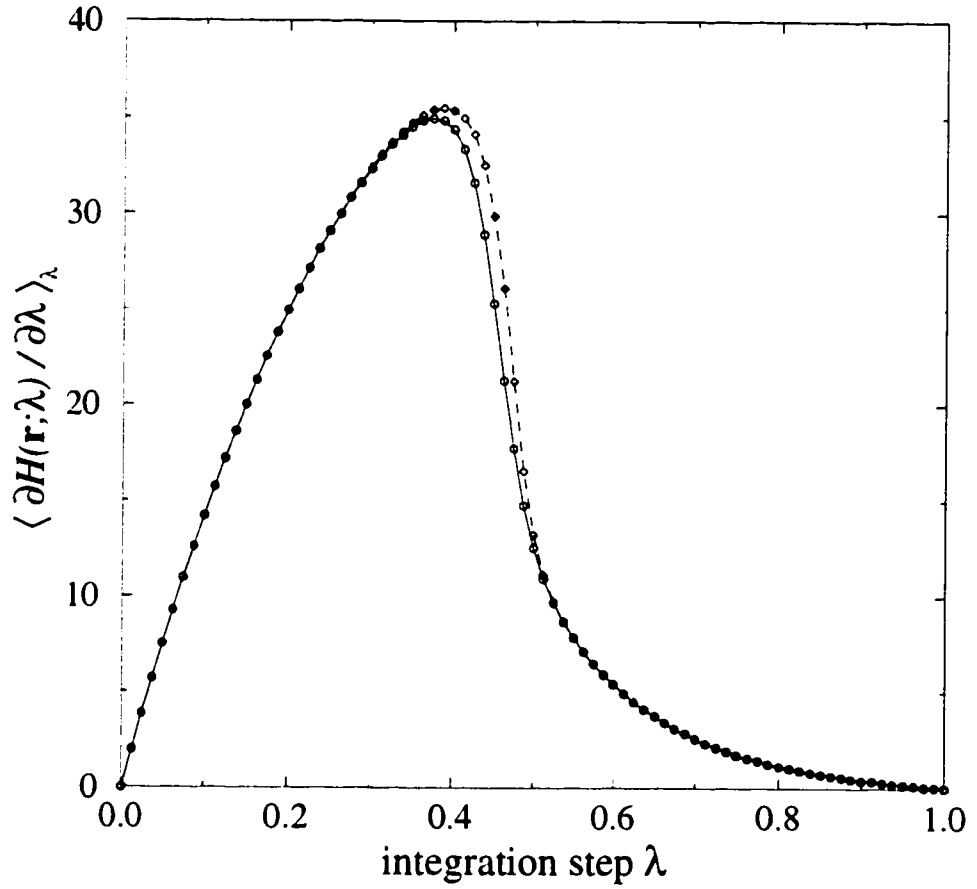

Figure 3.3: The integrand for TI [equation. (3.2)] at 80 points between LJ_{13} and an ideal gas in a sphere of radius 2.94σ at $kT/\epsilon = 0.37$. Solid line: constant d; dashed line: d adjusted every 50 MC sweeps.

averages amount to about 0.02%. In contrast, ΔA changes by 2.5% when d is adjusted every 50 sweeps instead of being held fixed. A greater discrepancy than was found with the FTV method. This shift corresponds to the area between the curves in Fig. 3.3.

3.3 Other systems affected by dynamic adjustment of d

The systematic error incurred by using dynamic adjustment of d is not limited to free energy difference calculations. However, these types of calculations involve the system passing through a phase transition. A crude approximation of the same type of transition can be modeled with a single particle bounded by a one-dimensional Lennard-Jones well,

$$U(x) = 4\epsilon \left[(\sigma/x)^{12} - (\sigma/x)^{6} \right], \quad 0 \leq x \leq 5\sigma,$$

with $U(x) = \infty$ outside this range. There is a single minimum at $x = 2^{1/6}\sigma$, steep repulsion towards $x = 0$, and an increasingly flat region towards the infinite wall at $x = 5\sigma$. The canonical average of U,

$$\langle U \rangle = \int_0^{5\sigma} U(x) e^{-U(x)/kT} dx \Big/ \int_0^{5\sigma} e^{-U(x)/kT} dx,$$

where kT/ϵ is the reduced temperature, can be calculated to arbitrary precision by quadrature in this simple case. Fig. 3.4(a) compares the exact result with MC ensemble averages. At each temperature, the initial position and maximum step size were $x = 1.5$ and $d = 0.1$. An equilibration of 10^6 steps was performed, followed by 10^7 production steps. The standard error in the mean (i.e. statistical uncertainty in $\langle U \rangle$) over 15 such runs at each temperature was typically in the range $5 \times 10^{-5}\epsilon$ to $3 \times 10^{-4}\epsilon$.

When d was allowed to change during the equilibration process but was held fixed during production, $\langle U \rangle$ agreed with the exact value, to within the standard error in the mean, for 19 of the 23 temperatures plotted in Fig. 3.4(a), and

only one point fell slightly outside twice the standard error. However, as the plot shows, adjusting d every 25 steps during production caused a pronounced deviation which, though smaller, was still clear when d was adjusted every 100 steps. At $kT/\epsilon = 0.25$ we found that agreement to within the statistical error (about 0.06%) was only obtained when d was adjusted less frequently than every 900 steps.

A change in d constitutes a temporary loss of detailed balance, and one might suspect that this introduces an error. However, we have found that *predetermined* schedules, in which d changes linearly, sinusoidally, or even randomly with the MC step number, do not produce systematic deviation from the exact solution [56]. In fact, strict detailed balance is an unnecessarily strong condition for obtaining the correct sampling distribution [57]. The problem with dynamic adjustment of d lies in the use of local information, relating to the actual recent history of an individual member of an ensemble, to change the transition matrix.

Adjusting d causes $\langle U \rangle$ to be underestimated. The configuration point stays disproportionately long in the vicinity of the minimum. This interpretation is confirmed by Fig. 3.4(b), where the ratio of the probabilities $p(x > 2\sigma)$ and $p(x \leq 2\sigma)$ is plotted. The exact value was obtained by quadrature from

$$p(a \leq x \leq b) = \int_a^b e^{-U(x)/kT} dx \Big/ \int_0^{5\sigma} e^{-U(x)/kT} dx.$$

For x near the minimum of the potential, dU/dx is relatively large and attempted moves are often rejected. Consequently, d is adjusted downwards and a larger number of steps is then required to escape from this region. Conversely, approaching $x = 5\sigma$, where $U(x)$ is flatter, the Boltzmann weight is relatively insensitive to x, and d can increase, enabling the system to leave this region in fewer steps, thereby undersampling it relative to the vicinity of the minimum. The more frequently d is adjusted, the more correlated it becomes

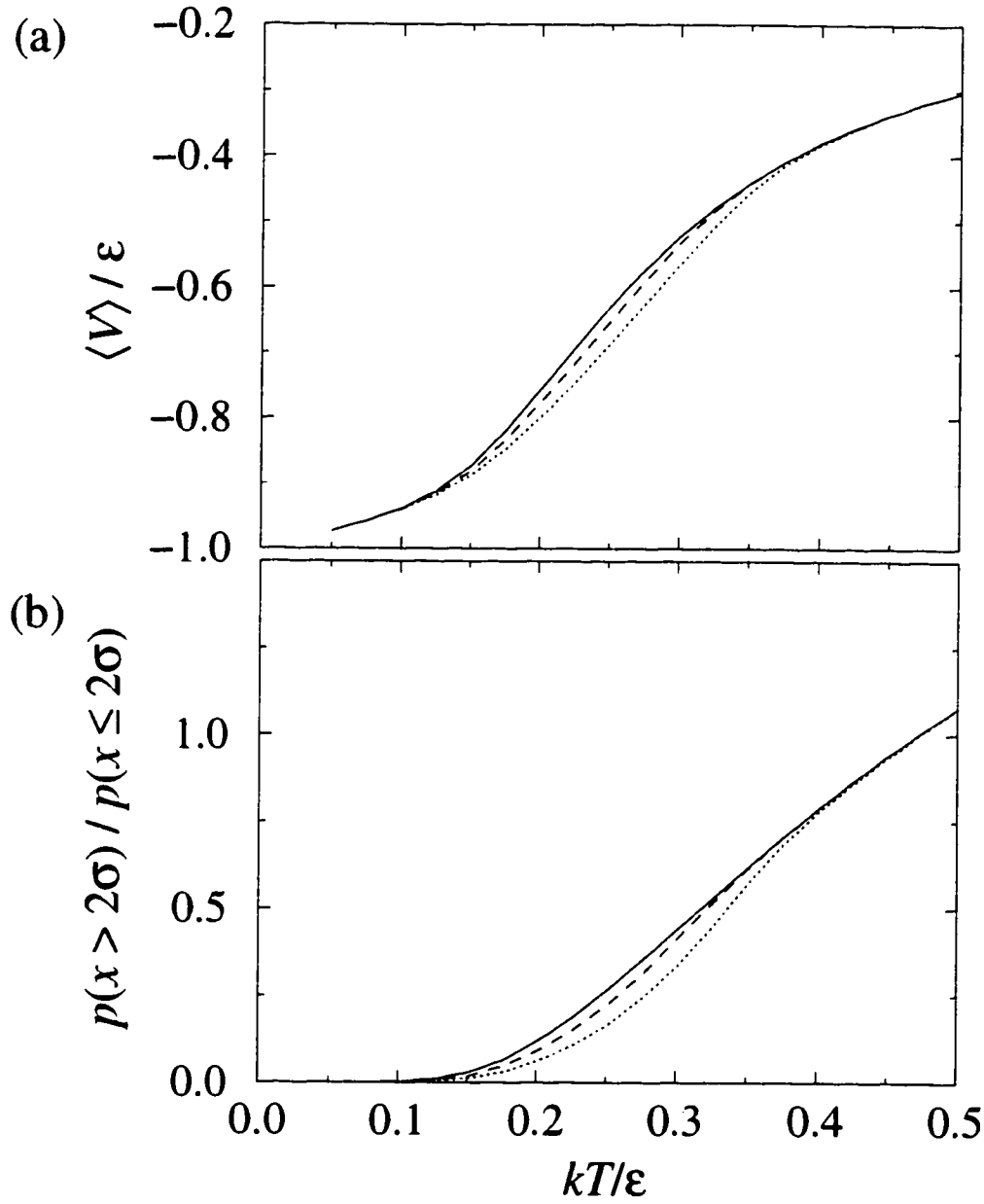

Figure 3.4: (a) Caloric curve, and (b) partitioning between $x > 2\sigma$ and $x \leq 2\sigma$ in the canonical ensemble for the one-dimensional example. Data points are 0.025ϵ apart and have been joined by straight lines for clarity. Solid lines: quadrature; dashed lines: MC, adjusting d every 100 steps; dotted lines: MC adjusting d every 25 steps. Statistical errors in the MC results are too small to plot [1].

with x. Fig. 3.4 shows that the problem is most serious at intermediate temperatures where both flat and steep parts of the PES contribute significantly to the ensemble average.

The step size issue is not restricted to finite systems. Our final example is a simple cubic box with periodic boundary conditions, containing 108 atoms that interact through the Lennard-Jones potential, truncated at a radius, r_c, equal to half the box length. The total potential energy is

$$U = 4\sum_{i<j} \epsilon_{ij}[(\sigma/r_{ij})^{12} - (\sigma/r_{ij})^{6}]\Theta(r_{ij} - r_c), \tag{3.3}$$

where Θ is the step function, and $\epsilon_{ij} = \epsilon$ for all interactions except those where both i and j come from a set of four "special" atoms (labeled 1 to 4) which interact more strongly with each other. For pairs of these atoms (i.e. $1 \leq i, j \leq 4$), $\epsilon_{ij} = 5\epsilon$. The interaction energy, $U_{\rm sp}$, of the special atoms can be obtained by restricting the sum in Eq. (3.3) to terms with $1 \leq i, j \leq 4$.

At a temperature of $kT/\epsilon = 1.45$ (above the critical point of bulk Lennard-Jones), and a density of $0.2\sigma^{-3}$, the ordinary atoms form a low density fluid in which the special particles may aggregate and disperse. Since the special atoms are likely to be closer together on average, and less able to accept large trial displacements, it is appropriate to adopt separate maximum step sizes, $d_{\rm or}$ and $d_{\rm sp}$, for the ordinary and special atoms respectively. Using different fixed step sizes in this way does not violate microscopic reversibility.

Fig. 3.5 shows the canonical average $\langle U_{\rm sp} \rangle$ obtained from MC under the above conditions as a function of the number of sweeps between adjustments of the maximum step size. $d_{\rm or}$ and $d_{\rm sp}$ were adjusted separately whenever the specified number of sweeps for the relevant subset of atoms had been performed. Five runs were performed at each temperature, each commencing with $80,000$ equilibration sweeps from the final configuration of the previous run (the very first configuration being generated by random placement of all the atoms)

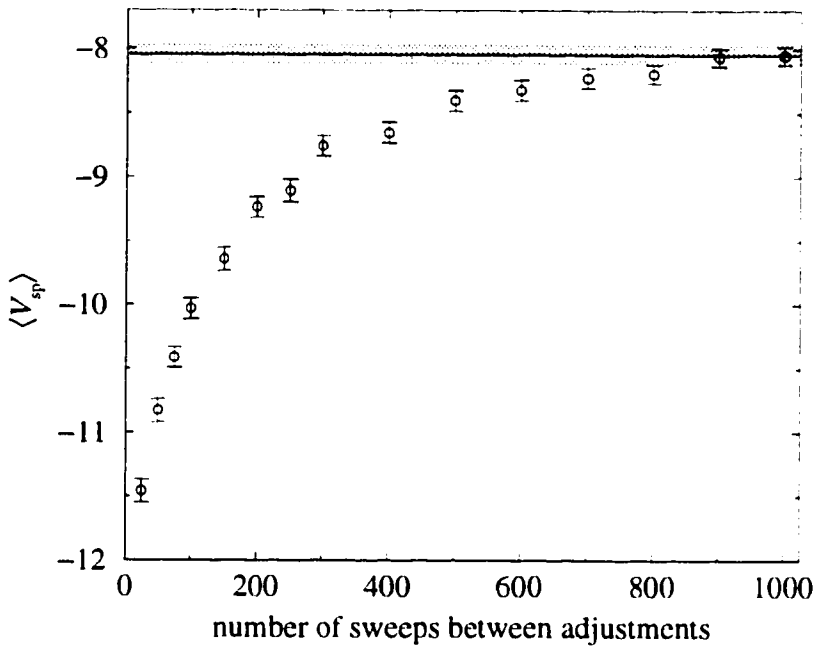

Figure 3.5: Mean interaction energy of the four "special" atoms in a supercritical fluid with periodic boundary conditions at $kT/\epsilon = 1.45$ and an overall density of $0.2\sigma^{-3}$ as a function of the number of sweeps between step size adjustments. Error bars indicate the standard error in the mean. The horizontal line and shaded area represent the result and standard error obtained with a fixed maximum step size [1].

and subsequently accumulating statistics every 16 sweeps for 4×10^6 sweeps. The data from all five runs were combined to obtain $\langle U_{sp} \rangle$, and the standard error was estimated using the blocking method [58]. The plot shows disagreement between simulations in which the maximum step sizes are adjusted and those in which they are fixed until the period between adjustment approaches about 900 sweeps. Whereas the statistical uncertainty is of the order of 1%, systematic error is about 4% when 500 sweeps elapse between adjustments and as large as 23% when the interval is 100 sweeps. Inspection of the distribution (not shown) of distances between the special atoms shows that adjusting the step size causes a disproportionately large number of samples to contain the special atoms clustered together. The potential experienced by the special atoms is most rapidly changing for such configurations, and as in the previous examples, allowing the step size to respond to the decreased acceptance ratio causes these configurations to be oversampled.

3.4 Summary

In this chapter, we have chosen simple atomic systems to demonstrate clearly the source of the systematic error that can arise from the dynamic adjustment of the maximum step size during MC simulations. However, we emphasize that any potentially inhomogeneous system could be susceptible to such error. Examples include solvated structures, polymers that can adopt compact or unfolded conformations, and any systems undergoing large fluctuations, such as near a phase change. Free energy calculations are particularly susceptible since the optimum step sizes for the initial and final states are likely to be different. Correlations between the step size and the region of configuration space may therefore occur at an intermediate stage if the step size is allowed to change, leading to systematic error even though equilibrium averages and

in the case of FTV calculations, upper and lower bounds, will seem to have converged consistently.

In summary, depending on the nature of the system and the conditions, the systematic error introduced by dynamic adjustment of the maximum step size may range from negligibly small to unacceptably large. Convergence of observables is probably only improved if the step size can adapt to different regions of configuration space. Since such correlations are the very source of the error, the purpose of such a scheme is defeated. We thus recommend that MC simulations start with a period of pre-equilibration in which the maximum step size is adjusted to achieve a target acceptance ratio. The step size should then be held fixed during a subsequent equilibration of the configuration and the production run itself. In the case of a free energy computation spanning a range of densities, an appropriate deterministic scaling of d may be used [56].

Chapter 4

REFERENCE STATES

The reference state plays a significant role in the overall computation time of an FTV calculation. As described in chapter 2, increasing the efficiency of the switching process (the number of MC sweeps needed the obtain convergence of the upper and lower bounds) will lower the computation time. However, the total computation time also depends on the amount of time taken for each MC sweep as well as the time needed to compute the free energy of the reference state. The choice of reference state can affect all three of these aspects of the calculation. If the reference state is simple enough, its free energy may be calculated analytically and therefore contribute a trivial amount to the total computation time. However, if a numerical integration is required the total computation time may be significantly increased. The amount of computation time needed per MC sweep will also be affected by implicit constraints required by the reference state. Lastly, because less work is required to switch between systems which are similar, the efficiency of the switching process can be greatly enhanced by choosing a reference state is similar to the system of interest.

In this thesis we consider the free energy of Lennard-Jones (LJ) atomic clusters. The atoms interact pair-wise through the well known interaction

$$U_{LJ}(\mathbf{r}) = 4\epsilon\left(\left(\frac{\sigma}{|\mathbf{r}|}\right)^{12} - \left(\frac{\sigma}{|\mathbf{r}|}\right)^{6}\right). \tag{4.1}$$

such that the coordinate-dependent part of the Hamiltonian for a system of N

atoms is

$$H_{LJ} = \sum_{i=1}^{N} \left(\sum_{j<i}^{N} U_{LJ}(\mathbf{r}_i - \mathbf{r}_j) \right). \tag{4.2}$$

To optimize the switching efficiency of the free energy calculations, the reference state should share similarities with the LJ cluster in the state of which the free energy is desired. The most obvious feature of a system is its physical state, i.e. its thermodynamic phase. LJ clusters can exist in both solid and liquid phases as described in chapter 1. Therefore, solid clusters should be switched to a solid-like state which has a similar lattice structure. Liquid clusters should be switched to a liquid-like state which is amorphous and has a similar density. Choosing the reference state in this way also avoids hysteresis during the switching the process, i.e., the reverse switching process for a solid cluster should end with a configuration that looks like a solid cluster. Said another way, the reverse switching should not lead to the system having difficulty in finding its way to typical equilibrated states characteristic of the fully coupled analog.

Because the free energy of the reference state should be easily calculated, a convenient reference state is a system of ideal gas particles. This state is easily achieved by multiplying U_{LJ} by a coefficient, $c(\lambda)$, which changes from $c(0) = 1$ to $c(1) = 0$ where λ is a measure of the progress of the switching process (see chapter 2). Reference states, however, encompass more than just the explicit interactions between atoms. The volume in which the atoms move is part of the reference state as well as the number of coordinates which are allowed to change during the simulation. In this chapter, we propose several different reference states for LJ clusters in which these latter two features are adjusted to maximize the overlap in configuration space with either solid or liquid clusters while the explicit interactions, those of ideal gas particles, remain the same. The advantages and disadvantages for each reference state

are then discussed.

4.1 Liquid Cluster

We first consider clusters which are in a liquid state. If the reference state is only defined by zero interaction between particles, then as $c(\lambda)$ approaches zero, the atoms could move infinitely far away from each other. An easy remedy is to constrain the atoms to some fixed volume. In our work, this is achieved by imposing a hard wall spherical container in which any MC move which results an atom exceeding a distance R_c from the center of the container is rejected. Because the cluster has an overall translation, it will interact with the wall such that the free energy calculated will be the free energy of a cluster interacting with a wall rather than just of the cluster. This translation needs to be separated out. The most obvious method is to center the container on the center of mass of the cluster instead of at the origin. This type of reference has been proposed and the partition function derived by by Lee, Barker and Abraham (LBA) [26]. We review it in some detail in the next section. We also present an alternative method of removing translation by centering the container on one atom. These two methods will be shown to give the same results under appropriate and well defined conditions.

4.1.1 Center of Mass Coordinates

More than two decades ago, LBA demonstrated how to separate out translation of the center mass of a cluster in a free energy calculation. We review it here to as a foundation on which we will later build other reference states. The first

step is rewriting the coordinates:

$$\begin{aligned} x_1 &= -x_2' - x_3' \cdots - x_N' + X_{cm}, \quad x_2 = x_2' + X_{cm}, \ldots \quad x_N = x_N' + X_{cm} \\ y_1 &= -y_2' - y_3' \cdots - y_N' + Y_{cm}, \quad y_2 = y_2' + Y_{cm}, \ldots \quad y_N = y_N' + Y_{cm} \\ z_1 &= -z_2' - z_3' \cdots - z_N' + Z_{cm}, \quad z_2 = z_2' + Z_{cm}, \ldots \quad z_N = z_N' + Z_{cm} \end{aligned} \tag{4.3}$$

The Hamiltonian in these new coordinates is

$$H_{LJ_{cm}} = \sum_{i=2}^{N} \left(\sum_{j<i}^{N} U_{LJ}(\mathbf{r}_i' - \mathbf{r}_j') + U_{LJ}(\mathbf{r}_i' + \mathbf{r}_{sum}') \right) \tag{4.4}$$

$$\mathbf{r}_{sum} = \sum_{i=2}^{N} \mathbf{r}_i' \tag{4.5}$$

The partition function rewritten in these new coordinates is

$$\begin{aligned} Q_{3N} &= \int \cdots \int \exp(-H_{LJ}(x_1, y_1, z_1 \ldots x_N, y_N, z_N)/kT) dx_1, dy_1, dz_1 \ldots dx_N dy_N dz_N \\ &= \int dX_{cm} \int dY_{cm} \int dZ_{cm}\, Q_{cm} \end{aligned} \tag{4.6}$$

$$Q_{cm} = N^3 \int_{\widetilde{C}(R_c)} \cdots \int \exp(-H_{LJ_{cm}}(x_2', y_2', z_2' \ldots x_N', y_N', z_N')/kT) \tag{4.7}$$

$$dx_2', dy_2', dz_2' \ldots dx_N' dy_N' dz_N'$$

The N^3 term is from the Jacobian required for the change of variables. Its derivation is outlined in appendix B. The container is imposed by adding a constraint, $\widetilde{C}(R_c)$, to the integration. In the notation of LBA

$$\widetilde{C}(R_c); \qquad \begin{cases} |\mathbf{r}_i'| \leq R_c, \\ |\mathbf{r}_{sum}| \leq R_c \end{cases} \tag{4.8}$$

We will refer to this set of coordinates as CM.

A MC simulation in CM coordinates can done by at least two different algorithms. In the one used by LBA, the atoms move just as before but the container is centered at the center of mass as in the following pseudo-code:

Algorithm 1 (for CM coordinates)

1: calculate center of mass, $\mathbf{cm} = \sum_i^N \mathbf{r}_i$

2: move the ath atom, $\mathbf{r}_a = \mathbf{r}_a + \mathbf{step}$

3: recalculate center of mass , $\mathbf{cm} = \mathbf{cm} + \mathbf{step}/N$

4: test all atoms, is $|\mathbf{r}_i - \mathbf{cm}| \leq R_c$

5: if no, reject MC move

6: if yes, calculate the difference in energy

$\Delta U = \sum_{i=1,i\neq a}^N U_{LJ}(\mathbf{r}_a - \mathbf{r}_i) - U_{LJ}(\mathbf{r}_{a_{old}} - \mathbf{r}_i)$

7: if $\Delta U < 0$ or $\exp(-\Delta U/kT) >$ random number, accept move

8: go to step 2

Imposing the constraint in equation 4.8 requires an additional N distance calculations because every time the center of mass moves, all the atoms must be rechecked to be certain that none have exceeded the bounds. Alternatively, the center of mass could be kept constant at the origin by shifting all the atoms by step$/N$ at every MC move. Step 4 would still be necessary but would become $|\mathbf{r}_i| \leq R_c$. The extra step of shifting all the atoms adds $3N$ more unnecessary operations. A different approach is to move the atoms according to redefined coordinates in 4.3. In this algorithm, only $N-1$ atoms are explicitly moved by MC steps. The first one moves in response to the other atoms, $\mathbf{r}_N = -\mathbf{r}_{sum}$ as in the following code:

Algorithm 2 (for CM coordinates)

1: begin with the center of mass at the origin

2: move the ath atom, but not the first one, $\mathbf{r}_a = \mathbf{r}_a + \mathbf{step}$

3: adjust $\mathbf{r}_{sum}$, $\mathbf{r}_{sum} = \mathbf{r}_{sum} + \mathbf{step}$

4: test atom a and $\mathbf{r}_{sum}$, is $|\mathbf{r}_a| \leq R_c$ and is $|\mathbf{r}_{sum}| \leq R_c$

5: if no, reject MC move

6: if yes, calculate the difference in energy

$\Delta U = \sum_{i=2,i\neq a}^N U_{LJ}(\mathbf{r}_a - \mathbf{r}_i) + \sum_{i=2}^N U_{LJ}(\mathbf{r}_i + \mathbf{r}_{sum}) -$

$$\sum_{i=2,i\neq a}^{N}(U_{LJ}(\mathbf{r}_{a_{old}}-\mathbf{r}_i)-U_{LJ}(\mathbf{r}_i+\mathbf{r}_{sum_{old}}))-U_{LJ}(\mathbf{r}_{a_{old}}+\mathbf{r}_{sum_{old}})$$

7: if $\Delta U < 0$ or $\exp(-\Delta U/kT) >$ random number, accept move

8: go to step 2.

It is not immediately clear which of these algorithms would be faster. On one hand, the number of distance calculations in step 4) is reduced by $N-2$. However, step 5) is more complicated than in the first algorithm. Instead of $2(N-1)$ calls to U_{LJ}, a computationally expensive function, it requires $2(2N-3)$. As a practical example we tested both algorithms in an equilibrium simulation of LJ_{55} at T=$0.37\epsilon/k$. In this case, algorithm 1 was found to be 1.5 times faster than algorithm 2 making a good case for the former.

Though the two simulations do not have the same number of coordinates, the free energy differences resulting from them are equivalent. The translational degrees of freedom are sampled in the first code and not the second but the free energy due to translation is irrelevant because it is the same for both the cluster and the ideal gas.

$$\begin{aligned}\Delta A &= A_{gas}-A_{cluster}\\ &= -kT\ln\left(\frac{Q_{gas}}{Q_{cluster}}\right)\\ &= -kT\ln\left(\frac{\int dX_{cm}\int dY_{cm}\int dZ_{cm}\,Q_{cm_{gas}}}{\int dX_{cm}\int dY_{cm}\int dZ_{cm}\,Q_{cm}}\right)\\ &= -kT\ln\left(\frac{Q_{cm_{gas}}}{Q_{cm}}\right)\end{aligned} \tag{4.9}$$

where $Q_{cm_{gas}}$ is the partition function of the ideal gas reference state in CM coordinates. The motion of the center of mass drops out of the calculation. The FTV method only measures the ratio of the two partition functions. In this case, they are only different in the integral over $\mathbf{r}'_2, \mathbf{r}'_3, \ldots \mathbf{r}'_N$ coordinates. Similarly, the integral over the velocity coordinates are the same for both states. These other coordinates only affect the absolute free energy and they are added in later. This point about only the relevant coordinates contributing to the free

energy will come up again as other reference states are introduced.

In order to determine the absolute free energy of the cluster, the partition function for the reference state must be known. With the ideal gas interaction, the partition function depends only on the volume of the container and the set of relevant coordinates. If the additional constraint in equation 4.8 of $\mathbf{r}_{sum} \leq R_c$ was not imposed, then the partition function would just be $(\frac{4}{3}\pi R_c)^{N-1}$. The first atom, $\mathbf{r}_N = -\mathbf{r}_{sum}$ could move far from the origin but not infinitely far. Its maximum distance would be $(N-1)R_c$. Because the second constraint is necessary, the integral is not easily separable. LBA evaluated the partition function, $Q_{cm_{gas}}$, by representing the constraints as Fourier transforms. The derivation is complicated and can be found in appendix A. The result is

$$Q_{cm_{gas}} = N^3 \left(\frac{4}{3}\pi R_c^3\right)^{N-1} \frac{2}{\pi} 3^{N-1} \int_0^\infty \left(\frac{\sin x - x\cos x}{x^2}\right)^N x^2 dx \qquad (4.10)$$

Though the integral must computed numerically, even for $N = 55$, it can be computed to great precision in a trivial amount of time.

The size of R_c is an important parameter. It should be large enough to accommodate all the internal motions of the cluster yet small enough to keep the computation efficient. At low temperatures atoms do not evaporate from the cluster and the integrand of Q_{cm} goes to zero at large distances. Beyond that point, Q_{cm} is independent of R_c. The appropriate cutoff can be estimated by determining where density profiles of the cluster go to zero. Examples of such profiles are shown in section 4.1.3. The smaller R_c can be made without affecting the internal motions of the cluster, the closer the densities of the reference and original states will be and the more the configurations of each state will overlap.

4.1.2 One Atom Center Coordinates

Using the CM reference state in the previous section as a model, we propose a second method of separating out translation of the cluster. The CM reference state allows efficient switching because the volume of the container can be small enough such that densities of the two states are close. However, the computational time needed per MC sweep maybe unnecessarily high because all the atoms are affected whenever one atom moves. Also, the derivation of the partition function for the CM reference state is complicated (see appendix A). Though, LBA have derived the result for a spherical container which constrains all the atoms, if the container is modified, a new result for the reference free energy is not easily obtained. This point will be illustrated section 4.2.1. For these reasons, we explore a different reference state we will call one atom center.

Instead of centering the container at the center of mass of the cluster, it is centered on the first atom. As in section 4.1.1, we begin by rewriting the coordinates:

$$\begin{aligned} x_1 &= X_{ac}, \quad & x_2 &= x_2' + X_{ac}, \quad & \ldots x_N &= x_N' + X_{ac} \\ y_1 &= Y_{ac}, \quad & y_2 &= y_2' + Y_{ac}, \quad & \ldots y_N &= y_N' + Y_{ac} \\ z_1 &= Z_{ac}, \quad & z_2 &= z_2' + Z_{ac}, \quad & \ldots z_N &= z_N' + Z_{ac} \end{aligned} \tag{4.11}$$

In this set of coordinates, X_{ac}, Y_{ac}, Z_{ac} refer to the one atom which acts as the center. These coordinates are much simpler than the center of mass ones because they do not depend on each other. The Hamiltonian in these coordinates is

$$H_{LJ_{ac}} = \sum_{i=2}^{N} \left(\sum_{j<i}^{N} U_{LJ}(\mathbf{r}_i' - \mathbf{r}_j') + U_{LJ}(\mathbf{r}_i') \right) \tag{4.12}$$

and the partition function becomes

$$Q_{3N} = \int dX_{ac} \int dY_{ac} \int dZ_{ac}\, Q_{ac} \tag{4.13}$$

$$Q_{ac} = \int \cdots \int \exp(-H_{LJ_{ac}}(x'_2, y'_2, z'_2 \ldots x'_N, y'_N, z'_N)/kT) \tag{4.14}$$
$$dx'_2, dy'_2, dz'_2 \ldots dx'_N dy'_N dz'_N$$

Q_{ac} differs from Q_{cm} in two ways. It does not include the N^3 term because the Jacobian is equal to one (see appendix B). Also, instead of using a constraint as in equation 4.8, the constraining volume is imposed by the limiting the integration such that each atom is allowed a volume of $\frac{4}{3}\pi R_c$. This set of coordinates will be referred to as AC.

Like CM, the AC simulation can be performed by either allowing all N atoms to move and re-centering the container every time the first atom moves, or by just not moving the first atom. For the same reasons explained in the previous section, these two AC simulations will give the same result but in this case, clearly, the latter method requires less computation. For every MC sweep, only N-1 atoms move and each step requires only one distance calculation for the volume constraint. If all the atoms are allowed to move, every time the first atom moved, all the atoms would need to be checked for the volume constraint. The algorithm for AC simulation is

Algorithm 3 (for AC coordinates)

1: begin with first atom at the origin

2: move ath atom, but not the first one, $\mathbf{r}_a = \mathbf{r}_a + \text{step}$

3: test only atom a, is $|\mathbf{r}_a| \leq R_c$

4: if no, reject MC move

5: if yes, calculate the difference in energy

$\Delta U = \sum_{i=2, i\neq a}^{N} U_{LJ}(\mathbf{r}_a - \mathbf{r}_i) + U_{LJ}(\mathbf{r}_a) - \sum_{i=2, i\neq a}^{N} (U_{LJ}(\mathbf{r}_{a_{old}} - \mathbf{r}_i) - U_{LJ}(\mathbf{r}_{a_{old}})$

6: if $\Delta U < 0$ or $\exp(-\Delta U/kT) >$ random number, accept move

7: go to step 2

This algorithm not only has fewer steps than algorithms 1 and 2, the number of operations per step is also smaller. In section 4.1.3 we give a more quantitative comparison between the amount of computer time each algorithm uses.

In addition to the decrease in computations, the partition function for the AC reference state is quite simple because the atoms are truly non-interacting. The partition function is just the product of the volumes each atom moves in or

$$Q_{ac_{gas}} = \left(\frac{4}{3}\pi R_c^3\right)^{N-1} \tag{4.15}$$

These simplifications make the AC simulations more convenient and faster per MC sweep but not more efficient. The efficiency decreases because the volume needed to allow all the internal motions of the liquid cluster is greater than the one needed in CM. In a liquid cluster in which atoms can move throughout the cluster, the Nth atom will not necessarily be in the center of the cluster. It can also be at the edge such that the radius of the constraining volume needs to be larger than just radius of the cluster. In fact, the radius may need to be set at double the radius of the cluster to allow for all the instances of the Nth atom located at an edge. As in CM, the density for an equilibrated cluster will show how large the volume must be. Using a such a large volume will decrease the efficiency of the switching process because the reference state density will be an order of magnitude lower than the density of the cluster and the overlap of configurations will be smaller.

4.1.3 Comparison of Center of Mass and One Atom Center

We have shown that the free energy of an atomic cluster can be calculated by using two different coordinate systems to define the reference state. In this section, we will first demonstrate that $Q_{ac} = Q_{cm}$ so that the free energy calculated either way will give the same result. Secondly, we will compare the

overall computation time of both types of calculations to determine if one algorithm is substantially superior.

Equivalent Results

We cannot show analytically that the partition functions of a Lennard-Jones cluster calculated in either coordinates are equivalent because we do not know either partition function analytically. If we did, we would not need a free energy difference calculation. However, if we use a simpler system which has a known partition function, we can prove that the two sets of coordinate give the same result under well defined conditions.

Two particles interacting through a harmonic potential in one dimension is our model system. The partition function in Cartesian coordinates is

$$Q_{harm} = \iint \exp(-(x_1 - x_2)^2/kT) dx_1 dx_2$$

In center of mass coordinates,

$$\begin{aligned} x_1 &= x_2' + X_{cm} \\ x_2 &= -x_2' + X_{cm} \end{aligned} \qquad \frac{\partial(x_1, x_2)}{\partial(X_{cm}, x_2')} = 2$$

$$\begin{aligned} Q_{harm} &= \int dX_{cm} \int 2\exp(-(2x_2')^2/kT) dx_2' \\ &= \int dX_{cm}\ Q_{cm_{harm}} \end{aligned} \tag{4.16}$$

In one atom center coordinates

$$\begin{aligned} x_1 &= X_{ac} \\ x_2 &= x_2' + X_{ac} \end{aligned} \qquad \frac{\partial(x_1, x_2)}{\partial(X_{ac}, x_2')} = 1$$

$$\begin{aligned} Q_{harm} &= \int dX_{ac} \int \exp(-(x_2')^2/kT) dx_2' \\ &= \int dX_{ac}\ Q_{ac_{harm}} \end{aligned} \tag{4.17}$$

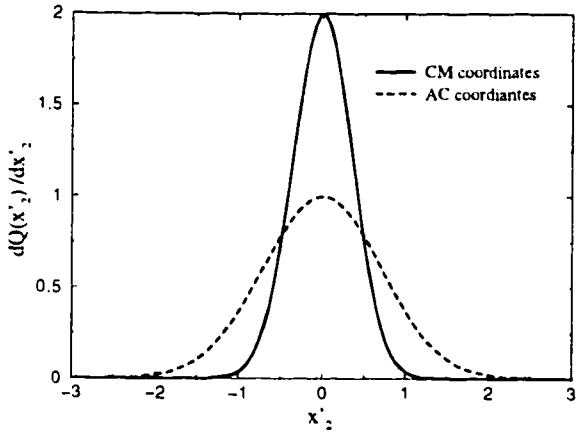

Figure 4.1: Integrands from equations 4.18 and 4.19 as a function of x_2', with $kT = 1$

If the limits of integration are $[-a, a]$,

$$Q_{cm_{harm}} = \sqrt{\frac{\pi}{kT}}\,\mathrm{erf}(2a\sqrt{kT}) \tag{4.18}$$

$$Q_{ac_{harm}} = \sqrt{\frac{\pi}{kT}}\,\mathrm{erf}(a\sqrt{kT}) \tag{4.19}$$

As $a \to \infty$ the error functions approach one and the answers are identical. In figure 4.1, the integrands of equations 4.16 and 4.17 are plotted as functions of x_2' with $kT = 1$. By $|x_2'| > 3$, where both integrands have gone to zero, the areas under these curves are the same. As long as the limits of integration are taken far enough from the origin where the partition functions goes to zero, $Q_{cm_{harm}} = Q_{ac_{harm}}$. The limits for $Q_{ac_{harm}}$ must be doubled because the distance to the origin is the entire separation between the atoms as opposed to half of the distance as with $Q_{cm_{harm}}$. This distance issue is analogous to the cluster, in which the origin can be at an outer edge of cluster.

The analysis above demonstrates that free energy for the two different coordinate systems are equal as long as integration limits can be taken large enough such that they no longer affect the partition function. In the case of

clusters, this requirement means that the cluster remains intact, that atoms do not evaporate. Otherwise, the atoms will fill whatever container they are in. Though this analytical analysis cannot be done on atomic clusters, it can be shown numerically that the results are same. We show this with a four atom cluster, LJ_4. Figure 4.2 shows the minimum energy tetrahedral structure of LJ_4 in both sets of coordinates. The shaded region surrounding the clusters depict the different constraining volumes needed for each coordinate system.

For this comparison, we chose a temperature low enough, that the tetrahedral structure is preserved, T=0.05 ϵ/k. The density profiles for each system are shown in figure 4.3. Data for both profiles were computed from the same simulation in which no volume constraint was imposed. After an equilibration period of 20,000 sweeps, the distances of each atom to both the center of mass and to the first atom were added to a histogram after every sweep for another 10^7 sweeps. Because the distance from the first atom will always be zero it was not included. At such a low temperature, LJ_4 is small and remains a solid with the atoms nearly equidistant from each other so the density profile for each set of coordinates is just one peak. The atoms are closer to the origin in CM than they are in AC as can be seen in figure 4.2. Another noticeable difference between the two peaks is that the AC peak is much broader. This difference occurs because AC allows for translation of the center of mass and the extra motion becomes incorporated into the density peak. The profiles in figure 4.3 show what the appropriate container size should be. For CM, $R_c = 0.825\sigma$ and $R_c = 1.6\sigma$ for AC.

Free energy difference calculations were performed using the CM reference state and algorithm 2 and also using the AC reference state with algorithm 3. Both calculations began with the minimum energy configuration which was equilibrated for 20,000 sweeps and maximum step size adjusted every 50 sweeps during just the first 2,000 sweeps. After the equilibration period, the

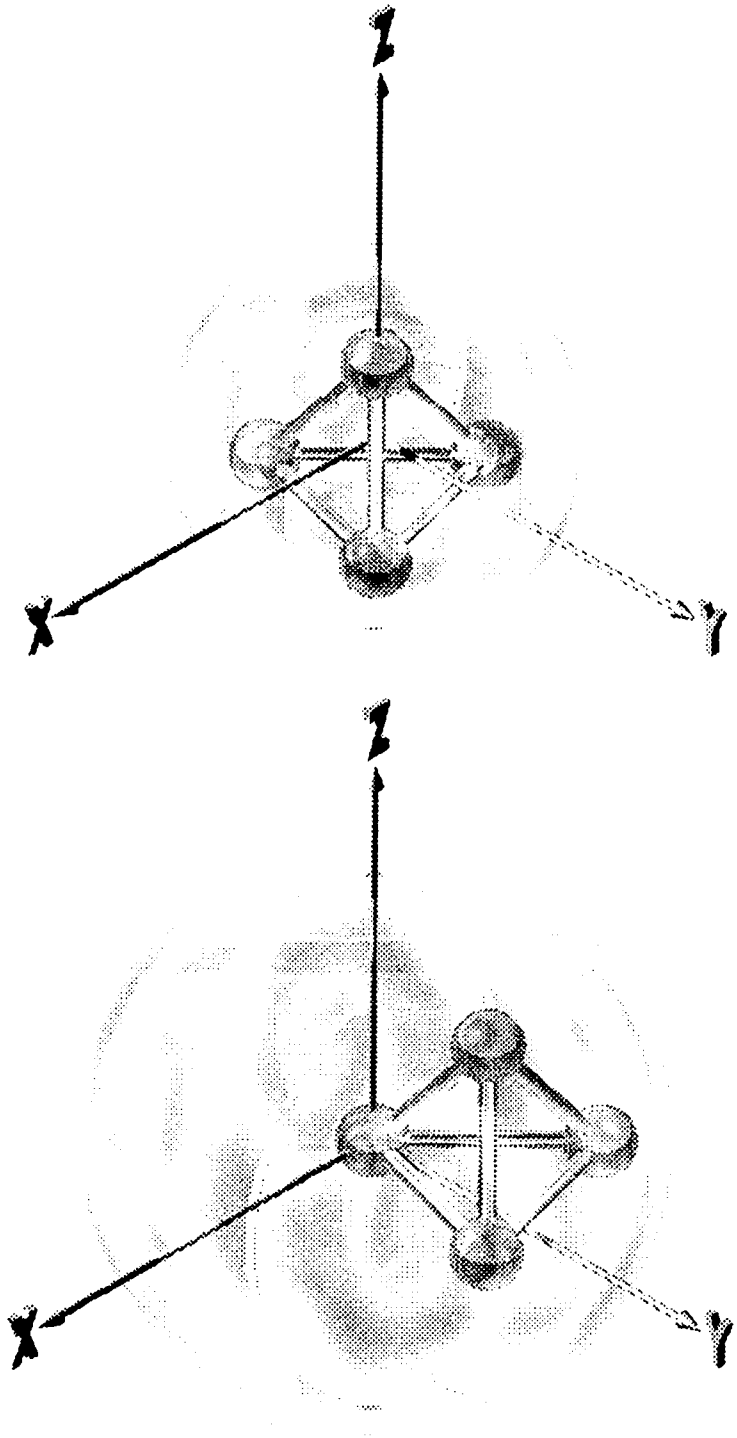

Figure 4.2: LJ_4 in CM coordinates (upper) and AC coordinates (lower). The spheres illustrate how are constraining volumes centered.

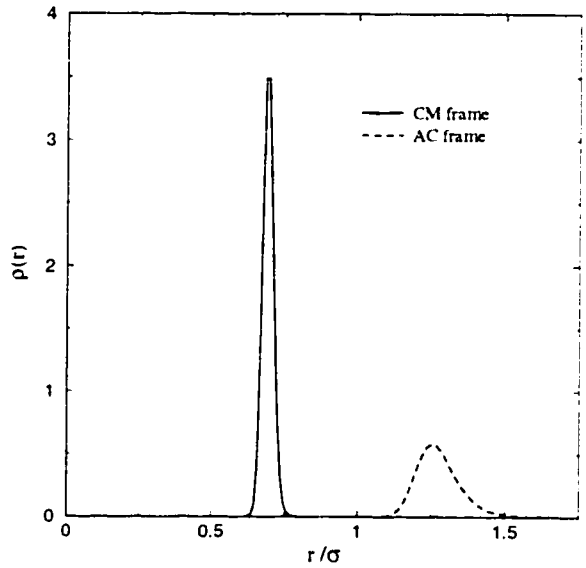

Figure 4.3: Density profiles for LJ_4 at T=0.05ϵ/k. The solid line represents $\rho(r)$ where r is the distance to the center of mass. The dashed line represents $\rho(r)$ where r is the distance to the first atom.

maximum step size is changed to an intermediate value between the appropriate sizes for the initial and final states, 0.10σ for the CM calculation and 0.50σ for AC. The interactions were switched off with the function $c(\lambda) = (1 - \lambda)^3$ over 1×10^7 sweeps. Fifty replicas were used for both the forward and reverse simulations for each calculation. The free energies of the CM and AC reference states are $-kT \ln Q_{cm_{gas}}$ and $-kT \ln Q_{ac_{gas}}$ respectively. The results shown in table 4.1 are the same to within the total error (see equation 2.15).

Computation Time

Since we have established that both methods give the same result for the free energy of the cluster, we are free to choose the method that requires the least amount of computation time. In order to compare the two methods, we use a more relevant system, LJ_{55}, at a temperature high enough that it remains

Table 4.1: Free energy of LJ_4 calculated using the two different reference states. All free energies are given in units of ϵ. The error is computed from equation 2.15.

coordinates	A_{ref}	ΔA	error	$A_{ref} - \Delta A$
center of mass	-0.27986	5.23885	0.00025	-5.51870
one atom center	-0.42636	5.09246	0.00031	-5.51891

in the liquid state, T=0.37ϵ/k. For this system at this temperature, there is a small chance that an atom can evaporate from the cluster which makes choosing the size of the constraining volume more complicated than for LJ_4. Evaporation events would alter the density profiles because one or more atoms could move infinitely far from the cluster. Such events can be prevented by rejecting MC moves that result in any atom being a distance greater than $bond_{max}$ to its nearest neighboring atom. Defining $bond_{max}$ is be problematic because any definition would seem arbitrary. A reasonable estimate can be made by computing the atom-atom radial distribution function as shown in figure 4.4. After 500,000 equilibration sweeps, all the atom-atom distances were added to a histogram for an additional 10^7 sweeps. A constraining volume of 4.5σ relative to the center of mass was imposed to prevent atoms moving infinitely far away. The constraining volume is much larger than the cluster and should not interfere with the cluster's internal motions. The first peak corresponds to nearest neighbor interactions after which there is a clear minimum before the next nearest neighbor peak. We chose $bond_{max}$ to be the distance which corresponds to the minimum between these two peaks. In figure 4.4, $bond_{max} = 1.55\sigma$. A second simulation was then run in which no constraining volume was imposed but any MC move that resulted in any atom being further away than $bond_{max}$ from its nearest neighbor was rejected. The equilibration and data collection

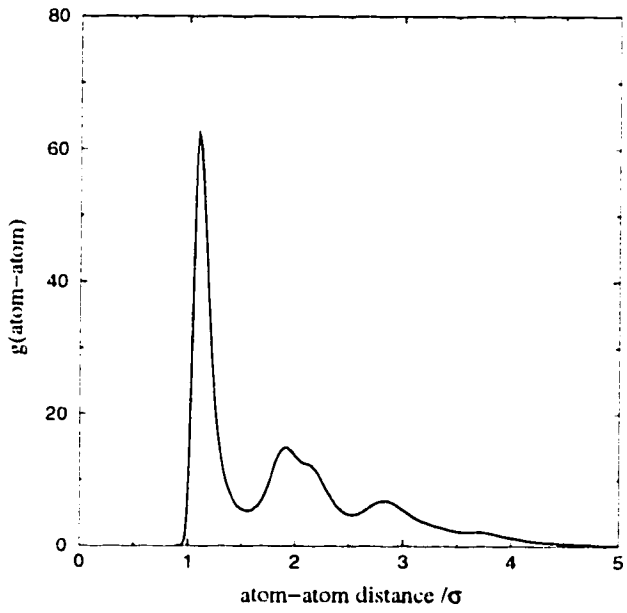

Figure 4.4: Atom-atom radial distribution function for LJ_{55} at T=0.37ϵ/k.

periods were the same as for the first simulation. Density profiles were computed as was described for LJ_4 in both simulations and are shown in figure 4.5. Though the peaks in the simulation without checking for evaporation are slightly shorter, choosing the appropriate value for R_c will be the same for either simulation. This feature will not necessarily hold at higher temperatures so it is worth checking for evaporation even though the simulation takes about 3.3 times longer.

Like the density profiles for LJ_4, the CM and AC profiles look quite different. In figure 4.5a, a peak occurs at zero because LJ_{55} almost always has an atom at its center. The next two peaks show that two shells of atoms surround the center atom. Figure 4.5b has no peak until about 1.0σ because the origin is centered on an atom which means no other atom can get closer than one atom diameter away. Clearly, a larger sphere is needed for the AC coordinates, $R_c = 5.0\sigma$ versus $R_c = 3.25\sigma$ for the CM coordinates. This increase in volume

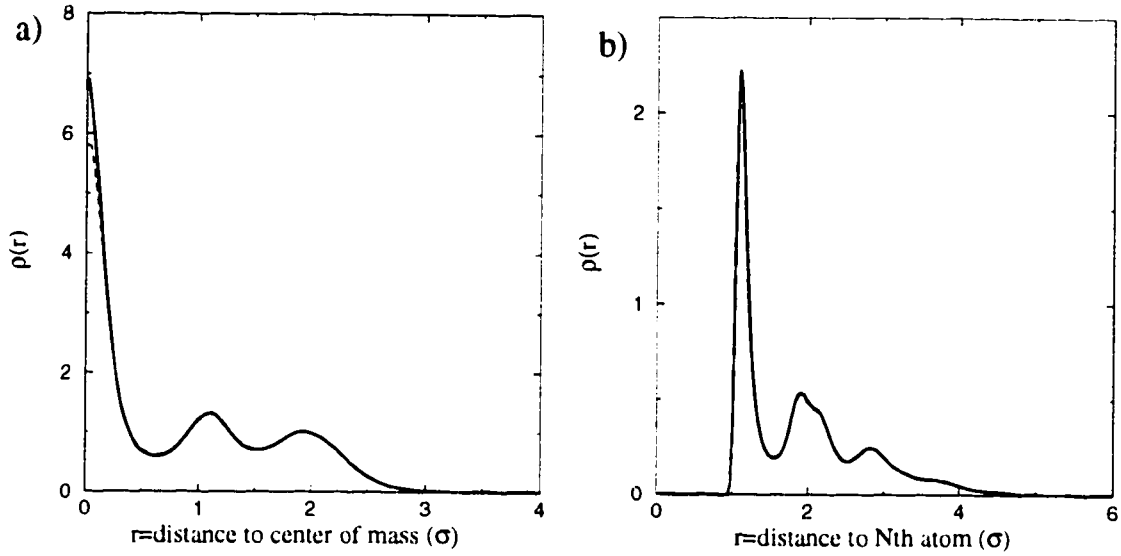

Figure 4.5: Density profiles for LJ_{55} at T=0.37ϵ/k. The solid lines are from simulations with the $bond_{max} = 1.55\sigma$ restriction and no volume constraint. The dashed lines are from simulations with no bond restriction but constrained by a volume of radius $R_c = 4.5\sigma$.

should affect the efficiency of the calculation but it may be overshadowed by the smaller amount of computation per MC sweep.

Free energy calculations were performed in a similar manner as for LJ_4. The initial configurations for the forward direction were taken every 500,000 sweeps from post-equilibration part of simulation in which $bond_{max}$ was determined. The initial configurations for the reverse direction were equilibrated from a randomly selected configuration for 10,000 sweeps. A total of 20 replicas were used for each switching direction. The constant step size used during the switching process for the CM and AC calculations were 0.25σ and 0.75σ respectively. To be certain that only intact clusters were being used, any final configuration for the reverse calculation in which any atoms were detached by the criteria described above was not used. Because the initial configurations used for the forward directions came from a simulation with this constraint,

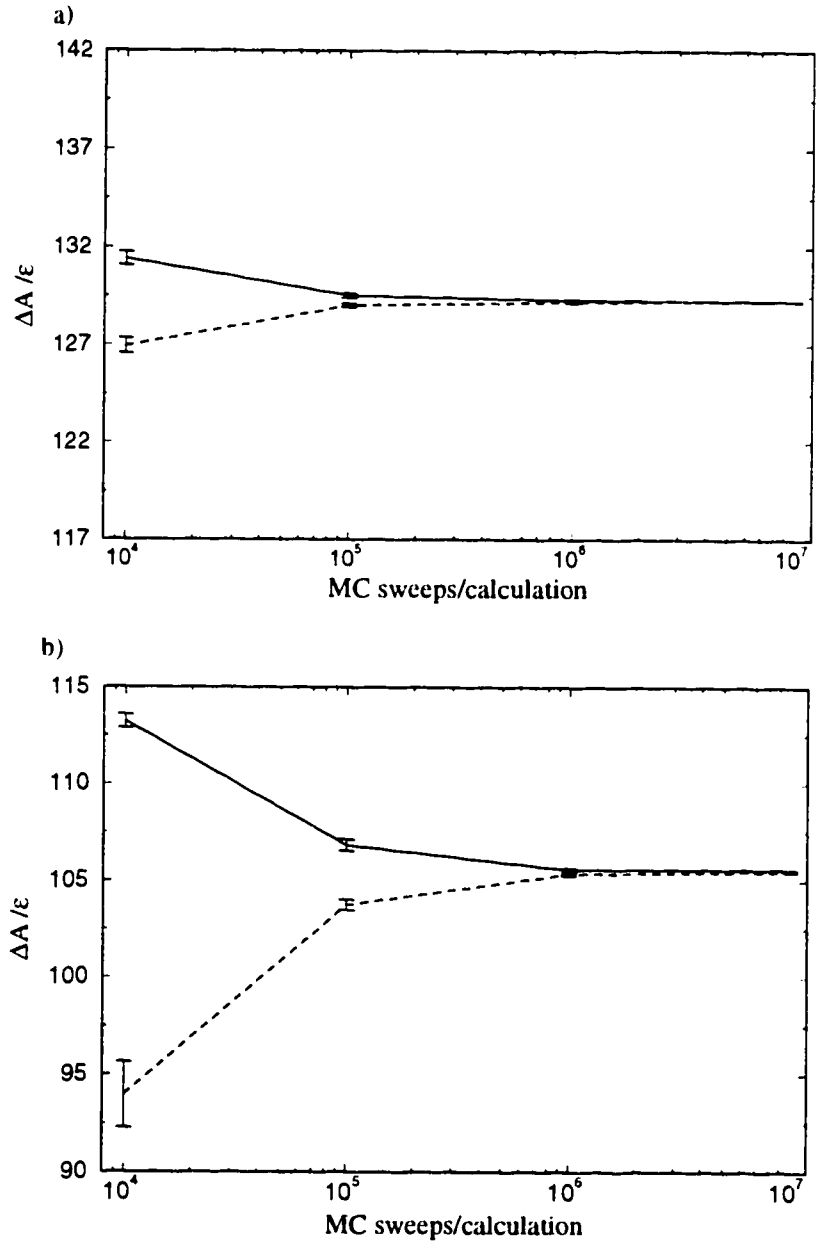

Figure 4.6: Convergence of upper and lower bounds on the free energy difference for LJ_{55} at T=0.37ϵ/k in a) CM coordinates and b) AC coordinates. The ranges on the x and y-axes are the same for both a) and b). The solid lines connect each calculation of $W(LJ_{55} \rightarrow ref)$ as the dashed lines do for $-W(ref \rightarrow LJ_{55})$.

they were known to be intact.

To determine which calculation is more efficient, we plotted in figure 4.6 the work as a function of MC sweeps calculated for the forward direction, the upper bound to ΔA, and the negative of the work in the reverse direction, the lower bound, for both AC and CM simulations. The ranges of the x and y-axes of both figures are set equal to show how much more quickly the center of mass method converges. The error in the center of mass method at one million sweeps is 0.070ϵ. In order to achieve that same error with the one atom center method, the calculation would require more than ten million sweeps. The AC calculation is 1.2 times faster per MC sweep than the CM calculation but this gain in speed is not nearly enough to make up for the loss of efficiency in the AC calculation. Though the CM reference state is clearly the optimal choice for the liquid cluster, we will show in the next section that when these reference states are extended to solid clusters, the one atom center coordinates have a distinct advantage.

4.2 Solid Clusters

Efficient free energy computations for solid clusters require a different type of reference state than that used for liquid clusters. One that possesses some qualities of a solid cluster is optimal. Free energy changes have been calculated for bulk solids by using an ideal crystal, also known as the Einstein crystal, as a reference state [59]. The Einstein crystal is a set of independent harmonic oscillators whose centers are spread out on a lattice. Usually, the lattice is chosen to coincide with the minimum energy structure of the initial system. In this work we use a similar type of reference state in which atoms interact with a lattice site but in place of a harmonic interaction, the atoms act as ideal gas particles. Small hard wall containers are centered at each lattice site to

keep the ideal gas particles close to their respective centers. As with the large container used for liquid clusters, the small containers need to be large enough to accommodate atomic vibrations but they should not be so large that particle exchange occurs.

Applying this type of constraint to a cluster which is free not only to translate but to rotate as well is problematic. Even after translation is removed, rotation of the cluster will cause difficulties. Like the liquid cluster translating and interacting with the walls, when the cluster in this environment rotates, the atoms will interact with the walls of the small containers. Such interactions will contribute to the free energy. These problems do not arise in bulk free energy calculations and so they have not been addressed before now. Calvo and Labastie [60] presented one method for eliminating rotation from a cluster in an equilibrium MC simulation. All the atoms are moved in one MC step and the angular momentum is taken to be $L_{tot} = m(\sum_i^N \mathbf{r}_i \times \delta\mathbf{r}_i)$. All of the steps, $\delta\mathbf{r}_i$, are then adjusted to make the total angular momentum zero. We have tried this method and found that unless the step sizes are quite small, the acceptance rates are so low that free energy calculations do not converge. A simpler strategy, like those used for handling translation in the liquid clusters, is to eliminate the rotational coordinates from the simulation. In the next two sections, we present two different methods for doing so.

4.2.1 Center of Mass, Non-rotating Coordinates

The first set of coordinates have translation separated out just as the CM coordinates. Separating out the rotational coordinates requires more sophisticated methods. Just as in the CM coordinates described in section 4.1.1, the center of mass defines the origin of the coordinates. To remove rotation, three other coordinates are used to define the x, y, and z axes. Figure 4.7 shows an example with LJ_4 in which the center of mass is at the origin. The x and y coordinates

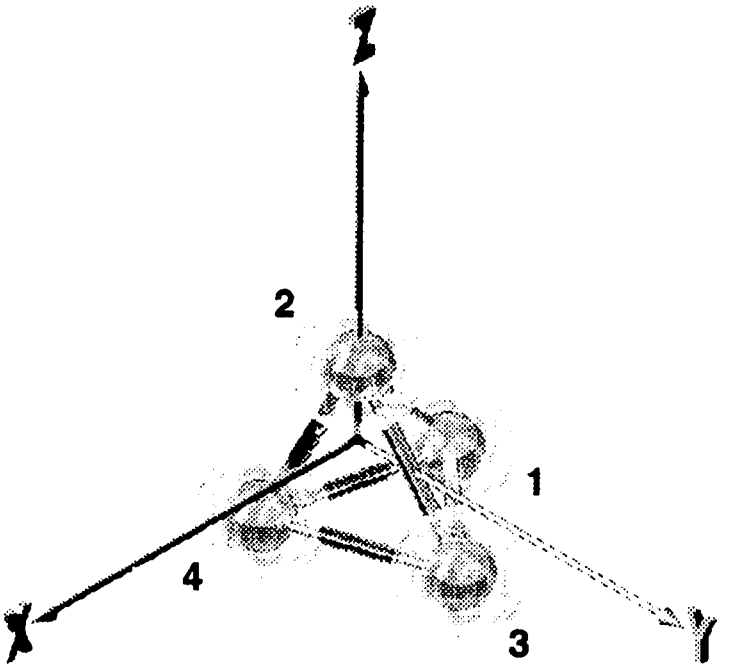

Figure 4.7: LJ_4 in CMNR coordinates. The small spheres surrounding each atom show how each constraining volume imposed. The center of mass remains at the origin. Atom 2 is restricted the z-axis and atom 3 is restricted to the y, z plane. All other atoms are free to move in all three coordinates.

of atom 2 are at zero such that the atom defines the z-axis. The x coordinate of atom 3 is zero and defines the yz-plane. These three coordinates can be defined by any two atoms as long as they are not collinear with the center of mass. In terms of the new coordinates,

$$
\begin{aligned}
x_1 &= -z'_2 D_{13} - y'_3 D_{12} - z'_3 D_{13} \cdots - x'_N D_{11} - y'_N D_{12} - z'_N D_{13} + X_{cm} \\
x_2 &= z'_2 D_{13} + X_{cm}, \qquad x_3 = y'_3 D_{12} + z'_3 D_{13} + X_{cm}, \\
x_4 &= x'_4 D_{11} + y'_4 D_{12} + z'_4 D_{13} + X_{cm} \quad \ldots x_N = x'_N D_{11} + y'_N D_{12} + z'_N D_{13} + X_{cm} \\
y_1 &= -z'_2 D_{23} - y'_3 D_{22} - z'_3 D_{23} \cdots - x'_N D_{21} - y'_N D_{22} - z'_N D_{23} + Y_{cm} \\
y_2 &= z'_2 D_{23} + Y_{cm}, \qquad y_3 = y'_3 D_{22} + z'_3 D_{23} + Y_{cm}, \\
y_4 &= x'_4 D_{21} + y'_4 D_{22} + z'_4 D_{23} + Y_{cm} \quad \ldots y_N = x'_N D_{21} + y'_N D_{22} + z'_N D_{23} + Y_{cm} \\
z_1 &= -z'_2 D_{33} - y'_3 D_{32} - z'_3 D_{33} \cdots - x'_N D_{31} - y'_N D_{32} - z'_N D_{33} + Z_{cm} \\
z_2 &= z'_2 D_{33} + Z_{cm}, \qquad z_3 = y'_3 D_{32} + z'_3 D_{33} + Z_{cm}, \\
z_4 &= x'_4 D_{31} + y'_4 D_{32} + z'_4 D_{33} + Z_{cm} \quad \ldots z_N = x'_N D_{31} + y'_N D_{32} + z'_N D_{33} + Z_{cm}
\end{aligned}
\tag{4.20}
$$

The terms D_{ij} are the elements of the rotation matrix

$$
\begin{pmatrix}
\cos\phi\cos\psi - \sin\phi\cos\theta\sin\psi & -\cos\phi\sin\psi - \sin\phi\cos\theta\cos\psi & \sin\phi\sin\theta \\
\sin\phi\cos\psi + \cos\phi\cos\theta\sin\psi & -\sin\phi\sin\psi + \cos\phi\cos\theta\cos\psi & -\cos\phi\sin\theta \\
\sin\theta\sin\psi & \sin\theta\cos\psi & \cos\theta
\end{pmatrix}
\tag{4.21}
$$

in which θ, ϕ, ψ are Euler angles.

Rewriting the partition function in these coordinates requires a more complicated Jacobian than the one used CM or AC coordinates though its value turns out to be surprisingly simple: $N^3 \sin(\theta) y'_3 z'^2_2$. The derivation is in appendix C. The new partition function is

$$
Q_{3N} = \int dX_{cm} \int dY_{cm} \int dZ_{cm} \int_{-\pi}^{\pi} d\psi \int_{-\pi}^{\pi} d\phi \int_{0}^{\pi} \sin(\theta) d\theta \; Q_{cmnr} \tag{4.22}
$$

$$Q_{cmnr} = N^3 \int_{\tilde{C}(R_c)} \cdots \int y_3' z_2'^2 \exp(-H_{LJ_{cmnr}}(z_2', y_3', z_3' \ldots x_N', y_N', z_N')/kT)$$
$$dz_2', dy_3', dz_3' \ldots dx_N' dy_N' dz_N' \tag{4.23}$$

The small containers are imposed in this case by a slightly different constraint than equation 4.8:

$$\tilde{C}(R_c): \quad \begin{cases} |\mathbf{r}_i' - \mathbf{site}_i| \leq R_c \\ |\mathbf{r}_{sum} + \mathbf{site}_1| \leq R_c \end{cases} \tag{4.24}$$

The lattice positions are represented by $\mathbf{site}_i$. They are chosen as the positions of the atoms in the minimum energy configuration. This set of coordinates will be referred to as CMNR.

In section 4.1.1, we presented two different algorithms for simulating atoms in center of mass coordinates and showed that allowing all the atoms to move and re-centering the container (algorithm 2) was significantly faster than only moving the $3N-3$ center of mass coordinates with the first atom moving only in response to the others (algorithm 1). Ideally, we would like to use an algorithm for CMNR that is similar to algorithm 2 because it is faster. The analogous algorithm would allow all the atoms to move and then the lattice on which the small spheres are centered would not only be re-centered to the new center of mass, it would also have to be rotated. This extra step would require determining the three Euler angles, making up the rotation matrix and multiplying each of the N lattice positions by the rotation matrix. These extra computations surely would obscure the gain in speed. For this reason, the following algorithm we use for CMNR is similar to algorithm 2 instead of algorithm 1.

Algorithm 4 (for CMNR coordinates)

1: begin with the center of mass at the origin,
the x and y coordinates of atom 2 at zero
and the x coordinate of atom 3 at zero

2: move the ath atom, but not the first one, $\mathbf{r}_a = \mathbf{r}_a + \mathbf{step}$

if atom = 2, $\mathrm{step}_x = 0$ and $\mathrm{step}_y = 0$

if atom = 3, $\mathrm{step}_x = 0$

3: adjust $\mathbf{r}_{sum}$, $\mathbf{r}_{sum} = \mathbf{r}_{sum} + \mathbf{step}$

4: test atom a and $\mathbf{r}_{sum}$, is $|\mathbf{r}_a - \mathbf{site}_a| \leq R_c$ and is $|\mathbf{r}_{sum} + \mathbf{site}_N| \leq R_c$

5: if no, reject MC move

6: if yes, calculate the difference in energy

$$\Delta U = \sum_{i=2,i\neq a}^{N} U_{LJ}(\mathbf{r}_a - \mathbf{r}_i) + \sum_{i=2}^{N} U_{LJ}(\mathbf{r}_i + \mathbf{r}_{sum}) - \sum_{i=2,i\neq a}^{N} (U_{LJ}(\mathbf{r}_{a_{old}} - \mathbf{r}_i) - U_{LJ}(\mathbf{r}_i + \mathbf{r}_{sum_{old}})) - U_{LJ}(\mathbf{r}_{a_{old}} + \mathbf{r}_{sum_{old}})$$

7: if $\frac{y_3 z_2^2}{y_{3_{old}} z_{2_{old}}^2} \exp(-\Delta U/kT) >$ random number, accept move

8: go to step 2

The extra term in step 5) comes from the extra term in partition function. Unless atom 2 or 3 moves, it is equal to one. Though this method does not extinguish overall cluster motion altogether it reduces it quite dramatically. In the next section we demonstrate this reduction. The method works best when the cluster is solid and has only low amplitude internal motions.

A significant disadvantage of this reference state is that its partition function is not easily calculated. Though the atoms are not interacting with one another through a potential, they are not independent due to the constraint in equation 4.24 so the integral is not separable. The methods used by LBA to determine the partition function for the CM ideal gas in one large volume will not work in this case. The differences between that system and this one are that the atoms each move in their own containers which are each at different locations and the extra $y_3' z_2'^2$ term in the integral. We are left to determine the integral numerically using Monte Carlo techniques. This computation is possible because even for $N = 55$ the atoms are restricted to small volumes.

4.2.2 *One Atom Center, Non-rotating Coordinates*

The CMNR reference state has several weaknesses. Its partition function can only be calculated numerically and it requires additional computation because at every MC step, two atoms move thereby doubling the number of operations. A similar reference state to the one in AC coordinates can alleviate these problems. In this state, translation is removed by keeping the origin at the first atom. Rotation is removed by the same method described in the previous section. The z-axis is defined by atom 2 whose x and y coordinates remain at zero. The yz-plane is defined by atom 3 which has its x coordinate at zero. Figure 4.8 illustrates this new set of coordinates for LJ_4. Rewriting the coordinates

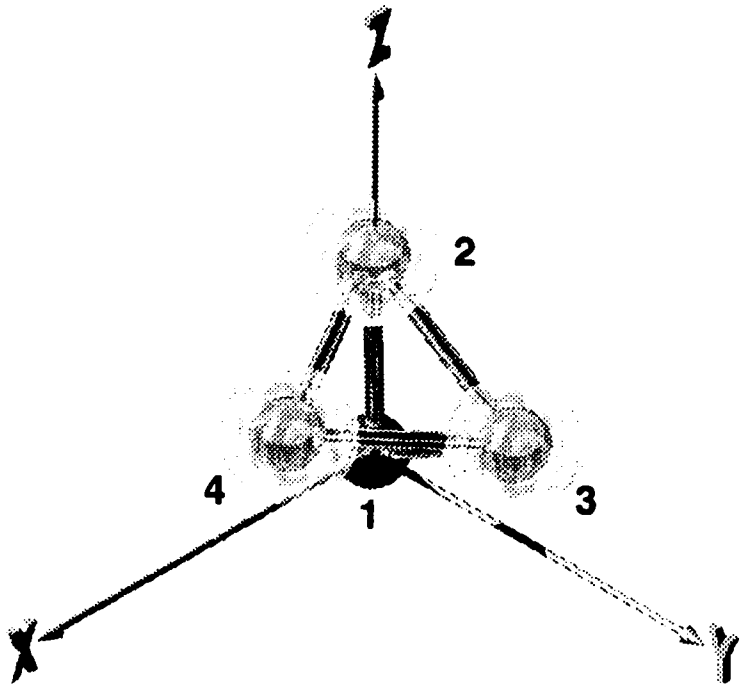

Figure 4.8: LJ_4 in ACNR coordinates. The small spheres surrounding each atom show how each constraining volume imposed. Atom 1 remains at the origin. Atom 2 is restricted the z-axis and atom 3 is restricted to the y, z plane. All other atoms are free to move in all three coordinates.

results in

$$
\begin{aligned}
x_1 &= X_{ac} & x_2 &= z_2' D_{13} + X_{ac}, & x_3 &= y_3' D_{12} + z_3' D_{13} + X_{ac}, \\
x_4 &= x_4' D_{11} + y_4' D_{12} + z_4' D_{13} + X_{ac} & \ldots x_N &= x_N' D_{11} + y_N' D_{12} + z_N' D_{13} + X_{ac} \\
y_1 &= Y_{ac} & y_2 &= z_2' D_{23} + Y_{ac}, & y_3 &= y_3' D_{22} + z_3' D_{23} + Y_{ac}, \\
y_4 &= x_4' D_{21} + y_4' D_{22} + z_4' D_{23} + Y_{ac} & \ldots y_N &= x_N' D_{21} + y_N' D_{22} + z_N' D_{23} + Y_{ac} \\
z_1 &= Z_{ac} & z_2 &= z_2' D_{33} + Z_{ac}, & z_3 &= y_3' D_{32} + z_3' D_{33} + Z_{ac}, \\
z_4 &= x_4' D_{31} + y_4' D_{32} + z_4' D_{33} + Z_{ac} & \ldots z_N &= x_N' D_{31} + y_N' D_{32} + z_N' D_{33} + Z_{ac}
\end{aligned}
\tag{4.25}
$$

The terms D_{ij} are the elements of the rotation matrix from 4.21. The Jacobian in this case, worked out in appendix C to be $\sin(\theta) y_{N-2}' z_{N-1}'^2$, is strikingly similar to the one needed in the CMNR coordinates except for the N^3 which is exactly the difference between the Jacobians of the CM and AC coordinate systems used for the liquid cluster. The resulting partition function is

$$
Q_{3N} = \int dX_{ac} \int dY_{ac} \int dZ_{ac} \int_{-\pi}^{\pi} d\psi \int_{-\pi}^{\pi} d\phi \int_{0}^{\pi} \sin(\theta) d\theta \; Q_{acnr} \tag{4.26}
$$

$$
Q_{acnr} = \int \cdots \int z_2'^2 y_3' exp(-H_{LJ_{acnr}}(z_2', y_3', z_3', \ldots, x_N', y_N', z_N')/kT) \tag{4.27}
$$

$$
dz_2', dy_3', dz_3', \ldots, dx_N', dy_N', dz_N'
$$

This set of coordinates will be referred to as ACNR.

The algorithm for these coordinates shares steps with both Algorithms 3 and 5.

Algorithm 5 (for ACNR coordinates)

1: begin with first atom at the origin,
the x and y coordinates of atom 2 at zero and
the x coordinate of atom 3 at zero

2: move the ath atom, but not the first one, $\mathbf{r}_a = \mathbf{r}_a + \text{step}$
if atom = 2, $\text{step}_x = 0$ and $\text{step}_y = 0$
if atom = 3, $\text{step}_x = 0$

3: test only atom a, is $|\mathbf{r}_a - \text{site}_a| \leq R_c$

4: if no, reject MC move

5: if yes, calculate the difference in energy

$\Delta U = \sum_{i=2,i\neq a}^{N} U_{LJ}(\mathbf{r}_a - \mathbf{r}_i) + U_{LJ}(\mathbf{r}_a) - \sum_{i=2,i\neq a}^{N}(U_{LJ}(\mathbf{r}_{a_{old}} - \mathbf{r}_i) - U_{LJ}(\mathbf{r}_{a_{old}})$

6: if $\frac{y_3 z_2^2}{y_{3_{old}} z_{2_{old}}^2} \exp(-\Delta U/kT) >$ random number, accept move

7: go to step 2

As with algorithm 4, this one is also quite successful at reducing overall rotation of the cluster. A specific example will be shown in section 4.2.3. This algorithm differs with the previous one in that only one atom moves per MC step. This means that U_{LJ} is only called $N-2$ times versus $2(N-2)$ times. Also, at every MC step, only one atom has to be checked to see if it left the sphere instead of all N atoms. The computation time for this algorithm should be much shorter than algorithm 4. A more quantitative analysis is given in the next section.

The partition function for this reference state is easily calculated because, unlike the CMNR reference state, the ideal gas atoms are all independent of each other.

$$Q_{gas_{acnr}} = \int z_2'^2 dz_2' \iint y_3' dy_3' dz_3' \iiint dx_4' dy_4' dz_4' \cdots \iiint dx_N' dy_N' dz_N' \qquad (4.28)$$

Unlike the liquid reference states, however, the integration must be with respect to the lattice sites instead of the origin. For $\mathbf{r}_i; i = 4 \ldots N$, that change of coordinates is trivial and a further transformation to spherical coordinates yields the expected result: $\left(\frac{4}{3}\pi R_c^3\right)^{N-3}$. For the second atom, the integration is only over two coordinates.

$$u = y_3' - y_{3_{site}}; \qquad v = z_3' - z_{3_{site}}$$

$$du = dy_3'; \qquad dv = dz_3'$$

$$\iint y_3' dy_3' dz_3' = \iint u + y_{3_{site}} du dv$$

Transforming u and v in polar coordinates yields

$$\int_0^{2\pi}\int_0^{R_c} r^2\cos\theta + r y_{3_{site}} = \pi R_c^2 y_{3_{site}} \tag{4.29}$$

The last part of the integration is straight forward because it is only over one coordinate. Instead of transforming the coordinates the limits of integration are adjusted.

$$\int_{z_{2_{site}}-R_c}^{z_{3_{site}}+R_c} z_2'^2 dz_2' = 2z_{2_{site}}^2 R_c + \frac{2}{3}R_c^3$$

and bringing the parts together

$$Q_{gas_{acnr}} = \left(\frac{4}{3}\pi R_c^3\right)^{N-3}\left(\frac{2}{3}R_c^3 + 2R_c z_{2_{site}}^2\right)\pi R_c^2 y_{3_{site}} \tag{4.30}$$

A clear advantage of using this reference state over the CMNR state is that unlike $Q_{gas_{cmnr}}$, this partition function is not only known exactly, it is quite easy to derive.

4.2.3 Comparison of Center of Mass, non-rotating and One Atom Center, non-rotating

As for liquid clusters, we have presented two methods for the calculating free energy of solid clusters. In this section, we show that the two methods yield equivalent results. We also give an analysis of which method achieves those results with the least amount of total computation time.

Equivalent Results

We can show the results are the same numerically, again using the LJ_4 cluster in figures 4.7 and 4.8. We use the same temperature, 0.05 ϵ/k, as in section 4.1.3 which is low enough that the cluster maintains its tetrahedral structure. Now, instead of showing that the cluster density goes to zero at some distance

from the origin, we need to show that the probability of an atom moving some distance from its lattice site goes to zero. Two separate simulations were run with no volume constraints, one in CMNR coordinates and one in ACNR coordinates. After 20,000 equilibration sweeps, the distances of each atom to its lattice site are added to a histogram every sweep for another 10^6 sweeps. Because the first atom in the ACNR simulation does not move its distance is not added. The atom-site radial distribution function, in figure 4.2.3, shows that the distribution decreases to zero over a short radius indicating that the mechanism for removing rotation is indeed working for both sets of coordinates. The atoms do not move far from their lattice sites. The ACNR peak is broader than its CMNR counter part. This difference occurs because although the the ACNR cluster does not translate or rotate about the origin, it does have a small amount of translation and rotation about the center of mass. From these histograms, appropriate values of R_c for the CMNR and ACNR simulations are 0.20σ and 0.28σ respectively.

Using these values for R_c, free energy difference calculations were performed using algorithm 4 and the CMNR reference state and using algorithm 5 and the ACNR reference state. The maximum step size adjustment period was 2000 sweeps and equilibration period was 20,000 sweeps. After the equilibration period, the maximum step size was changed to 0.075σ for both types of simulations and U_{LJ} was switched off with the function $c(\lambda) = (1-\lambda)^3$ over 10^7 sweeps. Fifty replicas were run for both the forward and reverse simulations for each calculation. The free energy of the CMNR reference state is $-kT \ln Q_{cmnr_{gas}}$ and $-kT \ln Q_{acnr_{gas}}$ for the ACNR reference state. $Q_{cmnr_{gas}}$ was obtained numerically using Monte Carlo integration from a code found in appendix D. The ensemble average and standard error in the mean of $Q_{cmnr_{gas}}$ were determined from ten separate calculations consisting 10^7 points. The propagated error in $A_{ref} = -kT \ln Q_{acnr_{gas}}$ was of the order of 10^{-6} and not in-

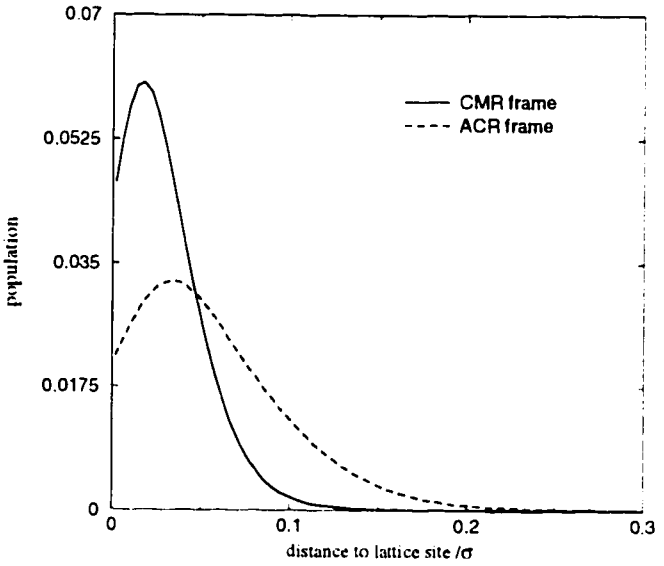

Figure 4.9: Population of atoms from their lattice sites for LJ_4 at T=0.05ϵ/kin center of mass and one atom center non-rotating coordinates.

cluded in the total error of the free energy of the cluster. The results are shown in table 4.2. The free energies are the same within the total error.

Computation Time

As we showed with the liquid cluster methods, we have established that the two solid cluster methods yield the same result. Now, we establish which method is

Table 4.2: Free energy of LJ_4 calculated using the two different non-rotating reference states. All free energies are given in units of ϵ. The error is computed from equation 2.15.

coordinates	A_{ref}	ΔA	error	$A_{ref} - \Delta A$
center of mass	0.210446	5.47613	0.00034	-5.26568
one atom center	0.207212	5.47267	0.00017	-5.26546

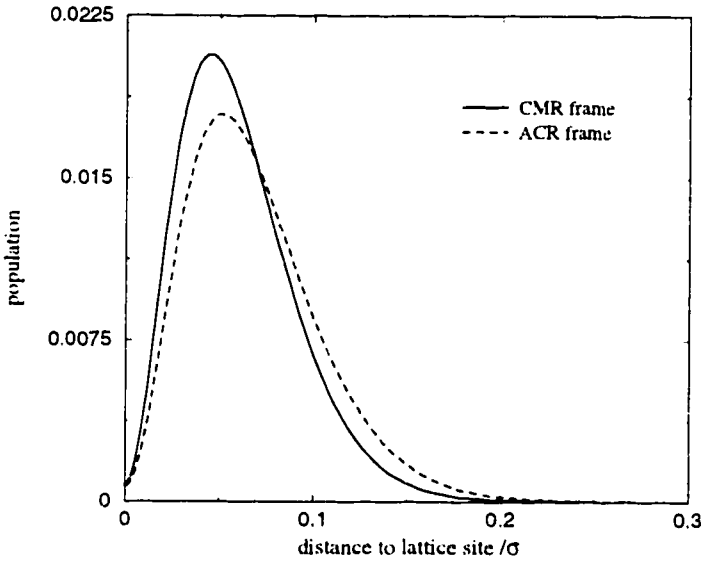

Figure 4.10: Atom-site radial distribution functions for LJ_{55} at T=0.083ϵ/kin center of mass non-rotating and one atom center non-rotating coordinates.

preferable for computing free energies by determining, for the same amount of total error, which has the lowest total computational time. As in section 4.1.3, we use LJ_{55} to make the comparison but this time the temperature used is lowered to one at which the cluster is a solid, $T = 0.083\epsilon/k$. First the appropriate size of the containers must be established. Atom-site radial distribution functions were computed as described for the LJ_4 case. Because at this temperature atoms do not evaporate, no special steps are required when collecting data for the histograms. Figure 4.10 shows the distribution functions from simulations with equilibration periods of 500,000 sweeps and data collection periods of 10^7 sweeps. The radius of the spheres need for the ACNR simulation, 0.250σ, is only slightly larger than the one needed for the CMNR simulation, 0.225σ. Given this small difference in volumes, the convergence of the upper and lower bounds of ACNR would be expected to be only slightly worse than CMNR.

Free energy difference calculations were then performed using these values

for R_c according to description for LJ_4. The initial configurations for the forward direction were taken every 500,000 sweeps from post-equilibration part of simulations in which R_c was determined. The initial configurations for the reverse direction were equilibrated from a randomly selected configuration for 10,000 sweeps. A total of 20 replicas were used for each switching direction. The constant step size used during the switching process for the CMNR and ACNR calculations were 0.05σ and 0.075σ respectively. Unlike the the liquid cluster, no extra effort is required to be certain that all the clusters are intact. The upper and lower bounds to ΔA as a function of MC sweeps are plotted in figure 4.11. The plots defy the prediction that the CMNR reference state would produce better convergence because it requires smaller spheres. In fact, when the number of MC sweeps is small, the convergence for ACNR coordinates is better. However, when 10^6 sweeps are used per calculation, the total error for both calculations is comparable. This unexpected reversal in converge times can be explained by the unusual steps required in algorithm 4, namely that for every atom moved, an additional atom has to be moved in response. Such coordination results in a decreased acceptance ratio which affects how much phase space can be explored.

Slower convergence is not the only feature which makes the CMNR calculation more computationally taxing. As explained in 4.2.2, the computation time per MC sweep is greater for CMNR simulations. For LJ_{55} at $T = 0.083\epsilon/k$, a CMNR free energy difference calculation takes 2.2 times longer than ACNR with the same number of MC sweeps. The most significant liability of CMNR however is that the free energy of the reference state must be computed numerically. Unlike the one dimensional integral in equation 4.10, the integral needed to compute $Q_{cmnr_{gas}}$ has $3N - 6$ dimensions which for $N = 55$ is a large calculation. We computed $-kT \ln Q_{cmnr_{gas}}$ in the same manner as for LJ_4. To achieve a statistical error on the order of 10^{-4}, ten calculations of 10^7 points

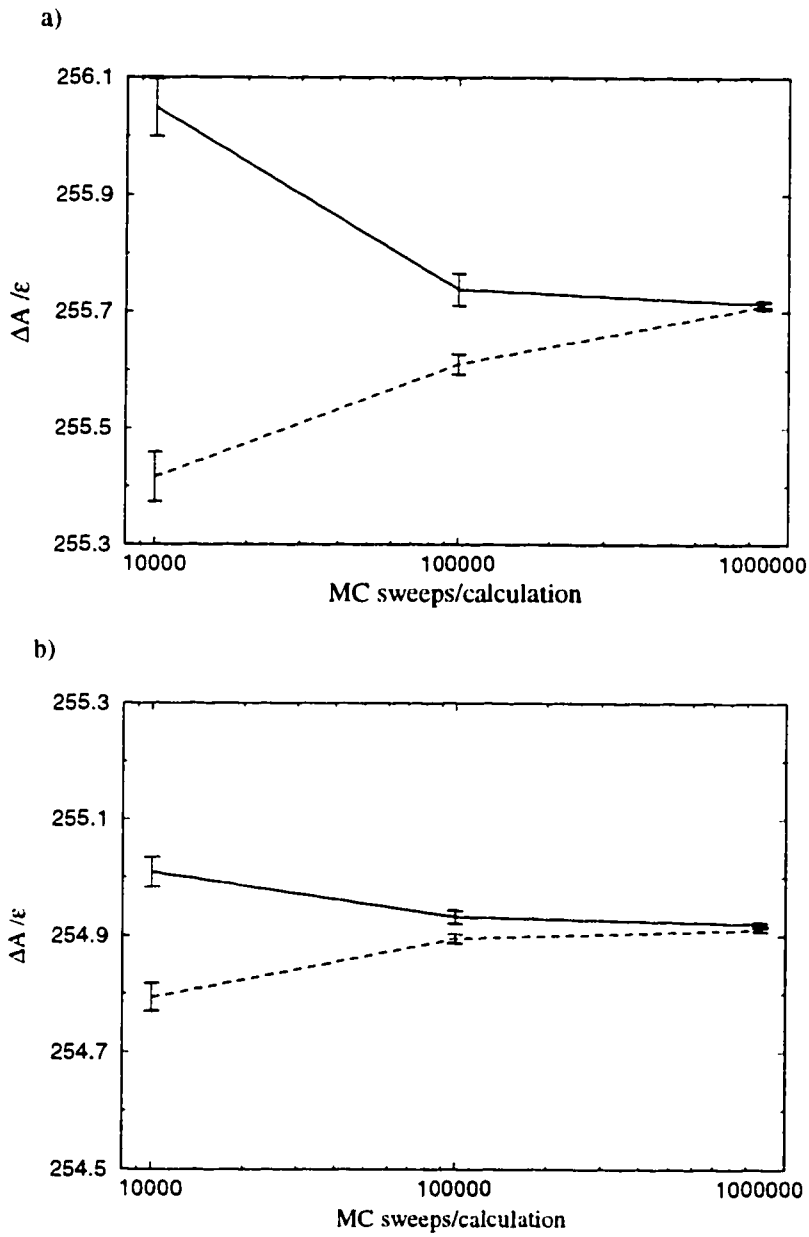

Figure 4.11: Convergence of upper and lower bounds on the free energy difference for LJ_{55} at T=0.083ϵ/kin a) CM coordinates and b) AC coordinates. The ranges on x and y axes are the same for both a) and b). The solid lines connect each calculation of $W(LJ_{55} \rightarrow ref)$ as the dashed lines do for $-W(ref \rightarrow LJ_{55})$.

were run which consumed over three hours of computer time.

4.3 *Determining Absolute Free Energies for Solid and Liquid Clusters*

We have presented two different coordinate systems for calculating the partition function of liquid clusters and have demonstrated that the result does not depend on which coordinate system is used. Likewise, the two different coordinate systems presented for calculating the solid cluster partition function also give equivalent results. In this section, we will show that for a system like LJ_4, which is small enough that at low temperatures its free energy can computed by either the solid or liquid methods, all four coordinate systems result in the same value for the free energy. We also show what factors need to be added to each partition function to determine the absolute free energy.

The partition functions presented so far only account for the configuration part of phase space and do not include the momenta of the atoms. The solid cluster partition function, because the cluster did not rotate and because no atom exchanges were permitted, also excluded a large amount of phase space. First we show what factors need to be added to the solid cluster partition function to make it equivalent to the liquid cluster. Equation 4.6 is only different from 4.22 by

$$\int_{-\pi}^{\pi} d\psi \int_{-\pi}^{\pi} d\phi \int_{0}^{\pi} \sin(\theta) = 8\pi^2$$

The same is true of equations 4.13 and 4.26. This term accounts for the rotation that was removed from the calculation. However, if the cluster has discrete symmetry, the amount of phase space attributed to rotation will be over counted. The appropriate symmetry number is based on the lattice sites or the minimum energy conformer of the cluster. The under counting due to lack atom exchanges must be corrected by a factor of $N!$. The factor needed to make the

Table 4.3: Absolute free energy of LJ_4 calculated with each reference state. All free energies are given in units of ϵ. The error is computed from equation 2.15.

coordinates	$A_{cluster}$	error[a]
center of mass	-5.51882	0.00027
one atom center	-5.51892	0.00058
center of mass NR	-5.51878	0.00034
one atom center NR	-5.51856	0.00017

partition functions calculated from using CMNR and ACNR coordinates equal to those calculated from using CM and AC coordinates respectively is

$$8\pi^2\, N!/\sigma_r$$

where σ_r is the rotational symmetry number.

We can easily show this fact to be true for the case of LJ_4 where we already calculated the partition functions using both solid and liquid types of reference states though the temperature was low enough that the cluster remained solid. Because the cluster has a tetrahedral structure, the rotational symmetry number is 12. Table 4.3 shows that solid and liquid reference states give the same results for Q_{cm} and Q_{ac} to within the total error. This consistency confirms the correctness of the statistical and combinatorial factors.

The contribution to the partition function from the momenta of the atoms must also be added. That integral is easily solved because the momenta are independent

$$\int_{-\infty}^{\infty}\cdots\int_{-\infty}^{\infty}\exp\left(-\left(\frac{\mathbf{p}_1^2}{2m}+\ldots\frac{\mathbf{p}_N^2}{2m}\right)/kT\right)d\mathbf{p}_1\ldots d\mathbf{p}_N=\left(\sqrt{2\pi mkT/h^2}\right)^{3N}$$

in which Planck's constant is added in just make the classical partition function

equal to the quantum one. The final result is

$$Q_{total} = \int dX_{cm} \int dY_{cm} \int dZ_{cm}\, Q_{cm} \left(\sqrt{2\pi mkT/h^2}\right)^{3N} \tag{4.31}$$

If we are interested in only the partition function of the non-translating cluster, we can divide Q_{total} by the partition function for translation of the whole cluster

$$\begin{aligned} Q_{non-trans} &= \frac{\int dX_{cm} \int dY_{cm} \int dZ_{cm}\, Q_{cm} \left(\sqrt{2\pi mkT/h^2}\right)^{3N}}{\int dX_{cm} \int dY_{cm} \int dZ_{cm} \left(\sqrt{2\pi NmkT/h^2}\right)^{3}} \\ &= Q_{cm} \left(\sqrt{2\pi mkT/h^2}\right)^{3N-3} N^{-3/2} \end{aligned} \tag{4.32}$$

The $\int dX_{cm} \int dY_{cm} \int dZ_{cm}$ conveniently drop out leaving only Q_{cm} and the momentum term. As we have already shown, Q_{cm} can be calculated using any of the reference states and coordinate systems described in this chapter which means $Q_{non-trans}$ can also be calculated by any of these methods. Therefore, we can select the most efficient and least computationally intensive method. For liquid clusters, the optimal method is the center of mass coordinates constrained by one large sphere. For solid clusters, the one atom center non-rotating coordinates with many small containers performs the best.

Chapter 5

FREE ENERGY OF SOLID AND LIQUID LJ_{55} CLUSTERS

Though the reference states described in chapter 4 used in conjunction with the FTV method can be applied to any atomic cluster, and with some modification, molecular clusters, we chose a well-studied cluster, LJ_{55} , to test our methods. As noted in chapter 4, LJ_{55} is an atomic cluster composed of 55 atoms which interact via the Lennard-Jones potential (see equation 4.1). The ϵ and σ parameters can be set to make the potential mimic the interaction between noble gas atoms. For the sake of generality, we use Lennard-Jones units. Namely, energy is expressed a multiple of ϵ, distance as a multiple of σ and temperature is in units of ϵ/k where k is Boltzman's constant. In this chapter, we first review early computational studies which established melting and freezing of LJ_{55} clusters as well as indicated a third state, surface-melted clusters. Previous attempts to compute the free energy of LJ_{55} are also described. Our estimates of the cluster's free energy for a wide range of temperatures are then presented and compared to prior results.

5.1 Previous studies of LJ_{55}

An important fact regarding LJ_{55} is that the lowest potential energy structure is not the lowest energy ordering of bulk Lennard-Jones atoms, face-centered cubic (fcc). Spherical fcc, or cuboctahedral, packing was found to mechanically unstable by Burton [61] such that the clusters distort into more compact structures with lower energy. Hoare and Pal [62] showed that these low en-

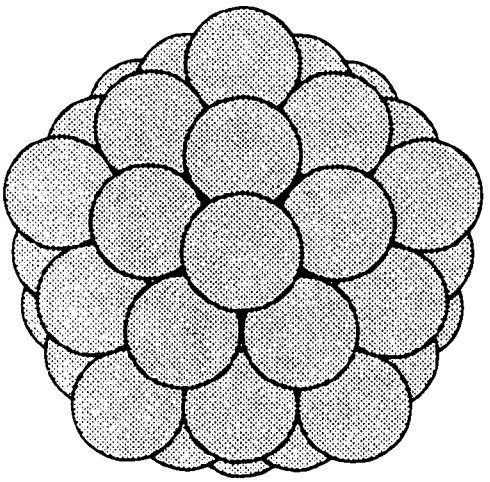

Figure 5.1: Mackay icosahedron for 55 atoms.

ergy structures are icosahedral. Such structures had already been predicted by Mackay [63] who suggested a family of icosahedral structures as a dense, non-crystallographic packing of identical spheres. Certain numbers of atoms, $N(a) = \frac{1}{3}(2a+1)(5a^2+5a+3)$, form nearly spherical icosahedra. These have became known as "magic numbers", the lowest three being 13, 55, and 147. Experimentally, icosahedral packing for clusters of fewer than 750 argon atom has been supported by electron diffraction data [14, 15, 16]. Figure 5.1 shows the Mackay icosahedron for 55 atoms which has a Lennard-Jones energy of V_{sol} =-279.248ϵ. To date, no other structure has been found for LJ_{55} with a lower potential energy. Several other higher energy local minima on the PES, referred to as *inherent structures* [64], have been found. One structure, found by construction, has a "needle" shape and though mechanically stable, it is ther-

modynamically unstable [65]. Other inherent structures, found by found by quenching configurations from MD simulations using steepest descent [2, 65], look like the Mackay icosahedra but with a small number of deformations.

The first extensive molecular simulation studies of the melting and freezing of LJ_{55} clusters, done by Briant and Burton [13], showed a sharp, first order-like melting transition in the caloric curve, $\langle E \rangle_T$, similar to the one shown in figure 1.1. These curves and ones generated from subsequent canonical [2] and microcanonical [65] simulations showed hysteresis during heating and subsequent cooling. More recently, smoother caloric curves have been generated from the density of states estimated either using the either the multihistogram method [3, 66, 67] or the superposition harmonic approximation (SHA) method [28, 4]. These two methods were described in chapter 1. Figure 5.2 shows caloric curves generated from canonical MD, multihistogram MD and the SHA method. The heat capacity as a function of temperature can also be obtained by the latter two methods as shown in figure 5.3. With the exception of SHA without anharmonicity, the melting temperature ranges indicated in all the calculations appear to be in reasonable agreement, roughly $0.27\epsilon/k$ to $0.32\epsilon/k$.

As discussed in chapter 1, this temperature range is sometimes called the coexistence range because the cluster fluctuates from the solid phase to the liquid one. The fluctuations can be illustrated by plotting the potential energy as a function of simulation step. This is shown in figure 5.4 for a MC simulation of LJ_{55} at $T = 0.2893\epsilon/k$. The figure shows that cluster has a low potential energy for a short time and then jumps to a higher value where it stays for a long time and then jumps back down to its original value where it remains. The high and low energies correspond to amorphous and ordered configurations respectively. This data suggests that the Landau free energy curve, $F(E)$, for this system would have two minima separated a barrier low enough to permit crossings but high enough to prevent frequent crossings. Lynden-Bell and Wales [5]

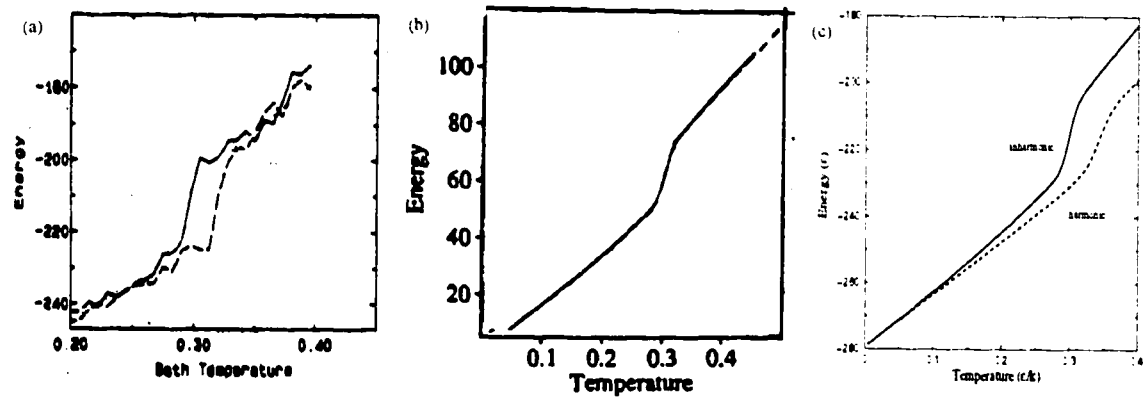

Figure 5.2: Previously computed caloric curves for LJ_{55} . (a) Canonical MD where the solid curves was generated by heating the cluster and the dashed line generated from cooling [2]. (b) Generated from multihistogram data from canonical MC in which the total energy state density is obtained by convoluting $\Omega(U)$ with $\Omega(KE)$ [3]. The energy is relative to V_{sol}. (c) Generated from SHA with and without anharmonicity [4].

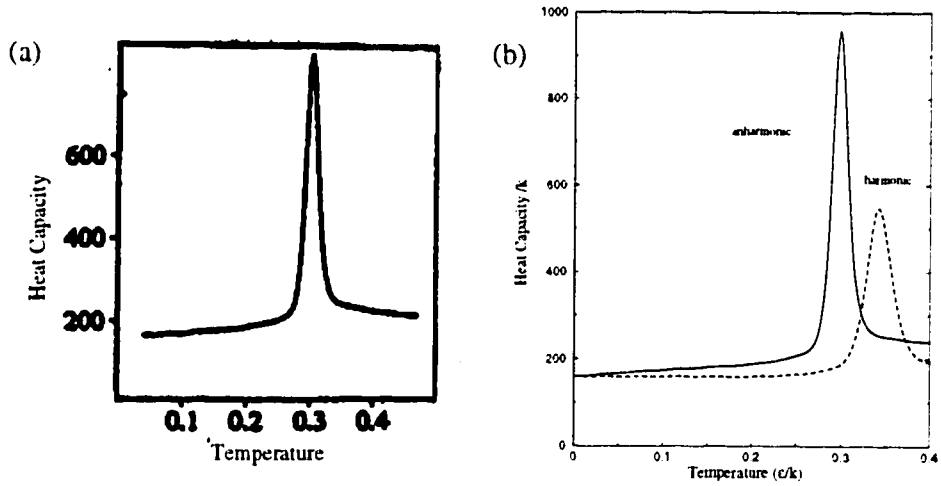

Figure 5.3: Previously computed heat capacities for LJ_{55} . (a) From the same source as figure 5.2b. (b) From the same source as figure 5.2c.

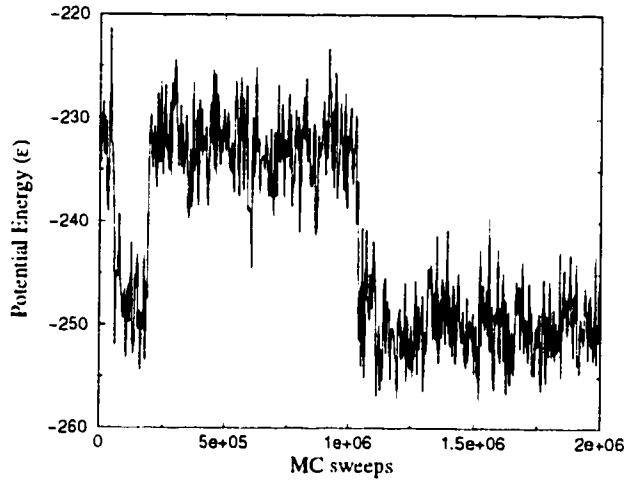

Figure 5.4: Potential energy for LJ_{55} at $T = 0.2893\epsilon/k$.

computed $F(E)$ for several temperatures near and within the coexistence range using canonical MD. Their results, shown in figure 5.5, are consistent with the behavior depicted in figure 5.4. However, obtaining good statistics for this system is difficult because of the infrequent barrier crossings. It has been our experience that even applying umbrella sampling to the problem still resulted in $F(E)$ curves in the coexistence region that did not converge. Better sampling in the coexistence region can be achieved using the multihistogram method or the SHA method to generate $\Omega(E)$. The canonical population distribution is $f(E) = \Omega(E)\exp(-E/kT)$. Like the $F(E)$ curve shown in figure 5.5, $f(E)$ obtained by either method shows bimodal behavior.

A further analysis of the SHA-generated $f(E)$ by Doye and Wales (DW) [4, 29] showed that clusters occupying several potential energy minima in addition to the global one contribute to first peak. The corresponding inherent structures include the deformed icosahedra discussed above as well as a few others. Because the deformations occur on the outermost shell of the icosahedron, these structures have been linked to surface-melting. The idea that large

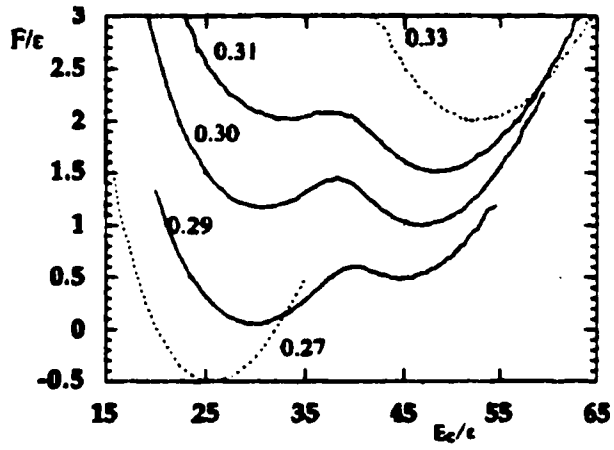

Figure 5.5: Previously computed Landau free energy from canonical MD [5] for several temperatures in and around the coexistence region.

clusters could exhibit surface-melting was first proposed by Briant and Burton [13]. The first computational evidence for LJ_{55} was found by Nauchitel and Pertsin [68] from the radial density distribution function. More recently, Cheng and Berry [69] characterized surface melting of LJ_{55} by calculating layer-by-layer diffusion coefficients. At a temperature near the melting range, the average mean square displacement of atoms in the outermost layer was consistent with a liquid layer while the diffusion was negligible for atoms closer to the center of the cluster.

The picture evoked from such data is of a solid core of atoms covered by a liquid layer. A different scenario suggested by Doye and Wales is that the cluster, in its solid state, occupies the global potential energy minimum and experiences fluctuations which promote it to higher local minima with structures which differ from the icosahedron by the displacement of only a few atoms in the outer shell. The minima range in energy from -276.604ϵ to -271.500ϵ. Similarly, another fluctuation can take the cluster back to the global minimum. This behavior is consistent with the mean square displacement data because upon

returning to the solid, the order of the atoms will likely change causing it to appear diffusive. It also agrees with the early descriptions of LJ_{55} dynamics by Honeycutt and Andersen [2] and Stillinger and Stillinger[65]. A much smaller contribution to the solid peak of $f(E)$ comes from inherent structures which are distorted icosahedra with energies between -271.500ϵ and -268.840ϵ. Above V_{liq}=-268.840ϵ, the minima correspond to amorphous, liquid-like structures and contribute to second peak of $f(E)$.

Only DW have computed the absolute Helmholtz free energy, A, for LJ_{55} . Though, in principle, the Landau free energy in figure 5.5 or the population distributions generated from the multihistogram data could be integrated to determine A but only on a relative scale. Of these three methods, only the SHA method of DW allows separate determination of $\Omega(E)$ and hence of A for each phase. The separation is a result of grouping the inherent structures by phase and doing the sum over just the minima of the group. In this chapter, we present our results, the absolute Helmholtz free energy, A, of solid LJ_{55} and liquid LJ_{55} for a range of temperatures using the FTV and RS methods and compare our results to those of DW.

5.2 FTV Results for LJ_{55}

Using the FTV method, we can estimate the absolute Helmholtz free energy of LJ_{55} for the whole range of temperatures for which the cluster remains intact. The FTV method also allows us to estimate accuracy of the calculations from the upper and lower bounds. Furthermore, the reference states described in chapter 4 enable us to calculate the free energy of LJ_{55} in the solid phase separately from the liquid phase. In this section, we give the technical details for both types of calculations. For the liquid cluster, special measures must be taken when the temperature is within the coexistence range. The reversible

scaling method described in chapter 2 is also applied to both types of calculations and compared to the basic FTV results.

5.2.1 Solid LJ_{55}

The Helmholtz free energy of solid LJ_{55} clusters, A_{sol}, was calculated using the ACNR coordinates and reference state introduced in section 4.2.2. The work was computed as described in section 4.2.3. For each temperature, the radii of the constraining spheres were determined by histograms of the population as a function of distance from the lattice site just as in figure 4.11. The data was collected over 10^7 MC sweeps after an equilibration period of $500,000$ sweeps of a simulation with no volume constraints. Twenty initial configurations for the forward work calculation were also collected over these simulations every 500,000 sweeps. However, at temperatures as low as 0.247 ϵ/k, incidents of atoms on the outer shell of the cluster moving far from their lattice sites without returning were detected. Such events may be caused by a transition to a surface-melted configuration followed by another transition to a solid configuration but with the atoms reordered from the original solid. At $T \geq 0.281\epsilon/k$, these events may also be caused by transitions to a liquid cluster. In either case, these events contaminate the histogram data so, for $T > 0.247\epsilon/k$, small spheres of radius 0.60σ, slightly less than half distance between lattice sites, were imposed in the equilibrium simulation. This volume constraint, while preventing atom exchanges should not interfere with atomic motions of the solid cluster. An example of a histogram taken at a temperature at the high end of this region, $T = 0.3058$, is shown in figure 5.6. For all of the temperatures we used for the solid cluster, 0.0826 - 0.3058 ϵ/k, convergence of the upper and lower bounds was reached within 10^6 sweeps. The free energy of the ACNR reference state was calculated using equation 4.30. Table 5.1 provides the results for each temperature for which A_{sol} was calculated.

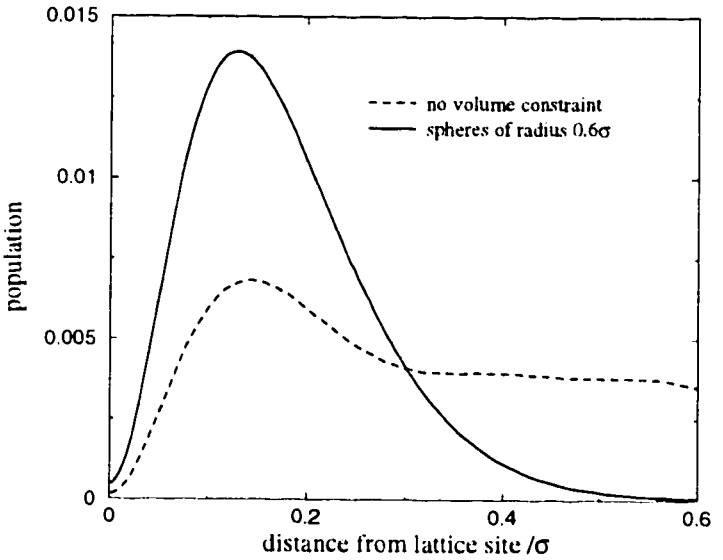

Figure 5.6: Population histograms taken an equilibration simulation at $T = 0.3058$ with and without a volume constraint.

Table 5.1: Results for solid LJ_{55} . The radius indicates the size of the spheres used in calculating ΔA. A_{sol} is given relative to the zero point energy of the cluster, $V_{sol} = -279.248$. The error is taken from equation 2.15

$T/(\epsilon/k)$	$\Delta A/\epsilon$	error/ϵ	radius/σ	A_{sol}/ϵ
0.0826	254.9156	0.0072	0.250	4.4292
0.1653	230.7844	0.0160	0.360	-10.2074
0.2066	216.9649	0.0316	0.430	-20.6282
0.2479	202.7674	0.0249	0.500	-32.6213
0.2686	196.3514	0.0278	0.525	-39.1227
0.2810	191.6939	0.0244	0.550	-43.2028
0.2893	185.9215	0.0522	0.600	-45.9584
0.2975	184.0934	0.0765	0.600	-48.7887
0.3058	182.2926	0.0505	0.600	-51.6651

5.2.2 *Liquid LJ_{55}*

The free energy of liquid LJ_{55} clusters, A_{liq}, was calculated using the CM coordinates and reference state defined in section 4.1.1. The radius of spherical volume constraint was determined by the method described in section 4.1.3. Data for the $\rho(r)$ histograms was taken from equilibration simulations of 10^7 sweeps after an equilibration period of $500,000$ sweeps. Twenty initial configurations needed for the forward work calculation were taken from this simulation every $500,000$ sweeps. When the temperature is low enough to allow coexistence of liquid and solid or surface-melted clusters, some of the collected initial configurations may not be in the liquid phase. The phase of configurations taken from simulations at $T \leq 0.3140$ were checked by the criteria proposed by Doye and Wales described in section 5.1. Each configuration was quenched by the steepest descent method to determine its inherent structure. Only if the energy of the inherent structures was greater than V_{liq} was the configuration considered to be in the liquid phase. If the configuration was not in the liquid phase, it would be reinserted into an equilibration simulation and checked every 10,000 sweeps until it made a transition back to the liquid state. Likewise, the ending configurations from the reverse calculation, were also checked for their phase. If a calculation failed to end in a liquid phase configuration, it was not used in the data accumulation process.

It was assumed that restricting the initial configurations of the forward calculation and the ending configurations of the reverse calculation to those of the liquid phase would guarantee that the resulting ΔA would be the difference between liquid clusters and ideal gas atoms. When the switching of the FTV method is performed slowly enough in the forward direction, the initial liquid configurations can make a transition into a solid state before the inter-atomic interaction becomes too weak to allow such a state. Such an event may also

occur at the end of a reverse calculation. We have found that such events affect both the statistical error of the bound and the convergence of the bounds as shown in figure 5.7a for the extreme low end of the coexistence region, $T = 0.281\epsilon/k$. At 10^7 sweeps, the upper bound starts increasing and the standard error in the mean increases as well.

A possible remedy to this problem is to reject an MC move that results in cluster whose nearest potential energy minimum is lower than V_{liq}. Such a procedure is too computationally expensive to apply because a steepest descent quench would have to performed for MC step. An approximation to this remedy is to check at every sweep is the potential energy is below a certain value and if so perform a quench. If the cluster has become a solid, the calculation must begin again. This procedure is not very expensive for the forward direction because the liquid→solid transition will occur at the beginning of the calculation so starting over does not waste very much time. The reverse calculation does require much more time if many liquid→solid transitions occur. For extreme case of $T = 0.281$, only fourteen replicas out of 120 did not make the transition in a reverse calculation of 10^7 sweeps. The convergence of the upper and lower bounds for this case with the new procedure is shown in figure 5.7b. Unlike the figure above it, the bounds continue to converge for a large number of MC sweeps and the standard error in mean is smaller as well. Given the computational expense of this procedure, using a smaller number of MC sweeps may be preferable. For this case, at 10^6 sweeps, the total error is only 0.0725 compared to 0.0265 for the lengthy computation at 10^7 sweeps. The results for all of the liquid cluster temperatures using the lengthy procedure described above are listed in table 5.2.

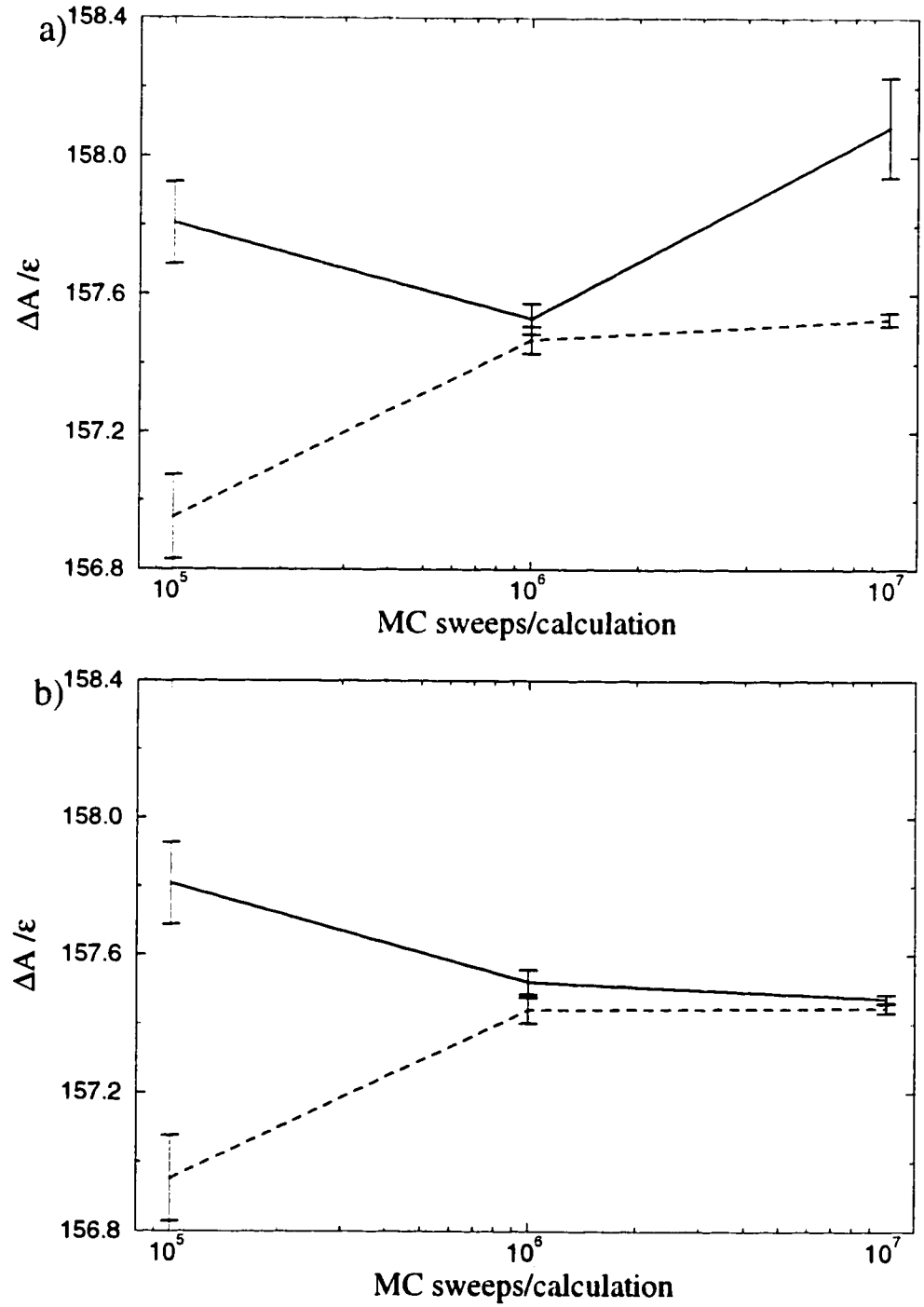

Figure 5.7: Convergence of bounds for $T = 0.281\epsilon/k$ checking only the initial and ending configurations (a) and checking configurations throughout the switching path (b).

Table 5.2: Results for liquid LJ_{55} . The radius indicates the size of the spheres used in calculating ΔA. A_{liq} is given relative to the zero point energy of the cluster, $V_{sol} = -279.248$. The error is taken from equation 2.15

$T/(\epsilon/k)$	$\Delta A/\epsilon$	error/ϵ	radius/σ	A_{liq}/ϵ
0.2810	157.4599	0.0265	3.18	-42.6294
0.2893	155.2275	0.0277	3.18	-45.9121
0.2975	153.0077	0.0151	3.18	-49.2264
0.3058	150.8586	0.0290	3.18	-52.6301
0.3140	148.1190	0.0332	3.22	-56.0980
0.3306	142.6552	0.0239	3.30	-63.1649
0.3719	129.2673	0.0180	3.50	-81.8524
0.4132	117.1670	0.0170	3.65	-101.8471

5.3 RS Results for LJ_{55}

In chapter 2, we described a recently published method, reversible scaling (RS) [51] in which the free energy of the system can be estimated for a range of temperatures from a calculation done at just one temperature. We have applied this method to both solid and liquid clusters using the lowest and highest temperatures of our calculations. The liquid calculation, performed at $T = 0.4132\epsilon/k$, has the same problems regarding liquid→solid transitions as the previous calculations. To avoid the transitions, the number of sweeps used in the switching path is reduced. Only a small number, 10^5, is needed for the data to converge because the change the system undergoes, from a hot liquid cluster to a cold one, is less severe than switching to an ideal gas. For solid clusters, we performed the calculation at $T = 0.0826\epsilon/k$ and used the sphere size of the highest temperature solid, $T = 0.3058\epsilon/k$ with a switching time of 10^6. The results for both types of clusters are shown in figure 5.8 along with the

data from tables 5.1 and 5.2. The curves are interpolations of RS data points, 51 for the solid cluster and 26 for liquid cluster. The standard error in the mean in the RS data and the error in the FTV values from the tables are too small to discern on this scale. For most of the temperatures, the agreement between the two types of data is quite good. The worst discrepancy is at the end point of each curve in the coexistence region. At $T = 0.3058\epsilon/k$, the difference between A_{FTV} and A_{RS} of the solid cluster is 0.0140ϵ which is well within the estimated error of the FTV value. For the liquid cluster at $T = 0.2810\epsilon/k$, the difference between A_{FTV} and A_{RS} is 0.0683ϵ which is 2.5 times greater than the FTV error. This discrepancy can be improved by increasing the switching time but then the clusters are more likely to make a *liquid* $\rightarrow$ *solid* transition. However, even for the short switching times, the error is still reasonable. Figure 5.9 is a magnification of figure 5.8 showing only the coexistence temperature range. Even on this scale, the discrepancies described above are almost indiscernible. Thus, the RS method allows us to generate the free energy for whole temperature range from calculations at just two temperatures thereby greatly decreasing the amount of computation time.

5.4 Discussion

Though a wealth of data for LJ_{55} can be found in the literature, only one paper contains recent estimates for the absolute Helmholtz free energy to which we can compare our results. Another piece of data obtained from our results is the melting temperature, the temperature at which the solid and liquid clusters have equal free energies. Several previous studies have made estimates of this value. Lastly, because the RS method provides A for many temperatures, we can also use our data to obtain the caloric curve. In this section, we show how our data compares to other computational studies of LJ_{55} .

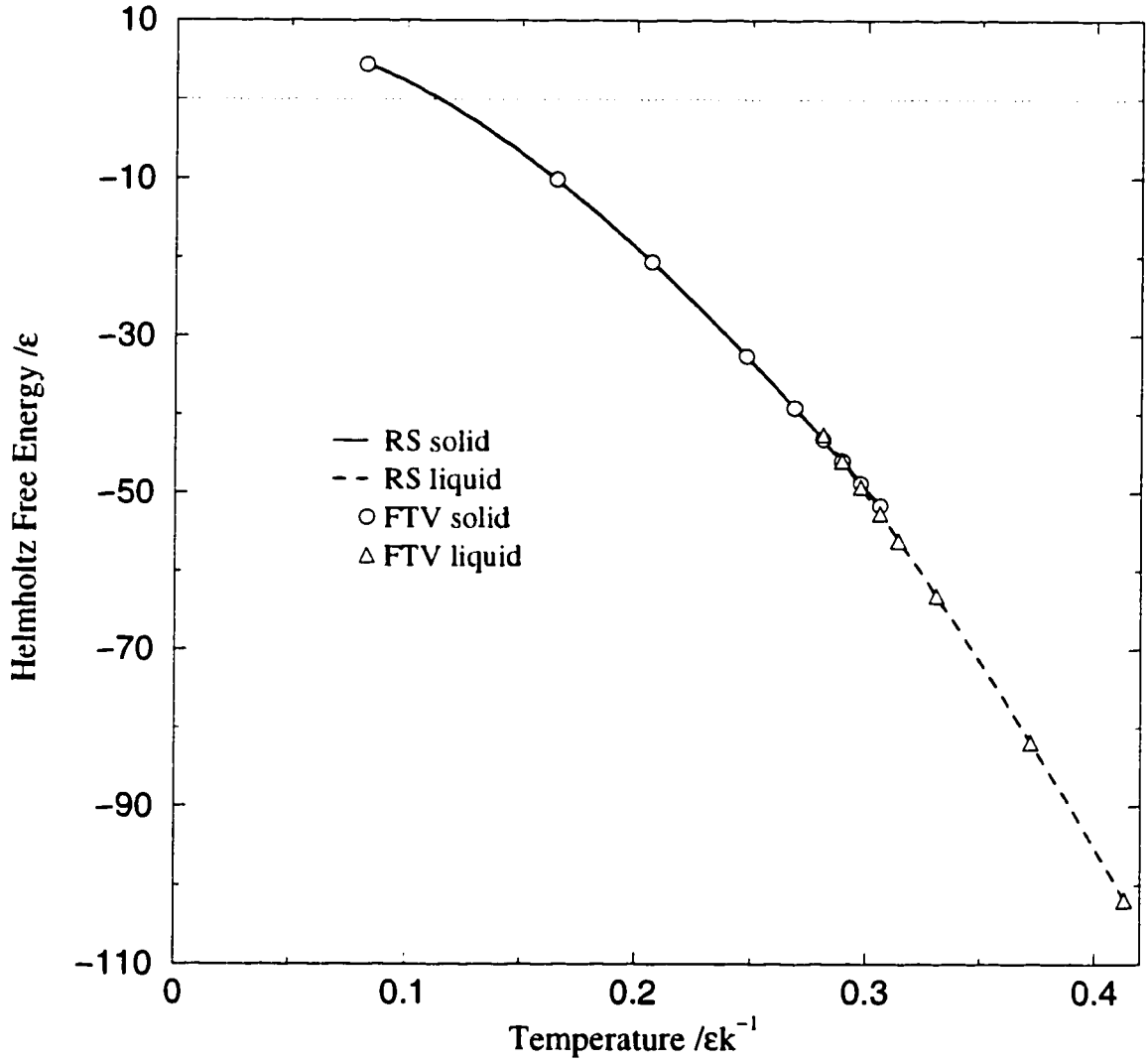

Figure 5.8: Free energy of LJ_{55} for both solid and liquid clusters. The curves are generated from the RS method. Free energies are given relative to V_{sol}

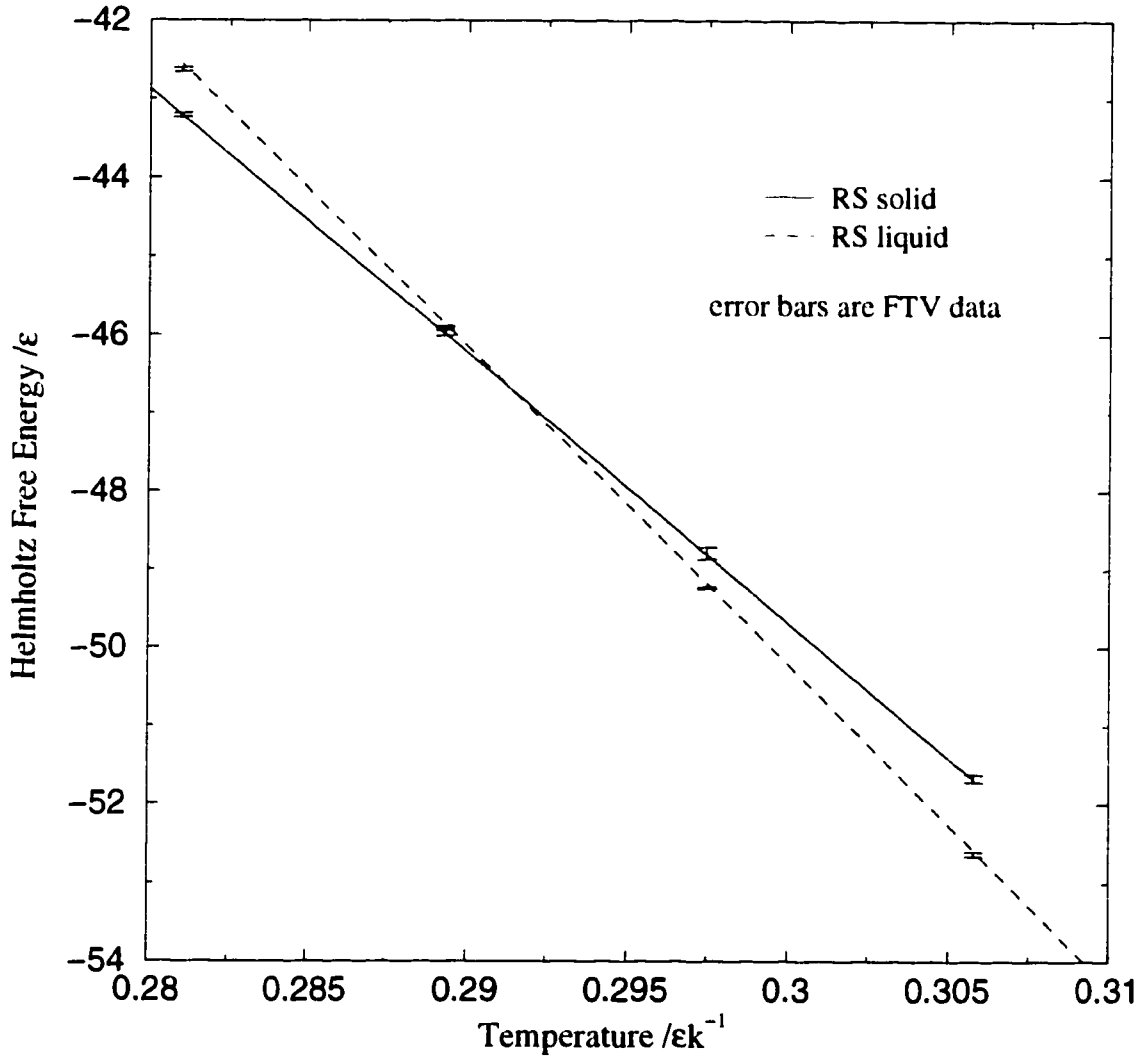

Figure 5.9: Free energy of LJ_{55} for both solid and liquid clusters in the coexistence range.

Doye and Wales (DW) [4] used the SHA method with anharmonic effects to compute the density of states for LJ_{55} from which they obtained several thermodynamic properties, among them the Helmholtz free energy on an absolute scale. Because the SHA method results in only the vibrational density of states the DW results do not include translational, A_{trans}, and rotational, A_{rot}, free energies. All of our free energy results presented so far also do not include A_{trans} (see equation 4.32) but they do include A_{rot}. In order to compare our results to theirs, we approximated A_{rot} as

$$A_{rot} = -kT \ln \left(8\pi^2 \mathbf{I} kT/h^2\right) \tag{5.1}$$

where the value of **I**, the moment of inertia, was taken from averages over the equilibrium simulations used to obtain the initial configurations for the ΔA calculations. The error in A_{rot}, estimated from the standard error in the mean of **I**, ranges from 5.2×10^{-4} to 1.8×10^{-2}. Our FTV data with A_{rot} subtracted out is shown in figure 5.10 along with the DW results with and without anharmonicity. The error bars show the combined error from the FTV calculation and from the error in A_{rot}. The FTV data is in reasonably close agreement to the DW anharmonic results. In the coexistence range, they are expected to differ because the DW data has contributions from all of the phases. The agreement is best at the low temperatures where anharmonic effects are small. At higher temperatures, either our calculation undercounts configurations or the DW calculation over counts. Possible causes of undercounting in our methods could stem from the nature the volume constraints or, in the case of liquid clusters, the definition of an intact cluster. However, the population distributions in figures 4.5 and 4.10 indicate that configurations neglected for these reasons are not likely to contribute significantly to the partition function. In fact, the DW data is more likely to suffer than our data from neglected configurations because of the limited number of potential energy minima used in their SHA calculations.

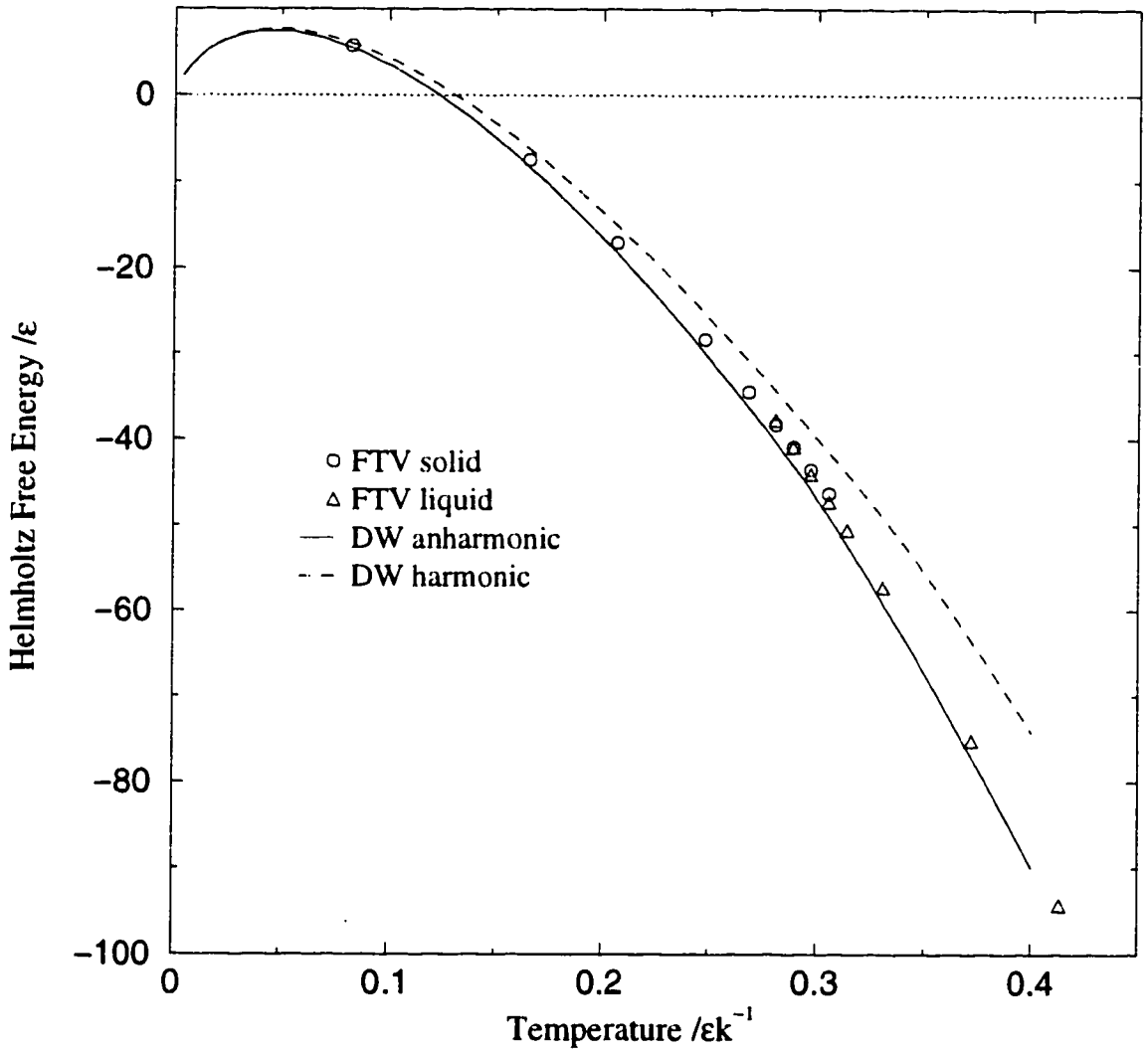

Figure 5.10: Free energy of LJ_{55} with A_{rot} subtracted out, FTV results and DW results. Free energies are given relative to V_{sol}.

Another important quantity that can be determined from our data is the melting temperature. In figure 5.9, the solid and liquid RS curves cross at $T_m = 0.2913\epsilon/k$ indicating the temperature at which the solid and liquid free energies are equal. Previous estimates of T_m have been made in a variety of ways. The peak in the heat capacity, as in figure 5.3, has been taken as one measure. Both Labastie and Whetten [3] and Cheng and Berry [66] have evaluated $T_m = 0.30\epsilon/k$ in this way. Stillinger and Stillinger [65] used the average of the kinetic energies of solid and liquid branches from the caloric curve in the coexistence region to get $T_m = 0.278\epsilon/k$. Lynden-Bell and Wales estimated T_m using the canonical population distribution obtained from the Landau free energy in figure 5.5 at $0.2982\epsilon/k$. They fit each peak with a Gaussian and determined the temperature at which the area under the peaks are equal. Our value for T_m is not entirely comparable to these numbers because the surface-melted clusters do not contribute to our value A_{sol}. In the DW work, on the other hand, separate probabilities, $p_i(T)$ for solid, surface-melted, and liquid clusters were found using $p_i(T) = Q_i(T)/Q(T)$. If the solid and surface-melted states are grouped together, $T_m = 0.2985\epsilon/k$ but if only the solid $p_i(T)$ is compared with the liquid, $T_m = 0.2949\epsilon/k$. This number is still slightly higher than our estimate of T_m.

One more analysis of our data comes from using the RS data to generate a caloric curve. In the canonical ensemble, $\langle E \rangle = kT^2 (\partial \ln Q/\partial T)$. Using the RS method, values of A and hence Q can be determined at enough temperatures to approximate $\partial \ln Q/\partial T$ using the simple formula, $f'(x) = (f(x+h) - f(x))/h$. The results are shown in figure 5.11 along with the DW caloric curve that is also shown in figure 5.2c. The triangles and circles are average energies from the equilibrated MC simulations used to generate the initial configurations for the liquid and solid FTV calculations respectively. In the coexistence region, the liquid MC average has contributions from solid and surface-melted configura-

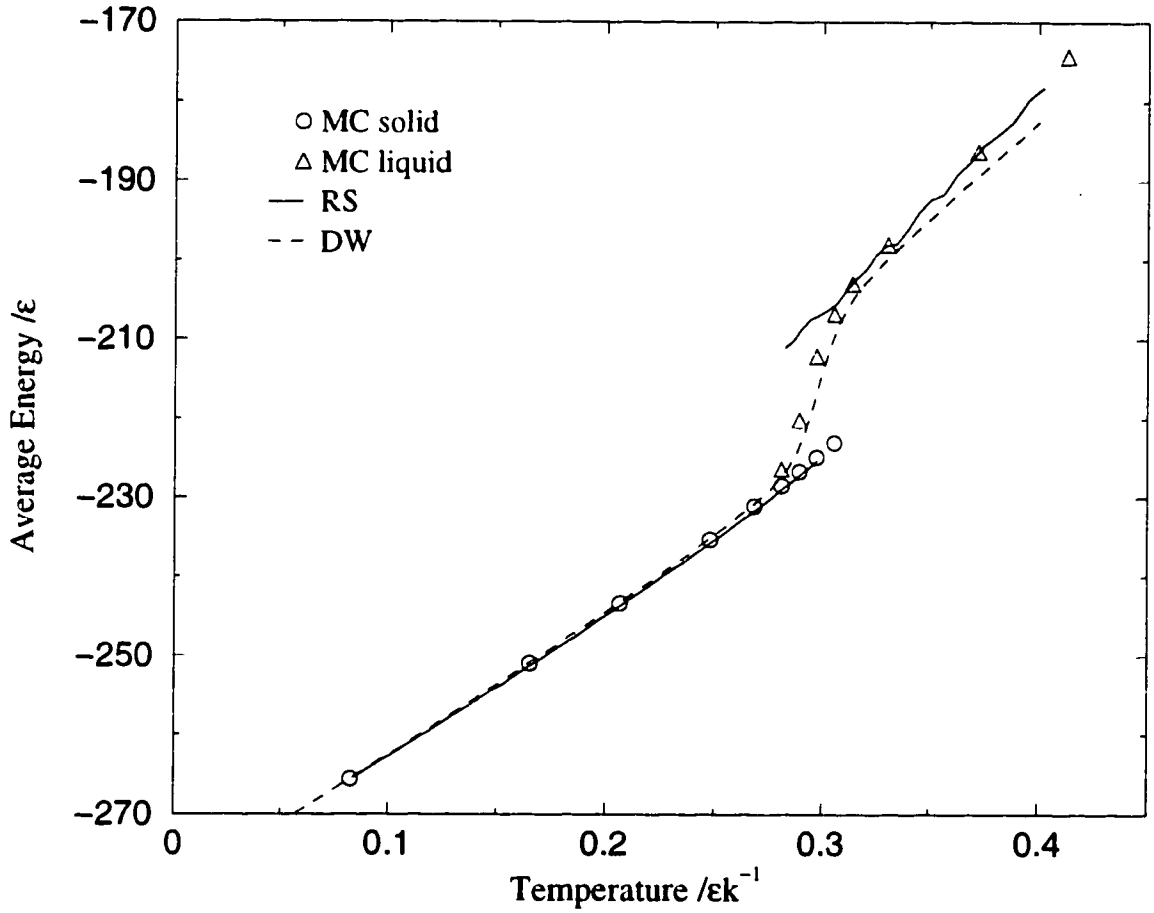

Figure 5.11: Caloric curve from RS data and from DW. The circles and triangles are from equilibrated MC simulations.

tions as well as liquid ones. The solid MC average, however, was constrained to allow only solid configurations. Just as in figure 5.10, the worst disagreement between the RS and the DW data is at high temperatures. The MC data agrees with the RS data at both high and low temperatures.

DW list three sources of error in the SHA. An obvious potential problem is an incomplete set of minima. They found their minima by quenching MD trajectories run at only two energies: one within the coexistence region and one slightly higher. Furthermore, their results also depend on a weighting factor which is determined by how many times a quench ends up a particular minimum. A lack of ergodicity in the MD sampling could result in missing some minima or an incorrect weighting. However, under counting the minima and quench statistics would result in an underestimate of the density of states and a corresponding overestimate of $A(T)$. In contrast, the DW anharmonic curve in figure 5.10 is lower than our curve. Another source of error comes from the harmonic approximation. The higher energy minima are likely flatter than a harmonic well and thus the approximation would result in an underestimate of the density of states. This underestimate is shown clearly in the difference between the solid and dashed curves in figure 5.10. Because the anharmonic curve is too low, it appears that the shape of the minima have been accounted for in their method. Lastly, the SHA relies on the assumption that the phase volumes for each minima can summed independently. If there is overlap, the SHA free energy will be underestimated. The overlap would be greatest at higher temperatures where our data and the difference with DW anharmonic data are the greatest. Because no explicit methods were used to combat this problem, it may be the cause of the disagreement.

5.5 Summary and Conclusions

We have presented a novel implementation of both the FTV and RS methods in applying them to atomic clusters. The success of this application relies strongly on the reference state used. All but one of the four reference states presented in this thesis are introduced and implemented for the first time. For larger clusters which undergo a first order-like transition, the optimal reference state for solid clusters uses ACNR coordinates while the CM reference state is the best one for liquid clusters. We have shown that using these reference states, the free energy of solid and liquid clusters can be calculated separately unlike other published methods with the exception of the SHA method of DW. From the FTV results of only the highest and lowest temperatures in the relevant range, the RS method gave the free energy of LJ_{55} for all the intermediate temperatures which were consistent with the more time-consuming FTV calculations. Furthermore, having $A(T)$ for so many temperatures permitted approximations of the caloric curve.

The free energy calculations had several checks for accuracy. First, the four reference states were shown to be consistent by providing the same result for the free energy of LJ_4. Secondly, in chapter 3, the free energy difference of LJ_{13} and the CM reference state calculated by FTV and TI agreed to well within the estimated uncertainties. Also, the caloric curve for LJ_{55} generated from the RS data agreed well with MC simulation data points.

The only other published method from which the free energy of different phases of an atomic cluster can be computed separately is the DW method which employs the SHA with anharmonic effects and identification of which parts of the PES contribute to each phase. While our method does not provide as much thermodynamic information as DW one, it requires less information about the PES and less computation. Additionally, an estimate of the system-

atic error can be determined from the upper and lower bounds on ΔA. Our results for LJ_{55} did not show exact agreement with the results of DW in the free energy curve, the caloric curve and melting temperature. However, given the consistency checks listed above, the differences are likely due to the nature of the DW methods.

Finally, the FTV and RS methods for atomic clusters are easily transferable to other atomic clusters, molecular clusters and large molecules. Using the ACNR reference state with the FTV method is particularly suited for determining the order of stability of different solid geometric isomers. For instance, the method could be used to determine which of the many predicted structures of $(H_2O)_{20}$ [19, 21, 22, 23] are the most stable for a range of temperatures. More complex applications may also be possible.

BIBLIOGRAPHY

[1] M. A. Miller, L. M. Amon and W. P. Reinhardt, Phys. Rev. Lett., submitted ().

[2] J. D. Honeycutt and H. C. Andersen, J. Phys. Chem. **91**, 4950 (1987).

[3] P. Labastie and R. L. Whetten, Phys. Rev. Lett. **65**, 1567 (1990).

[4] J. P. K. Doye and D. J. Wales, J. Chem. Phys. **102**, 9659 (1995).

[5] R. M. Lynden-Bell and D. J. Wales, J. Chem. Phys. **101**, 1460 (1994).

[6] F. H. Stillinger and D. K. Stillinger, J. Chem. Phys. **93**, 6106 (1990).

[7] C. J. Cerjan and W. H. Miller, J. Chem. Phys. **75**, 2800 (1981).

[8] J. P. K. Doye and D. J. Wales, Z. Phys. D **40**, 194 (1997).

[9] S. Kirkpatrick, C. D. Gelatt and M. P. Vecchi, Science **220**, 671 (1983).

[10] M. A. Moret, P. G. Pascutti, P. M. Bisch and K. C. Mundim, J. Comp. Chem. **19**, 647 (1998).

[11] J. Mestres and G. E. Scuseria, J. Comp. Chem. **16**, 729 (1995).

[12] R. S. Berry, T. L. Beck and H. L. Davis, Adv. Chem. Phys. **70B**, 75 (1988).

[13] C. L. Briant and J. J. Burton, J. Chem. Phys. **63**, 2045 (1975).

[14] J. Farges, M. F. de Feraudy, B. Faoult and G. J. Torchet, J. Chem. Phys. **78**, 5067 (1983).

[15] J. Farges, M. F. de Feraudy, B. Faoult and G. J. Torchet, Surf. Sci. **156**, 370 (1985).

[16] J. Farges, M. F. de Feraudy, B. Faoult and G. J. Torchet, J. Chem. Phys. **84**, 3491 (1986).

[17] T. L. Hill, *Thermodynamics of Small Systems*, W. A. Benjamin, New York (1963).

[18] J. Jellinek, T. L. Beck and R. S. Berry, J. Chem. Phys. **84**, 2783 (1986).

[19] C. J. Tsai and K. D. Jordan, J. Phys. Chem. **97**, 5208 (1993).

[20] D. J. Wales and I. Ohmine, J. Chem. Phys. **98**, 7245 (1993).

[21] D. J. Wales and M. P. Hodges, Chem. Phys. Lett. **286**, 65 (1998).

[22] L. S. Sremaniak, L. Perera and M. L. Berkowitz, J. Chem. Phys. **105**, 3715 (1996).

[23] A. Khan, Chem. Phys. Lett. **217**, 443 (1994).

[24] K. J. Oh and X. C. Zeng, J. Chem. Phys. **108**, 4683 (1998).

[25] D. J. McGinty, J. Chem. Phys. **55**, 580 (1974).

[26] J. K. Lee, J. A. Barker and F. F. Abraham, J. Chem. Phys. **58**, 3166 (1973).

[27] G. Herzberg, *Molecular Spectra and Molecular Structure*, Van Nostrand, Princeton (1945).

[28] D. J. Wales, Mol. Phys. **78**, 151 (1993).

[29] J. P. K. Doye and D. J. Wales, J. Chem. Phys. **102**, 9673 (1995).

[30] N. Metropolis, A. W. Rosenbluth, M. N. Rosenbluth, A. H. Teller and E. Teller, J. Chem. Phys. **21**, 1087 (1953).

[31] H. C. Andersen, J. Chem. Phys. **72**, 2384 (1980).

[32] W. G. Hoover, Phys. Rev. A **31**, 1695 (1985).

[33] S. Nóse, J. Chem. Phys. **81**, 511 (1984).

[34] G. M. Torrie and J. P. Valleau, J. Comp. Phys. **23**, 187 (1977).

[35] A. M. Ferrenberg and R. H. Swendsen, Phys. Rev. Lett. **63**, 1195 (1989).

[36] C. J. Tsai and K. D. Jordan, J. Chem. Phys. **99**, 6957 (1993).

[37] D. D. Frantz, D. L. Freeman and J. D. Doll, J. Chem. Phys. **93**, 2769 (1990).

[38] T. P. Straatsma and J. A. McCammon, Ann. Rev. Phys. Chem. **43**, 407 (1992).

[39] D. L. Beveridge and F. M. DiCapua, Ann. Rev. Biophys. Biophys. Chem. **18**, 431 (1989).

[40] R. W. Zwanzig, J. Chem. Phys. **22**, 1420 (1954).

[41] C. H. Bennett, J. Comp. Phys. **22**, 245 (1976).

[42] J. G. Kirkwood, J. Chem. Phys. **3**, 300 (1935).

[43] H. J. C. Berendsen, J. P. M. Postma and W. F. vanGunsteren, in *Molecular Dynamics and Protein Stucture*, edited by J. Hermans, p. 43, Polycrystal Bookservice, Illinois (1985).

[44] U. C. Singh, F. K. Brown, P. A. Bash and P. A. Kollman, J. Am. Chem. Soc. **109**, 1607 (1987).

[45] T. P. Straatsma, H. J. C. Berendsen and J. P. M. Postma, J. Chem. Phys. **85**, 6720 (1986).

[46] M. Watanabe and W. P. Reinhardt, Phys. Rev. Lett. **65**, 3301 (1990).

[47] W. P. Reinhardt and J. E. Hunter III, J. Chem. Phys. **97**, 1599 (1992).

[48] J. E. Hunter III, W. P. Reinhardt and T. F. Davis, J. Chem. Phys. **99**, 6856 (1993).

[49] C. Jarzynski, Phys. Rev. Lett. **78**, 2690 (1997).

[50] C. Jarzynski, J. Chem. Phys. **56**, 5018 (1997).

[51] M. de Koning, A. Antonelli and S. Yip, Phys. Rev. Lett. **83**, 3973 (1999).

[52] W. W. Wood and J. D. Jacobson, in *Proceedings of the Western Joint Computer Conference* (March 1959).

[53] W. B. Streett and D. J. Tildesley, Proc. R. Soc. Lond. A **348**, 485 (1976).

[54] M. P. Allen and D. J. Tildesley, *Computer Simulations of Liquids*, Oxford University Press, New York (1987).

[55] D. Frenkel and B. Smit, *Understanding Molecular Simulation*, Academic Press, San Diego (1996).

[56] W. P. Reinhardt, L. M. Amon and M. A. Miller, J. Chem. Phys., to be submitted ().

[57] V. I. Manousiouthakis and M. W. Deem, J. Chem. Phys. **110**, 2753 (1999).

[58] H. Flyvbjerg and H. G. Petersen, J. Chem. Phys. **91**, 461 (1989).

[59] D. Frenkel and A. J. C. Ladd, J. Chem. Phys. **81**, 3188 (1984).

[60] F. Calvo and P. Labastie, Eur. Phys. J. D **3**, 229 (1998).

[61] J. J. Burton, Nature **229**, 335 (1971).

[62] M. R. Hoare and P. Pal, Adv. Phys. **20**, 161 (1972).

[63] A. C. Mackay, Acta. Crystallogr. **15**, 916 (1962).

[64] F. H. Stillinger and T. A. Weber, Phys. Rev. A **25**, 978 (1982).

[65] F. H. Stillinger and D. K. Stillinger, J. Chem. Phys. **93**, 6013 (1990).

[66] H. Cheng, X. Li, R. L. Whetten and R. S. Berry, Phys. Rev. A **46**, 791 (1992).

[67] F. Calvo and P. Labastie, Chem. Phys. Lett. **247**, 395 (1995).

[68] V. V. Nauchitel and A. J. Pertsin, Mol. Phys. **40**, 1341 (1980).

[69] H. Cheng and R. S. Berry, Phys. Rev. A **45**, 7969 (1992).

Appendix A

DERIVATION OF THE PARTITION FUNCTION FOR THE IDEAL GAS IN CM COORDINATES

The following is Lee, Baker and Abraham's derivation of $Q_{cm_{gas}}$ in equation 4.10. Our notation is slightly different in that the N^3 term resulting from the Jacobian is included in $Q_{cm_{gas}}$.

We begin with equation 4.7 and replace $\exp(-H_{LJ_{cm}}/kT)$ with 1 because the Hamiltonian for ideal gas particles is zero.

$$Q_{cm_{gas}} = N^3 \int_{\widetilde{C}(R_c)} \cdots \int d\mathbf{r}'_2, \ldots dr'_N \tag{A.1}$$

where the primed variables are the CM coordinates in equation 4.3. The subscript $\widetilde{C}(R_c)$ indicates that the integration is performed under the constraint in equation 4.8.

The following step functions are defined:

$$g(\mathbf{r}'_i) = 1 \qquad \text{for} |\mathbf{r}'_i| \leq R_c, \qquad i = 2, \ldots, N \tag{A.2}$$

$$g(\mathbf{r}'_i) = 0 \qquad \text{for} |\mathbf{r}'_i| > R_c \tag{A.3}$$

and

$$\begin{aligned} g(\mathbf{r}'_{sum}) &= 1 \qquad \text{for} |\mathbf{r}'_{sum}| \leq R_c \\ g(\mathbf{r}'_{sum}) &= 0 \qquad \text{for} |\mathbf{r}'_{sum}| > R_c \end{aligned} \tag{A.4}$$

where $\mathbf{r}_{sum} = \sum_{i=2}^{N} \mathbf{r}'_i$. The Fourier transformations of $g(\mathbf{r}'_i)$ and $g(\mathbf{r}'_i)$ are

$$G(\mathbf{K}_i) = (2\pi)^{-3/2} \iiint_{-\infty}^{\infty} g(\mathbf{r}'_i) \exp(-i\mathbf{K}_i \cdot \mathbf{r}'_i) d\mathbf{r}_i$$
$$G(\mathbf{K}_{sum}) = (2\pi)^{-3/2} \iiint_{-\infty}^{\infty} g(\mathbf{r}'_{sum}) \exp(-i\mathbf{K}_i \cdot \mathbf{r}'_{sum}) d\mathbf{r}_i \qquad \text{(A.5)}$$

respectively. Inserting equations A.4 and A.5 into equation A.1 yields

$$\begin{aligned} Q_{cm_{gas}} =& N^3 (2\pi)^{-3/2} \int \cdots \int_{-\infty}^{\infty} G(\mathbf{K}_2) \ldots G(\mathbf{K}_N) \\ & \times G(\mathbf{K}_{sum}) \exp[i(\mathbf{K}_{sum} \cdot \mathbf{r}'_{sum} + \sum_{i=2}^{N} \mathbf{K}_i \cdot \mathbf{r}'_i)] \qquad \text{(A.6)} \\ & d\mathbf{r}'_2, \ldots d\mathbf{r}'_N d\mathbf{K}_2 \ldots d\mathbf{K}_N d\mathbf{K}_{sum}. \end{aligned}$$

Equation A.6 can be simplified by the following equalities associated with Dirac δ-functions:

$$\iiint_{-\infty}^{\infty} \exp[i(\mathbf{K}_i \cdot \mathbf{r}'_{sum} + \mathbf{K}_{sum} \cdot \mathbf{r}'_{sum})] d\mathbf{r}_i = (2\pi)^3 \delta(\mathbf{K}_i + \mathbf{K}_{sum}) \qquad \text{(A.7)}$$

and

$$\iiint_{-\infty}^{\infty} \delta(\mathbf{K}_i + \mathbf{K}_{sum}) G(\mathbf{K}_i) d\mathbf{K}_i = G(-\mathbf{K}_{sum}). \qquad \text{(A.8)}$$

The result is

$$Q_{cm_{gas}} = N^3 (2\pi)^{-3/2} (2\pi)^{3(N-1)} \iiint_{-\infty}^{\infty} [G(\mathbf{K}_{sum})]^N d\mathbf{K}_{sum}. \qquad \text{(A.9)}$$

Using the definition of $G(\mathbf{K}_{sum})$ in equation A.5,

$$G(\mathbf{K}_{sum}) = (2\pi)^{-3/2} \int_0^{R_c} 2\pi r_{sum}^2 dr_{sum} \int_0^{\pi} \exp(-ik_{sum} r_{sum} \cos\phi) \sin\phi d\phi \qquad \text{(A.10)}$$
$$= (2\pi)^{-3/2} 4\pi \frac{\sin(k_{sum}R_c) - k_{sum}R_c \cos(k_{sum}R_c)}{k_{sum}^3} \qquad \text{(A.11)}$$

where spherical coordinates are used for the integration. This expression for $G(\mathbf{K}_{sum})$ can be inserted back into equation A.9 resulting in

$$Q_{cm_{gas}} = N^3 3^{N-1} \left(\frac{4\pi}{3} R_c^3\right)^{N-1} \frac{2}{\pi} \int_{\infty}^{0} \left(\frac{\sin x - x\cos x}{x^3}\right)^N x^2 dx \qquad \text{(A.12)}$$

where $x = k_{sum}R_c$. The integral in equation A.12 can be solved numerically.

Appendix B

JACOBIANS USED FOR TRANSFORMATION OF VARIABLES: CM AND AC COORDINATES

In this appendix, we show how the Jacobians required for the CM and AC coordinate tranformations in chapter 4 are derived.

B.1 CM coordinates

The Jacobian needed to make the coordinate transformation in equation 4.3 is represented by

$$\frac{\partial(x_1, x_2, \ldots, x_N, y_1, y_2, \ldots, y_N, z_1, z_2, \ldots, z_N)}{\partial(X_{cm}, x'_2, \ldots, x'_N, Y_{cm}, y'_2 \ldots, y'_N, Z_{cm}, z'_2, \ldots, z'_N)} = |\mathbf{A}_{cm}| \qquad \text{(B.1)}$$

where $\mathbf{A}_{cm}$ is the $3N \times 3N$ matrix

$$\mathbf{A}_{cm} = \begin{pmatrix}
\frac{\partial x_1}{\partial X_{cm}} & \cdots & \frac{\partial x_N}{\partial X_{cm}} & \frac{\partial x_N}{\partial X_{cm}} & \frac{\partial y_1}{\partial X_{cm}} & \cdots & \frac{\partial y_N}{\partial X_{cm}} & \frac{\partial y_N}{\partial X_{cm}} & \frac{\partial z_1}{\partial X_{cm}} & \cdots & \frac{\partial z_N}{\partial X_{cm}} & \frac{\partial z_N}{\partial X_{cm}} \\
\frac{\partial x_1}{\partial x'_2} & \cdots & \frac{\partial x_N}{\partial x'_2} & \frac{\partial x_N}{\partial x'_2} & \frac{\partial y_1}{\partial x'_2} & \cdots & \frac{\partial y_N}{\partial x'_2} & \frac{\partial y_N}{\partial x'_2} & \frac{\partial z_1}{\partial x'_2} & \cdots & \frac{\partial z_N}{\partial x'_2} & \frac{\partial z_N}{\partial x'_2} \\
\vdots & & \vdots & \vdots & \vdots & & \vdots & \vdots & \vdots & & \vdots & \vdots \\
\frac{\partial x_1}{\partial x'_N} & \cdots & \frac{\partial x_N}{\partial x'_N} & \frac{\partial x_N}{\partial x'_N} & \frac{\partial y_1}{\partial x'_N} & \cdots & \frac{\partial y_N}{\partial x'_N} & \frac{\partial y_N}{\partial x'_N} & \frac{\partial z_1}{\partial x'_N} & \cdots & \frac{\partial z_N}{\partial x'_N} & \frac{\partial z_N}{\partial x'_N} \\
\frac{\partial x_1}{\partial Y_{cm}} & \cdots & \frac{\partial x_N}{\partial Y_{cm}} & \frac{\partial x_N}{\partial Y_{cm}} & \frac{\partial y_1}{\partial Y_{cm}} & \cdots & \frac{\partial y_N}{\partial Y_{cm}} & \frac{\partial y_N}{\partial Y_{cm}} & \frac{\partial z_1}{\partial Y_{cm}} & \cdots & \frac{\partial z_N}{\partial Y_{cm}} & \frac{\partial z_N}{\partial Y_{cm}} \\
\frac{\partial x_1}{\partial y'_2} & \cdots & \frac{\partial x_N}{\partial y'_2} & \frac{\partial x_N}{\partial y'_2} & \frac{\partial y_1}{\partial y'_2} & \cdots & \frac{\partial y_N}{\partial y'_2} & \frac{\partial y_N}{\partial y'_2} & \frac{\partial z_1}{\partial y'_2} & \cdots & \frac{\partial z_N}{\partial y'_2} & \frac{\partial z_N}{\partial y'_2} \\
\vdots & & \vdots & \vdots & \vdots & & \vdots & \vdots & \vdots & & \vdots & \vdots \\
\frac{\partial x_1}{\partial y'_N} & \cdots & \frac{\partial x_N}{\partial y'_N} & \frac{\partial x_N}{\partial y'_N} & \frac{\partial y_1}{\partial y'_N} & \cdots & \frac{\partial y_N}{\partial y'_N} & \frac{\partial y_N}{\partial y'_N} & \frac{\partial z_1}{\partial y'_N} & \cdots & \frac{\partial z_N}{\partial y'_N} & \frac{\partial z_N}{\partial y'_N} \\
\frac{\partial x_1}{\partial Z_{cm}} & \cdots & \frac{\partial x_N}{\partial Z_{cm}} & \frac{\partial x_N}{\partial Z_{cm}} & \frac{\partial y_1}{\partial Z_{cm}} & \cdots & \frac{\partial y_N}{\partial Z_{cm}} & \frac{\partial y_N}{\partial Z_{cm}} & \frac{\partial z_1}{\partial Z_{cm}} & \cdots & \frac{\partial z_N}{\partial Z_{cm}} & \frac{\partial z_N}{\partial Z_{cm}} \\
\frac{\partial x_1}{\partial z'_2} & \cdots & \frac{\partial x_N}{\partial z'_2} & \frac{\partial x_N}{\partial z'_2} & \frac{\partial y_1}{\partial z'_2} & \cdots & \frac{\partial y_N}{\partial z'_2} & \frac{\partial y_N}{\partial z'_2} & \frac{\partial z_1}{\partial z'_2} & \cdots & \frac{\partial z_N}{\partial z'_2} & \frac{\partial z_N}{\partial z'_2} \\
\vdots & & \vdots & \vdots & \vdots & & \vdots & \vdots & \vdots & & \vdots & \vdots \\
\frac{\partial x_1}{\partial z'_N} & \cdots & \frac{\partial x_N}{\partial z'_N} & \frac{\partial x_N}{\partial z'_N} & \frac{\partial y_1}{\partial z'_N} & \cdots & \frac{\partial y_N}{\partial z'_N} & \frac{\partial y_N}{\partial z'_N} & \frac{\partial z_1}{\partial z'_N} & \cdots & \frac{\partial z_N}{\partial z'_N} & \frac{\partial z_N}{\partial z'_N}
\end{pmatrix}$$

which can be broken down into nine $N \times N$ matrices

$$\mathbf{A}_{cm} = \begin{vmatrix} \mathbf{B}_{cm} & \mathbf{0} & \mathbf{0} \\ \mathbf{0} & \mathbf{B}_{cm} & \mathbf{0} \\ \mathbf{0} & \mathbf{0} & \mathbf{B}_{cm} \end{vmatrix}$$

where $\mathbf{0}$ represents an $N \times N$ matrix of zeros and

$$\mathbf{B}_{cm} = \begin{pmatrix} 1 & 1 & 1 & \ldots 1 \\ -1 & 1 & 0 & \ldots 0 \\ -1 & 0 & 1 & \ldots 0 \\ \vdots & & & \\ -1 & 0 & 0 & \ldots 1 \end{pmatrix}$$

is also an $N \times N$ matrix. We obtain the matrix $\mathbf{B}'_{cm}$ by consecutively adding the $i+1$ column to the first column where $i = 1$ for the first operation and increases

by one every operation until $i = N - 1$.

$$\mathbf{B}'_{cm} = \begin{pmatrix} N & 1 & \ldots 1 & 1 \\ 0 & 1 & \ldots 0 & 0 \\ \vdots & & & \\ 0 & 0 & \ldots 1 & 0 \\ 0 & 0 & \ldots 0 & 1 \end{pmatrix} \tag{B.2}$$

By the rules of determinants:

$$|\mathbf{B}'_{cm}| = N \tag{B.3}$$

$$|\mathbf{B}_{cm}| = |\mathbf{B}'_{cm}| = N \tag{B.4}$$

$$|\mathbf{A}_{cm}| = |\mathbf{B}_{cm}|^3 = N^3 \tag{B.5}$$

B.2 AC coordinates

For the AC coordinates, the Jacobian needed to make the coordinate transformation in equation 4.11 is represented by

$$\frac{\partial(x_1, x_2, \ldots, x_N, y_1, y_2, \ldots, y_N, z_1, z_2, \ldots, z_N)}{\partial(X_{ac}, x'_2, \ldots, x'_N, Y_{ac}, y'_2 \ldots, y'_N, Z_{ac}, z'_2, \ldots, z'_N)} = |\mathbf{A}_{ac}| \tag{B.6}$$

where $\mathbf{A}_{ac}$ is the $3N \times 3N$ matrix

$$\mathbf{A}_{ac} = \begin{pmatrix}
\frac{\partial x_1}{\partial X_{ac}} & \cdots & \frac{\partial x_N}{\partial X_{ac}} & \frac{\partial x_N}{\partial X_{ac}} & \frac{\partial y_1}{\partial X_{ac}} & \cdots & \frac{\partial y_N}{\partial X_{ac}} & \frac{\partial y_N}{\partial X_{ac}} & \frac{\partial z_1}{\partial X_{ac}} & \cdots & \frac{\partial z_N}{\partial X_{ac}} & \frac{\partial z_N}{\partial X_{ac}} \\
\frac{\partial x_1}{\partial x'_2} & \cdots & \frac{\partial x_N}{\partial x'_2} & \frac{\partial x_N}{\partial x'_2} & \frac{\partial y_1}{\partial x'_2} & \cdots & \frac{\partial y_N}{\partial x'_2} & \frac{\partial y_N}{\partial x'_2} & \frac{\partial z_1}{\partial x'_2} & \cdots & \frac{\partial z_N}{\partial x'_2} & \frac{\partial z_N}{\partial x'_2} \\
\vdots & & \vdots & \vdots & \vdots & & \vdots & \vdots & \vdots & & \vdots & \vdots \\
\frac{\partial x_1}{\partial x'_N} & \cdots & \frac{\partial x_N}{\partial x'_N} & \frac{\partial x_N}{\partial x'_N} & \frac{\partial y_1}{\partial x'_N} & \cdots & \frac{\partial y_N}{\partial x'_N} & \frac{\partial y_N}{\partial x'_N} & \frac{\partial z_1}{\partial x'_N} & \cdots & \frac{\partial z_N}{\partial x'_N} & \frac{\partial z_N}{\partial x'_N} \\
\frac{\partial x_1}{\partial Y_{ac}} & \cdots & \frac{\partial x_N}{\partial Y_{ac}} & \frac{\partial x_N}{\partial Y_{ac}} & \frac{\partial y_1}{\partial Y_{ac}} & \cdots & \frac{\partial y_N}{\partial Y_{ac}} & \frac{\partial y_N}{\partial Y_{ac}} & \frac{\partial z_1}{\partial Y_{ac}} & \cdots & \frac{\partial z_N}{\partial Y_{ac}} & \frac{\partial z_N}{\partial Y_{ac}} \\
\frac{\partial x_1}{\partial y'_2} & \cdots & \frac{\partial x_N}{\partial y'_2} & \frac{\partial x_N}{\partial y'_2} & \frac{\partial y_1}{\partial y'_2} & \cdots & \frac{\partial y_N}{\partial y'_2} & \frac{\partial y_N}{\partial y'_2} & \frac{\partial z_1}{\partial y'_2} & \cdots & \frac{\partial z_N}{\partial y'_2} & \frac{\partial z_N}{\partial y'_2} \\
\vdots & & \vdots & \vdots & \vdots & & \vdots & \vdots & \vdots & & \vdots & \vdots \\
\frac{\partial x_1}{\partial y'_N} & \cdots & \frac{\partial x_N}{\partial y'_N} & \frac{\partial x_N}{\partial y'_N} & \frac{\partial y_1}{\partial y'_N} & \cdots & \frac{\partial y_N}{\partial y'_N} & \frac{\partial y_N}{\partial y'_N} & \frac{\partial z_1}{\partial y'_N} & \cdots & \frac{\partial z_N}{\partial y'_N} & \frac{\partial z_N}{\partial y'_N} \\
\frac{\partial x_1}{\partial Z_{ac}} & \cdots & \frac{\partial x_N}{\partial Z_{ac}} & \frac{\partial x_N}{\partial Z_{ac}} & \frac{\partial y_1}{\partial Z_{ac}} & \cdots & \frac{\partial y_N}{\partial Z_{ac}} & \frac{\partial y_N}{\partial Z_{ac}} & \frac{\partial z_1}{\partial Z_{ac}} & \cdots & \frac{\partial z_N}{\partial Z_{ac}} & \frac{\partial z_N}{\partial Z_{ac}} \\
\frac{\partial x_1}{\partial z'_2} & \cdots & \frac{\partial x_N}{\partial z'_2} & \frac{\partial x_N}{\partial z'_2} & \frac{\partial y_1}{\partial z'_2} & \cdots & \frac{\partial y_N}{\partial z'_2} & \frac{\partial y_N}{\partial z'_2} & \frac{\partial z_1}{\partial z'_2} & \cdots & \frac{\partial z_N}{\partial z'_2} & \frac{\partial z_N}{\partial z'_2} \\
\vdots & & \vdots & \vdots & \vdots & & \vdots & \vdots & \vdots & & \vdots & \vdots \\
\frac{\partial x_1}{\partial z'_N} & \cdots & \frac{\partial x_N}{\partial z'_N} & \frac{\partial x_N}{\partial z'_N} & \frac{\partial y_1}{\partial z'_N} & \cdots & \frac{\partial y_N}{\partial z'_N} & \frac{\partial y_N}{\partial z'_N} & \frac{\partial z_1}{\partial z'_N} & \cdots & \frac{\partial z_N}{\partial z'_N} & \frac{\partial z_N}{\partial z'_N}
\end{pmatrix}$$

which also can be broken down into nine $N \times N$ matrices

$$= \begin{vmatrix}
\mathbf{B}_{ac} & \mathbf{0} & \mathbf{0} \\
\mathbf{0} & \mathbf{B}_{ac} & \mathbf{0} \\
\mathbf{0} & \mathbf{0} & \mathbf{B}_{ac}
\end{vmatrix}$$

where

$$\mathbf{B}_{ac} = \begin{pmatrix}
1 & 1 & 1 & \ldots 1 \\
0 & 1 & 0 & \ldots 0 \\
\vdots & & & \\
0 & 0 & 1 & \ldots 0 \\
0 & 0 & 0 & \ldots 1
\end{pmatrix}$$

In this case, $\mathbf{B}_{ac}$ does not need any rearranging because it is already upper block triangular and $|\mathbf{B}_{ac}| = 1$. Thus, $|\mathbf{A}_{ac}| = |\mathbf{B}_{ac}|^3 = 1$.

Appendix C

JACOBIAN USED FOR TRANSFORMATION OF VARIABLES TO CMNR AND ACNR COORDINATES

C.1 ACNR coordinates

Because the transformation to ACNR coordinates in equation 4.11 is more straightforward we consider it first. Its Jacobian is

$$\frac{\partial(x_1, y_1, z_1, x_2, y_2, z_2, x_3, y_3, z_3, \ldots, x_N, y_N, z_N)}{\partial(X_{ac}, Y_{ac}, Z_{ac}, \theta, \phi, \psi, z'_2, y'_3, z'_3, \ldots, x'_N, y'_N, z'_N)} = |\mathbf{A}_{acnr}|$$

where $\mathbf{A}_{acnr}$ is the following $3N \times 3N$ matrix:

$$\mathbf{A}_{acnr} =$$

$$\begin{pmatrix}
\frac{\partial x_1}{\partial X_{ac}} & \frac{\partial y_1}{\partial X_{ac}} & \frac{\partial z_1}{\partial X_{ac}} & \frac{\partial x_2}{\partial X_{ac}} & \frac{\partial y_2}{\partial X_{ac}} & \frac{\partial z_2}{\partial X_{ac}} & \frac{\partial x_3}{\partial X_{ac}} & \frac{\partial y_3}{\partial X_{ac}} & \frac{\partial z_3}{\partial X_{ac}} & \cdots & \frac{\partial x_N}{\partial X_{ac}} & \frac{\partial y_N}{\partial X_{ac}} & \frac{\partial z_N}{\partial X_{ac}} \\
\frac{\partial x_1}{\partial Y_{ac}} & \frac{\partial y_1}{\partial Y_{ac}} & \frac{\partial z_1}{\partial Y_{ac}} & \frac{\partial x_2}{\partial Y_{ac}} & \frac{\partial y_2}{\partial Y_{ac}} & \frac{\partial z_2}{\partial Y_{ac}} & \frac{\partial x_3}{\partial Y_{ac}} & \frac{\partial y_3}{\partial Y_{ac}} & \frac{\partial z_3}{\partial Y_{ac}} & \cdots & \frac{\partial x_N}{\partial Y_{ac}} & \frac{\partial y_N}{\partial Y_{ac}} & \frac{\partial z_N}{\partial Y_{ac}} \\
\frac{\partial x_1}{\partial Z_{ac}} & \frac{\partial y_1}{\partial Z_{ac}} & \frac{\partial z_1}{\partial Z_{ac}} & \frac{\partial x_2}{\partial Z_{ac}} & \frac{\partial y_2}{\partial Z_{ac}} & \frac{\partial z_2}{\partial Z_{ac}} & \frac{\partial x_3}{\partial Z_{ac}} & \frac{\partial y_3}{\partial Z_{ac}} & \frac{\partial z_3}{\partial Z_{ac}} & \cdots & \frac{\partial x_N}{\partial Z_{ac}} & \frac{\partial y_N}{\partial Z_{ac}} & \frac{\partial z_N}{\partial Z_{ac}} \\
\frac{\partial x_1}{\partial \theta} & \frac{\partial y_1}{\partial \theta} & \frac{\partial z_1}{\partial \theta} & \frac{\partial x_2}{\partial \theta} & \frac{\partial y_2}{\partial \theta} & \frac{\partial z_2}{\partial \theta} & \frac{\partial x_3}{\partial \theta} & \frac{\partial y_3}{\partial \theta} & \frac{\partial z_3}{\partial \theta} & \cdots & \frac{\partial x_N}{\partial \theta} & \frac{\partial y_N}{\partial \theta} & \frac{\partial z_N}{\partial \theta} \\
\frac{\partial x_1}{\partial \phi} & \frac{\partial y_1}{\partial \phi} & \frac{\partial z_1}{\partial \phi} & \frac{\partial x_2}{\partial \phi} & \frac{\partial y_2}{\partial \phi} & \frac{\partial z_2}{\partial \phi} & \frac{\partial x_3}{\partial \phi} & \frac{\partial y_3}{\partial \phi} & \frac{\partial z_3}{\partial \phi} & \cdots & \frac{\partial x_N}{\partial \phi} & \frac{\partial y_N}{\partial \phi} & \frac{\partial z_N}{\partial \phi} \\
\frac{\partial x_1}{\partial \psi} & \frac{\partial y_1}{\partial \psi} & \frac{\partial z_1}{\partial \psi} & \frac{\partial x_2}{\partial \psi} & \frac{\partial y_2}{\partial \psi} & \frac{\partial z_2}{\partial \psi} & \frac{\partial x_3}{\partial \psi} & \frac{\partial y_3}{\partial \psi} & \frac{\partial z_3}{\partial \psi} & \cdots & \frac{\partial x_N}{\partial \psi} & \frac{\partial y_N}{\partial \psi} & \frac{\partial z_N}{\partial \psi} \\
\frac{\partial x_1}{\partial z'_2} & \frac{\partial y_1}{\partial z'_2} & \frac{\partial z_1}{\partial z'_2} & \frac{\partial x_2}{\partial z'_2} & \frac{\partial y_2}{\partial z'_2} & \frac{\partial z_2}{\partial z'_2} & \frac{\partial x_3}{\partial z'_2} & \frac{\partial y_3}{\partial z'_2} & \frac{\partial z_3}{\partial z'_2} & \cdots & \frac{\partial x_N}{\partial z'_2} & \frac{\partial y_N}{\partial z'_2} & \frac{\partial z_N}{\partial z'_2} \\
\frac{\partial x_1}{\partial y'_3} & \frac{\partial y_1}{\partial y'_3} & \frac{\partial z_1}{\partial y'_3} & \frac{\partial x_2}{\partial y'_3} & \frac{\partial y_2}{\partial y'_3} & \frac{\partial z_2}{\partial y'_3} & \frac{\partial x_3}{\partial y'_3} & \frac{\partial y_3}{\partial y'_3} & \frac{\partial z_3}{\partial y'_3} & \cdots & \frac{\partial x_N}{\partial y'_3} & \frac{\partial y_N}{\partial y'_3} & \frac{\partial z_N}{\partial y'_3} \\
\frac{\partial x_1}{\partial z'_3} & \frac{\partial y_1}{\partial z'_3} & \frac{\partial z_1}{\partial z'_3} & \frac{\partial x_2}{\partial z'_3} & \frac{\partial y_2}{\partial z'_3} & \frac{\partial z_2}{\partial z'_3} & \frac{\partial x_3}{\partial z'_3} & \frac{\partial y_3}{\partial z'_3} & \frac{\partial z_3}{\partial z'_3} & \cdots & \frac{\partial x_N}{\partial z'_3} & \frac{\partial y_N}{\partial z'_3} & \frac{\partial z_N}{\partial z'_3} \\
\vdots & & & & & & & & & & & & \\
\frac{\partial x_1}{\partial x'_N} & \frac{\partial y_1}{\partial x'_N} & \frac{\partial z_1}{\partial x'_N} & \frac{\partial x_2}{\partial x'_N} & \frac{\partial y_2}{\partial x'_N} & \frac{\partial z_2}{\partial x'_N} & \frac{\partial x_3}{\partial x'_N} & \frac{\partial y_3}{\partial x'_N} & \frac{\partial z_3}{\partial x'_N} & \cdots & \frac{\partial x_N}{\partial x'_N} & \frac{\partial y_N}{\partial x'_N} & \frac{\partial z_N}{\partial x'_N} \\
\frac{\partial x_1}{\partial y'_N} & \frac{\partial y_1}{\partial y'_N} & \frac{\partial z_1}{\partial y'_N} & \frac{\partial x_2}{\partial y'_N} & \frac{\partial y_2}{\partial y'_N} & \frac{\partial z_2}{\partial y'_N} & \frac{\partial x_3}{\partial y'_N} & \frac{\partial y_3}{\partial y'_N} & \frac{\partial z_3}{\partial y'_N} & \cdots & \frac{\partial x_N}{\partial y'_N} & \frac{\partial y_N}{\partial y'_N} & \frac{\partial z_N}{\partial y'_N} \\
\frac{\partial x_1}{\partial z'_N} & \frac{\partial y_1}{\partial z'_N} & \frac{\partial z_1}{\partial z'_N} & \frac{\partial x_2}{\partial z'_N} & \frac{\partial y_2}{\partial z'_N} & \frac{\partial z_2}{\partial z'_N} & \frac{\partial x_3}{\partial z'_N} & \frac{\partial y_3}{\partial z'_N} & \frac{\partial z_3}{\partial z'_N} & \cdots & \frac{\partial x_N}{\partial z'_N} & \frac{\partial y_N}{\partial z'_N} & \frac{\partial z_N}{\partial z'_N}
\end{pmatrix}$$

$\mathbf{A}_{acnr}$ can be broken down into N (3×3) matrices.

$$\mathbf{A}_{acnr} = \begin{pmatrix} \mathbf{1} & \mathbf{1} & \mathbf{1} & \mathbf{1} & \dots & \mathbf{1} \\ \mathbf{0} & \mathbf{B}^2_{acnr} & \mathbf{B}^3_{acnr} & \mathbf{B}^4_{acnr} & \dots & \mathbf{B}^N_{acnr} \\ \mathbf{0} & \mathbf{C}^2_{acnr} & \mathbf{C}^3_{acnr} & \mathbf{0} & \dots & \mathbf{0} \\ \mathbf{0} & \mathbf{0} & \mathbf{0} & \mathbf{D}^T & \dots & \mathbf{0} \\ \vdots & & & & & \\ \mathbf{0} & \mathbf{0} & \mathbf{0} & \mathbf{0} & \dots & \mathbf{D}^T \end{pmatrix}$$

where **1** is the identity matrix and **0** is a matrix of all zero elements. **D** is the rotation matrix in equation 4.21 while

$$\mathbf{B}^2_{acnr} = \begin{pmatrix} z'_2 \frac{\partial D_{13}}{\partial \theta} & z'_2 \frac{\partial D_{23}}{\partial \theta} & z'_2 \frac{\partial D_{33}}{\partial \theta} \\ z'_2 \frac{\partial D_{13}}{\partial \phi} & z'_2 \frac{\partial D_{23}}{\partial \phi} & z'_2 \frac{\partial D_{33}}{\partial \phi} \\ 0 & 0 & 0 \end{pmatrix}$$

$$\mathbf{B}^3_{acnr} = \begin{pmatrix} y'_3 \frac{\partial D_{12}}{\partial \theta} + z'_3 \frac{\partial D_{13}}{\partial \theta} & y'_3 \frac{\partial D_{22}}{\partial \theta} + z'_3 \frac{\partial D_{23}}{\partial \theta} & y'_3 \frac{\partial D_{32}}{\partial \theta} + z'_3 \frac{\partial D_{33}}{\partial \theta} \\ y'_3 \frac{\partial D_{12}}{\partial \phi} + z'_3 \frac{\partial D_{13}}{\partial \phi} & y'_3 \frac{\partial D_{22}}{\partial \phi} + z'_3 \frac{\partial D_{23}}{\partial \phi} & y'_3 \frac{\partial D_{32}}{\partial \phi} + z'_3 \frac{\partial D_{33}}{\partial \phi} \\ y'_3 \frac{\partial D_{12}}{\partial \psi} + z'_3 \frac{\partial D_{13}}{\partial \psi} & y'_3 \frac{\partial D_{22}}{\partial \psi} + z'_3 \frac{\partial D_{23}}{\partial \psi} & y'_3 \frac{\partial D_{32}}{\partial \psi} + z'_3 \frac{\partial D_{33}}{\partial \psi} \end{pmatrix}$$

$$\mathbf{C}^2_{acnr} = \begin{pmatrix} D_{13} & D_{23} & D_{33} \\ 0 & 0 & 0 \\ 0 & 0 & 0 \end{pmatrix} \qquad \mathbf{C}^3_{acnr} = \begin{pmatrix} 0 & 0 & 0 \\ D_{12} & D_{22} & D_{32} \\ D_{13} & D_{23} & D_{33} \end{pmatrix}$$

If the sixth and seventh rows of $\mathbf{A}_{acnr}$ are exchanged then the new matrix is

$$\mathbf{A}'_{acnr} = \begin{pmatrix} \mathbf{1} & \mathbf{1} & \mathbf{1} & \mathbf{1} & \dots & \mathbf{1} \\ \mathbf{0} & \mathbf{B}^{2'}_{acnr} & \mathbf{B}^{3'}_{acnr} & \mathbf{B}^{4'}_{acnr} & \dots & \mathbf{B}^{N'}_{acnr} \\ \mathbf{0} & \mathbf{0} & \mathbf{C}^{3'}_{acnr} & \mathbf{0} & \dots & \mathbf{0} \\ \mathbf{0} & \mathbf{0} & \mathbf{0} & \mathbf{D}^T & \dots & \mathbf{0} \\ \vdots & & & & & \\ \mathbf{0} & \mathbf{0} & \mathbf{0} & \mathbf{0} & \dots & \mathbf{D}^T \end{pmatrix}$$

and by the rules of determinants

$$|\mathbf{A}_{acnr}| = -|\mathbf{A}'_{acnr}| = -|\mathbf{B}^{2'}_{acnr}||\mathbf{C}^{3'}_{acnr}||\mathbf{D}|^{N-3}.$$

Because the block matrices are only 3×3, their determinants are easily determined.

$$|\mathbf{B}^{2'}_{acnr}| = \begin{vmatrix} z'_2 \cos\theta \sin\phi & -z'_2 \cos\theta \cos\phi & -z'_2 \sin\theta \\ z'_2 \sin\theta \cos\phi & z'_2 \sin\theta \sin\phi & 0 \\ \cos\phi\cos\psi - \sin\phi\cos\theta\sin\psi & -\cos\phi\sin\psi - \sin\phi\cos\theta\cos\psi & \sin\theta\sin\phi \end{vmatrix}$$
$$= z'^2_2 \sin\theta$$

$$|\mathbf{C}'_3| = \begin{vmatrix} y'_3(-\cos\phi\cos\upsilon + \cos\theta\sin\phi\sin\upsilon) & y'_3(-\cos\upsilon\sin\phi - \cos\theta\cos\phi\sin\upsilon) & -y'_3\sin\theta\sin\upsilon \\ \sin\phi\cos\upsilon + \cos\phi\cos\theta\sin\upsilon & -\sin\phi\sin\upsilon + \cos\phi\cos\theta\cos\upsilon & -\cos\theta\sin\phi \\ \cos\phi\cos\upsilon - \sin\phi\cos\theta\sin\upsilon & -\cos\phi\sin\upsilon - \sin\phi\cos\theta\cos\upsilon & \sin\theta\sin\phi \end{vmatrix}$$
$$= -y'_3$$

$$|\mathbf{D}| = \begin{vmatrix} \cos\phi\cos\psi - \sin\phi\cos\theta\sin\psi & -\cos\phi\sin\psi - \sin\phi\cos\theta\cos\psi & \sin\theta\sin\phi \\ \sin\phi\cos\psi + \cos\phi\cos\theta\sin\psi & -\sin\phi\sin\psi + \cos\phi\cos\theta\cos\psi & -\cos\theta\sin\phi \\ \sin\theta\sin\psi & \sin\theta\cos\psi & \cos\theta \end{vmatrix}$$
$$= 1$$

and lastly, $|\mathbf{A}_{acnr}| = z'^2_2 y'_3 \sin\theta$.

C.2 CMNR coordinates

The Jacobian needed to make the transformation to CMNR coordinates in equation 4.3 is

$$\frac{\partial(x_1, y_1, z_1, x_2, y_2, z_2, x_3, y_3, z_3, \ldots, x_N, y_N, z_N)}{\partial(X_{cm}, Y_{cm}, Z_{cm}, \theta, \phi, \psi, z'_2, y'_3, z'_3, \ldots, x'_N, y'_N, z'_N)} = |\mathbf{A}_{cmnr}|$$

where $\mathbf{A}_{cmnr}$ is the following $3N \times 3N$ matrix:

$$\mathbf{A}_{cmnr} =$$

$$\begin{pmatrix}
\frac{\partial x_1}{\partial X_{cm}} & \frac{\partial y_1}{\partial X_{cm}} & \frac{\partial z_1}{\partial X_{cm}} & \frac{\partial x_2}{\partial X_{cm}} & \frac{\partial y_2}{\partial X_{cm}} & \frac{\partial z_2}{\partial X_{cm}} & \frac{\partial x_3}{\partial X_{cm}} & \frac{\partial y_3}{\partial X_{cm}} & \frac{\partial z_3}{\partial X_{cm}} & \cdots & \frac{\partial x_N}{\partial X_{cm}} & \frac{\partial y_N}{\partial X_{cm}} & \frac{\partial z_N}{\partial X_{cm}} \\
\frac{\partial x_1}{\partial Y_{cm}} & \frac{\partial y_1}{\partial Y_{cm}} & \frac{\partial z_1}{\partial Y_{cm}} & \frac{\partial x_2}{\partial Y_{cm}} & \frac{\partial y_2}{\partial Y_{cm}} & \frac{\partial z_2}{\partial Y_{cm}} & \frac{\partial x_3}{\partial Y_{cm}} & \frac{\partial y_3}{\partial Y_{cm}} & \frac{\partial z_3}{\partial Y_{cm}} & \cdots & \frac{\partial x_N}{\partial Y_{cm}} & \frac{\partial y_N}{\partial Y_{cm}} & \frac{\partial z_N}{\partial Y_{cm}} \\
\frac{\partial x_1}{\partial Z_{cm}} & \frac{\partial y_1}{\partial Z_{cm}} & \frac{\partial z_1}{\partial Z_{cm}} & \frac{\partial x_2}{\partial Z_{cm}} & \frac{\partial y_2}{\partial Z_{cm}} & \frac{\partial z_2}{\partial Z_{cm}} & \frac{\partial x_3}{\partial Z_{cm}} & \frac{\partial y_3}{\partial Z_{cm}} & \frac{\partial z_3}{\partial Z_{cm}} & \cdots & \frac{\partial x_N}{\partial Z_{cm}} & \frac{\partial y_N}{\partial Z_{cm}} & \frac{\partial z_N}{\partial Z_{cm}} \\
\frac{\partial x_1}{\partial \theta} & \frac{\partial y_1}{\partial \theta} & \frac{\partial z_1}{\partial \theta} & \frac{\partial x_2}{\partial \theta} & \frac{\partial y_2}{\partial \theta} & \frac{\partial z_2}{\partial \theta} & \frac{\partial x_3}{\partial \theta} & \frac{\partial y_3}{\partial \theta} & \frac{\partial z_3}{\partial \theta} & \cdots & \frac{\partial x_N}{\partial \theta} & \frac{\partial y_N}{\partial \theta} & \frac{\partial z_N}{\partial \theta} \\
\frac{\partial x_1}{\partial \phi} & \frac{\partial y_1}{\partial \phi} & \frac{\partial z_1}{\partial \phi} & \frac{\partial x_2}{\partial \phi} & \frac{\partial y_2}{\partial \phi} & \frac{\partial z_2}{\partial \phi} & \frac{\partial x_3}{\partial \phi} & \frac{\partial y_3}{\partial \phi} & \frac{\partial z_3}{\partial \phi} & \cdots & \frac{\partial x_N}{\partial \phi} & \frac{\partial y_N}{\partial \phi} & \frac{\partial z_N}{\partial \phi} \\
\frac{\partial x_1}{\partial \psi} & \frac{\partial y_1}{\partial \psi} & \frac{\partial z_1}{\partial \psi} & \frac{\partial x_2}{\partial \psi} & \frac{\partial y_2}{\partial \psi} & \frac{\partial z_2}{\partial \psi} & \frac{\partial x_3}{\partial \psi} & \frac{\partial y_3}{\partial \psi} & \frac{\partial z_3}{\partial \psi} & \cdots & \frac{\partial x_N}{\partial \psi} & \frac{\partial y_N}{\partial \psi} & \frac{\partial z_N}{\partial \psi} \\
\frac{\partial x_1}{\partial x'_2} & \frac{\partial y_1}{\partial x'_2} & \frac{\partial z_1}{\partial x'_2} & \frac{\partial x_2}{\partial x'_2} & \frac{\partial y_2}{\partial x'_2} & \frac{\partial z_2}{\partial x'_2} & \frac{\partial x_3}{\partial x'_2} & \frac{\partial y_3}{\partial x'_2} & \frac{\partial z_3}{\partial x'_2} & \cdots & \frac{\partial x_N}{\partial x'_2} & \frac{\partial y_N}{\partial x'_2} & \frac{\partial z_N}{\partial x'_2} \\
\frac{\partial x_1}{\partial y'_3} & \frac{\partial y_1}{\partial y'_3} & \frac{\partial z_1}{\partial y'_3} & \frac{\partial x_2}{\partial y'_3} & \frac{\partial y_2}{\partial y'_3} & \frac{\partial z_2}{\partial y'_3} & \frac{\partial x_3}{\partial y'_3} & \frac{\partial y_3}{\partial y'_3} & \frac{\partial z_3}{\partial y'_3} & \cdots & \frac{\partial x_N}{\partial y'_3} & \frac{\partial y_N}{\partial y'_3} & \frac{\partial z_N}{\partial y'_3} \\
\frac{\partial x_1}{\partial z'_3} & \frac{\partial y_1}{\partial z'_3} & \frac{\partial z_1}{\partial z'_3} & \frac{\partial x_2}{\partial z'_3} & \frac{\partial y_2}{\partial z'_3} & \frac{\partial z_2}{\partial z'_3} & \frac{\partial x_3}{\partial z'_3} & \frac{\partial y_3}{\partial z'_3} & \frac{\partial z_3}{\partial z'_3} & \cdots & \frac{\partial x_N}{\partial z'_3} & \frac{\partial y_N}{\partial z'_3} & \frac{\partial z_N}{\partial z'_3} \\
\vdots & & & & & & & & & & & & \\
\frac{\partial x_1}{\partial x'_N} & \frac{\partial y_1}{\partial x'_N} & \frac{\partial z_1}{\partial x'_N} & \frac{\partial x_2}{\partial x'_N} & \frac{\partial y_2}{\partial x'_N} & \frac{\partial z_2}{\partial x'_N} & \frac{\partial x_3}{\partial x'_N} & \frac{\partial y_3}{\partial x'_N} & \frac{\partial z_3}{\partial x'_N} & \cdots & \frac{\partial x_N}{\partial x'_N} & \frac{\partial y_N}{\partial x'_N} & \frac{\partial z_N}{\partial x'_N} \\
\frac{\partial x_1}{\partial y'_N} & \frac{\partial y_1}{\partial y'_N} & \frac{\partial z_1}{\partial y'_N} & \frac{\partial x_2}{\partial y'_N} & \frac{\partial y_2}{\partial y'_N} & \frac{\partial z_2}{\partial y'_N} & \frac{\partial x_3}{\partial y'_N} & \frac{\partial y_3}{\partial y'_N} & \frac{\partial z_3}{\partial y'_N} & \cdots & \frac{\partial x_N}{\partial y'_N} & \frac{\partial y_N}{\partial y'_N} & \frac{\partial z_N}{\partial y'_N} \\
\frac{\partial x_1}{\partial z'_N} & \frac{\partial y_1}{\partial z'_N} & \frac{\partial z_1}{\partial z'_N} & \frac{\partial x_2}{\partial z'_N} & \frac{\partial y_2}{\partial z'_N} & \frac{\partial z_2}{\partial z'_N} & \frac{\partial x_3}{\partial z'_N} & \frac{\partial y_3}{\partial z'_N} & \frac{\partial z_3}{\partial z'_N} & \cdots & \frac{\partial x_N}{\partial z'_N} & \frac{\partial y_N}{\partial z'_N} & \frac{\partial z_N}{\partial z'_N}
\end{pmatrix}$$

$\mathbf{A}_{acnr}$ can be broken down into N (3×3) matrices.

$$\mathbf{A}_{acnr} = \begin{pmatrix}
\mathbf{1} & \mathbf{1} & \mathbf{1} & \mathbf{1} & \cdots & \mathbf{1} \\
\mathbf{B}^1_{cmnr} & \mathbf{B}^2_{cmnr} & \mathbf{B}^3_{cmnr} & \mathbf{B}^4_{cmnr} & \cdots & \mathbf{B}^N_{cmnr} \\
\mathbf{C}^1_{cmnr} & \mathbf{C}^2_{cmnr} & \mathbf{C}^3_{cmnr} & \mathbf{0} & \cdots & \mathbf{0} \\
(-1)\mathbf{D}^T & \mathbf{0} & \mathbf{0} & \mathbf{D}^T & \cdots & \mathbf{0} \\
\vdots & & & & & \\
(-1)\mathbf{D}^T & \mathbf{0} & \mathbf{0} & \mathbf{0} & \cdots & \mathbf{D}^T
\end{pmatrix}$$

A matrix, $\mathbf{A}'_{cmnr}$ is formed by consecutively adding the $i+3, i+4$ and $i+5$ columns of $\mathbf{A}_{cmnr}$ to columns 1, 2 and 3 respectively starting with $i = 1$ and incrementing i by three until $i = 3N - 5$. One can easily see that after the third block row, the matrices in the first block column of $\mathbf{A}_{cmnr}$ become $\mathbf{0}$ matrices

resulting in

$$\mathbf{A}'_{cmnr} = \begin{pmatrix} N\mathbf{1} & \mathbf{1} & \mathbf{1} & \mathbf{1} & \dots & \mathbf{1} \\ \mathbf{B}^{1'}_{cmnr} & \mathbf{B}^{2}_{cmnr} & \mathbf{B}^{3}_{cmnr} & \mathbf{B}^{4}_{cmnr} & \dots & \mathbf{B}^{N}_{cmnr} \\ \mathbf{C}^{1'}_{cmnr} & \mathbf{C}^{2}_{cmnr} & \mathbf{C}^{3}_{cmnr} & \mathbf{0} & \dots & \mathbf{0} \\ \mathbf{0} & \mathbf{0} & \mathbf{0} & \mathbf{D}^{T} & \dots & \mathbf{0} \\ \vdots & & & & & \\ \mathbf{0} & \mathbf{0} & \mathbf{0} & \mathbf{0} & \dots & \mathbf{D}^{T} \end{pmatrix}$$

Inspection of equation 4.3, shows that

$$B^{1}_{cmnr_{uv}} = -z'_2\frac{\partial D_{v3}}{\partial \alpha} - y'_3\frac{\partial D_{v2}}{\partial \alpha} - z'_3\frac{\partial D_{v3}}{\partial \alpha} - x'_4\frac{\partial D_{v1}}{\partial \alpha} - y'_4\frac{\partial D_{v2}}{\partial \alpha} - z'_4\frac{\partial D_{v3}}{\partial \alpha} \\ \dots - x'_N\frac{\partial D_{v1}}{\partial \alpha} - y'_N\frac{\partial D_{v2}}{\partial \alpha} - z'_N\frac{\partial D_{v3}}{\partial \alpha}$$

while

$$\begin{aligned} B^{2}_{cmnr_{uv}} &= z'_2\frac{\partial D_{v3}}{\partial \alpha} \\ B^{3}_{cmnr_{uv}} &= y'_3\frac{\partial D_{v2}}{\partial \alpha} + z'_3\frac{\partial D_{v3}}{\partial \alpha} \\ B^{4}_{cmnr_{uv}} &= x'_4\frac{\partial D_{v1}}{\partial \alpha} + y'_4\frac{\partial D_{v2}}{\partial \alpha} + z'_4\frac{\partial D_{v3}}{\partial \alpha} \\ &\vdots \\ B^{N}_{cmnr_{uv}} &= x'_N\frac{\partial D_{v1}}{\partial \alpha} + y'_N\frac{\partial D_{v2}}{\partial \alpha} + z'_N\frac{\partial D_{v3}}{\partial \alpha} \end{aligned}$$

where for $u = 1, 2, 3$ and $v = 1, 2, 3$ and

$$\begin{aligned} u &= 1; \qquad \alpha = \theta \\ u &= 2; \qquad \alpha = \phi \\ u &= 3; \qquad \alpha = \psi \end{aligned}$$

such that the column adding operation yields $\mathbf{B}'_1 = \mathbf{0}$. Additionally,

$$\mathbf{C}^{1}_{cmnr} = \begin{pmatrix} -D_{13} & -D_{23} & -D_{33} \\ -D_{12} & -D_{22} & -D_{32} \\ -D_{13} & -D_{23} & -D_{33} \end{pmatrix}$$

$$\mathbf{C}^2_{cmnr} = \begin{pmatrix} D_{13} & D_{23} & D_{33} \\ 0 & 0 & 0 \\ 0 & 0 & 0 \end{pmatrix} \qquad \mathbf{C}^3_{cmnr} = \begin{pmatrix} 0 & 0 & 0 \\ D_{12} & D_{22} & D_{32} \\ D_{13} & D_{23} & D_{33} \end{pmatrix}$$

thus, the column adding operation results in $\mathbf{C}^{1'}_{cmnr} = \mathbf{0}$ and

$$\mathbf{A}'_{cmnr} = \begin{pmatrix} N\mathbf{1} & \mathbf{1} & \mathbf{1} & \mathbf{1} & \dots & \mathbf{1} \\ \mathbf{0} & \mathbf{B}^2_{cmnr} & \mathbf{B}^3_{cmnr} & \mathbf{B}^4_{cmnr} & \dots & \mathbf{B}^N_{cmnr} \\ \mathbf{0} & \mathbf{C}^2_{cmnr} & \mathbf{C}^3_{cmnr} & \mathbf{0} & \dots & \mathbf{0} \\ \mathbf{0} & \mathbf{0} & \mathbf{0} & \mathbf{D}^T & \dots & \mathbf{0} \\ \vdots & & & & & \\ \mathbf{0} & \mathbf{0} & \mathbf{0} & \mathbf{0} & \dots & \mathbf{D}^T \end{pmatrix}$$

The 6th and 7th rows of $\mathbf{A}'_{cmnr}$ are then exchanged as was done for the ACNR coordinates to form $\mathbf{A}''_{cmnr}$. For $i > 1$,

$$\mathbf{B}^i_{cmnr} = \mathbf{B}^i_{acnr}; \qquad \mathbf{C}^i_{cmnr} = \mathbf{C}^i_{acnr}$$

so the row exchange leads to

$$\mathbf{B}^{i'}_{cmnr} = \mathbf{B}^{i'}_{acnr}; \qquad \mathbf{C}^{i'}_{cmnr} = \mathbf{C}^{i'}_{acnr}$$

and nearly the same form for $\mathbf{A}''_{cmnr}$ as $\mathbf{A}'_{acnr}$.

$$\mathbf{A}''_{cmnr} = \begin{pmatrix} N\mathbf{1} & \mathbf{1} & \mathbf{1} & \mathbf{1} & \dots & \mathbf{1} \\ \mathbf{0} & \mathbf{B}^{2'}_{acnr} & \mathbf{B}^{3'}_{acnr} & \mathbf{B}^{4'}_{acnr} & \dots & \mathbf{B}^{N'}_{acnr} \\ \mathbf{0} & \mathbf{0} & \mathbf{C}^{3'}_{acnr} & \mathbf{0} & \dots & \mathbf{0} \\ \mathbf{0} & \mathbf{0} & \mathbf{0} & \mathbf{D}^T & \dots & \mathbf{0} \\ \vdots & & & & & \\ \mathbf{0} & \mathbf{0} & \mathbf{0} & \mathbf{0} & \dots & \mathbf{D}^T \end{pmatrix}$$

and $|\mathbf{A}_{cmnr}| = |\mathbf{A}'_{cmnr}| = -|\mathbf{A}''_{cmnr}| = -N^3|\mathbf{B}^{2'}_{acnr}||\mathbf{C}^{3'}_{acnr}||\mathbf{D}|^{N-3} = N^3 z'^2_2 y'_3 \sin\theta$.

Appendix D

CODE USED FOR MONTE CARLO INTEGRATION OF CMNR REFERENCE STATE PARTITION FUNCTION

total number of MC steps = $MaxSteps$

radius of spheres = R_c

positions of lattice = site_i

maximum value of the partition function, $maxQ = (site.y_3 + R_c)(site.z_2 + R_c)^2$

volume of coordinate space, $volume = \left(\frac{4\pi}{3} R_c^{N-3}\right)(2\pi R_c)(\pi R_c^2)$

$integral = 0.0$

for $iter = 1$ to $MaxSteps$ **do**

$sum.x = 0.0$; $sum.y = 0.0$; $sum.z = 0.0$

choose z-coordinate for atom 1, $z_1 = (2.0 * ran - 1.0)R_c$

choose y and z-coordinates for atom 2

$done = 0$

while $done = 0$ **do**

$y_2 = (2.0 * ran - 1.0)R_c$

$z_2 = (2.0 * ran - 1.0)R_c$

if $y_2^2 + z_2^2 \leq R_c^2$ **then**

done = 1

end if

end while

positions are to relative to the lattice sites

$z_1 = z_1 + site.z_1$

$y_2 = y_2 + site.y_2$; $z_2 = z_2 + site.2_2$

need term for Jacobian (see eq. 4.22); $term = z_1^2 y_2$

update sum; $sum.y = sum.y + y_1$; $sum.z = sum.z + z_1 + z_2$;

for $i = 4$ to $i \leq N$ **do**

choose x, y and z-coordinates for atom i

$done = 0$

while $done = 0$ **do**

$r.x = (2.0 * ran - 1.0)R_c$

$r.y = (2.0 * ran - 1.0)R_c$

$r.z = (2.0 * ran - 1.0)R_c$

if $r.x^2 + r.y^2 + r.z^2 \leq R_c^2$ **then**

$done = 1$

end if

end while

update sum; $\mathbf{sum} = \mathbf{sum} + \mathbf{r} + \mathbf{site}_i$

end for

coordinates for atom 1; $\mathbf{r}_1 = -\mathbf{sum} - \mathbf{site}_1$

if $\mathbf{r}_1^2 \leq R_c^2$ **then**

$trial = term$

else

$trial = 0.0$

end if

if $ran * MaxQ \leq trial$ **then**

$integral = integral + 1.0$

end if

end for

print $Q_{cmnr} = (integral/MaxSteps) * volume * MaxQ$

Vita

Lynn Marie Amon was born in Mt. Clemens, Michigan in 1970. She attended Romeo High School in Romeo, Michigan and graduated in 1988. She earned her Bachelors of Science in Chemistry from Saint Mary's College in 1992. In March, 2000, she earned her doctorate of philosophy in chemistry from the University of Washington under William P. Reinhardt. Much of the work presented here will be published in the Journal of Chemical Physics with W. P. Reinhardt. The portion of the work concerning step size adjustment in Monte Carlo simulations will be published in Chemical Physics Letters with W. P. Reinhardt and Mark Miller.